



THE HONG KONG
POLYTECHNIC UNIVERSITY

香港理工大學

Pao Yue-kong Library

包玉剛圖書館

Copyright Undertaking

This thesis is protected by copyright, with all rights reserved.

By reading and using the thesis, the reader understands and agrees to the following terms:

1. The reader will abide by the rules and legal ordinances governing copyright regarding the use of the thesis.
2. The reader will use the thesis for the purpose of research or private study only and not for distribution or further reproduction or any other purpose.
3. The reader agrees to indemnify and hold the University harmless from and against any loss, damage, cost, liability or expenses arising from copyright infringement or unauthorized usage.

IMPORTANT

If you have reasons to believe that any materials in this thesis are deemed not suitable to be distributed in this form, or a copyright owner having difficulty with the material being included in our database, please contact lbsys@polyu.edu.hk providing details. The Library will look into your claim and consider taking remedial action upon receipt of the written requests.

**DESIGN AND FABRICATION OF
LANTHANIDE-DOPED UPCONVERSION
PARTICLES FOR OPTICAL APPLICATIONS**

WANG TING

PhD

The Hong Kong Polytechnic University

2020

The Hong Kong Polytechnic University

Department of Applied Physics

**DESIGN AND FABRICATION OF LANTHANIDE-
DOPED UPCONVERSION PARTICLES FOR OPTICAL
APPLICATIONS**

WANG TING

A thesis submitted in partial fulfillment of the requirements

for the degree of Doctor of Philosophy

June 2019



Certificate of Originality

I hereby declare that this thesis is my own work and, to the best of my knowledge and belief, it reproduces no material previously published or written, nor material that has been accepted for the award of any other degree or diploma, except where due acknowledgment has been made in the text.

(Signature)

WANG Ting

(Name of candidate)



Abstract

Upconversion (UC) emission via lanthanide (Ln^{3+}) ions is a nonlinear optical process that can convert near-infrared (NIR) pump light to visible output. A wide emission wavelength from ultraviolet (UV) to infrared regime, which can be obtained from the Ln^{3+} -doped UC materials, is a necessary condition to realize broadband-tunable lasers. However, the relatively low UC emission efficiency leads to the high excitation threshold of Ln^{3+} -doped UC lasers. If the lasing threshold can be further reduced, the wide bandwidth emission characteristics of UC lasers may find enormous applications such as all-optical on-chip information processing, biomedical imaging, and optogenetics. Therefore, in this thesis, we propose using Ln^{3+} -doped UC particles, including the micro- and nano-particles, to obtain multi-wavelength lasing emission based on improving UC emission efficiency.

In chapter 3, Ln^{3+} ions (Yb^{3+} , Er^{3+} , and Tm^{3+}) doped $\beta\text{-NaYF}_4$ hexagonal microrods are proposed to support UC lasing emission under 980 nm ns-pulsed laser excitation. The single $\beta\text{-NaYF}_4$ hexagonal microrod, which hexagonal shape supports whispering gallery modes (WGMs), obtains multi-wavelength lasing emission under 980 nm ns-pulsed laser excitation. Initially, UC lasing emission intensities at red/green/blue (RGB) areas are optimized by modulating the Ln^{3+} concentration and then further controlling the $\beta\text{-NaYF}_4$ hexagonal microrods radius to decrease the lasing threshold. In this chapter, the RGB and white lasing emissions are successfully produced. In chapter 4, we further improve the single $\beta\text{-NaYF}_4$ hexagonal microrods UC lasing intensity by introducing surface plasmonic effect. Here, Ag film is utilized to introduce the plasmonic effect



and the experimental results show that the spontaneous UC emission intensity of the single β -NaYF₄ hexagonal microrods can be increased by more than 10 times and the values of the UC lasing threshold can be decreased by 50%. Besides, we note that the UC improvement is due to the optical coupling between the WGMs and the surface plasmonic resonance modes.

UC characteristics of Ln³⁺-doped nanoparticles on the lasing enhancement are investigated in chapter 5. Firstly, we find visually that the improvement of UC photoluminescence is due to the suppression of surface-related deactivations of the nanoparticles. This can be done by using aberration corrected high angle annular dark field (HAADF) scanning transmission electron microscopy (STEM) to directly observe the surface conditions of KLu₂F₇:Yb³⁺, Er³⁺ bare core UC nanoparticles in atomic scale. Due to the very thin and uniform thickness of the KLu₂F₇ nanoparticles, we observe unambiguously that the removal of surface defects by using the thermal annealing method can enhance UC photoluminescence. The realization of dominant green lasing emission under 980 nm ns-pulsed laser excitation further confirm the high crystallinity of the KLu₂F₇ nanoparticles.

Although the use of thermal annealing can strongly suppress the surface defects of Ln³⁺-doped UC nanoparticles during their growth process, the corresponding mechanism of surface defects restoration process is still unknown. Understanding the detail growth process of the UC nanoparticles can guide us to improve the UC efficiency of Ln³⁺-doped nanoparticles. In chapter 6, we observe the growth process of Yb³⁺, Er³⁺ co-doped LuF₃ nanoparticles by using *in situ* transmission electron microscopy (TEM) imaging technique to deduce the corresponding surface defects restoration mechanism. Here, we verify that the enhancement of LuF₃ nanoparticles UC



efficiency can be realized by crystallization of the surface clusters of the $\text{LuF}_3:\text{Yb}^{3+}$, Er^{3+} nanoparticles. This is because the surface clusters act as defect centers which decrease the UC efficiency of the nanoparticles. Hence, it is shown that the enhancement of UC intensity can be attributed to the removal of surface defects after using the thermal annealing method during the nanoparticles growth process.



List of Publications

1. **Ting Wang**, Huan Yu, Chun Kit Siu, Jianbei Qiu, Xuhui Xu*, and Siu Fung Yu*, "White-Light Whispering-Gallery-Mode Lasing from Lanthanide-Doped Upconversion NaYF₄ Hexagonal Microrods," *ACS Photonics* **4** (6), 1539-1543 (2017);
2. **Ting Wang**, Chun Kit Siu, Huan Yu, Yunfeng Wang, Siqi Li, Wei Lu, Jianhua Hao, Hong Liu, Jing Hua Teng, Dang Yuan Lei, Xuhui Xu, and Siu Fung Yu*, "Influence of Plasmonic Effect on the Upconversion Emission Characteristics of NaYF₄ Hexagonal Microrods," *Inorganic Chemistry* **57** (14), 8200-8204 (2018);
3. Wenjuan Bian, Yue Lin, **Ting Wang**, Xue Yu, Jianbei Qiu, Meng Zhou, Hongmei Luo, Siu Fung Yu*, and Xuhui Xu*, "Direct Identification of Surface Defects and Their Influence on the Optical Characteristics of Upconversion Nanoparticles," *ACS Nano* **12** (4), 3623-3628 (2018);
4. Liuli Yang, **Ting Wang**, Qihong Min, Bitao Liu, Zhichao Liu, Xiaotong Fan, Jianbei Qiu, Xuhui Xu*, Jie Yu, and Xue Yu, "High Water Resistance of Monoclinic CsPbBr₃ Nanocrystals Derived from Zero-Dimensional Cesium Lead Halide Perovskites," *ACS Omega* **4** (3), 6084-6091 (2019).
5. **Ting Wang**, Yue Lin, Wei Lu, Xuyun Guo, Jianbei Qiu, Xue Yu, Qiuqiang Zhan, Siu Fung Yu*, Xuhui Xu, The Growth Processes of Quasi-2D LuF₃ Upconversion Nanoflakes with Assistance of Amorphous Nanoclusters, *ACS Applied Nano Materials*, **2** (8) 5254-5259 (2019)
6. **Ting Wang**, Wei Lu, Xuhui Xu, Jianbei Qiu, Siu Fung Yu*, Study of Crystallization and Coalescence of Nanocrystals in Amorphous Glass at High Temperature, *Inorganic Chemistry*, **58** (14)9500-9504 (2019)
7. **Ting Wang**, Wei Lu, Qihua Yang, Xue Yu, Jianbei Qiu, Xuhui Xu, Siu Fung Yu*, A General Growth Process of Single Nanocrystals in Glass, *The Journal of Physical Chemistry Letters* (Submitted)



Acknowledge

Firstly, I want to express my deepest thanks to my supervisor Prof. Siu Fung Yu, thanks for his scrupulous guidance during my 3-year Ph. D. period. I really appreciate that I can join his group and be guided by him, and appreciate how he has always been so friendly and supportive of all of my efforts. He is also one of the best supervisors I have been seen in my Ph.D. period time.

I would like to use this opportunity to express my appreciation to Prof. Xuhui Xu, from the Kunming University of Science and Technology, for his invaluable guidance and support. His ideas, encouragement, attention to details and critiques have immensely improved my research.

Prof. Xue Yu, and Prof. Jianbei Qiu, from the Kunming University of Science and Technology, play an invaluable role in helping me analysis and guide these experiments whenever I was confused in the optical knowledge. They deserve special thanks and recognition.

My colleagues, Chun Kit Siu, Yunfeng Wang, Decheng Yang, Wenfei Zhang, Limin Jin, are a very important part of our groups and they provide a lot of help including the sharing the experiment experience.

Liuli Yang, Huan Yu, Sai Li, Yushuang Qi, et al., those are the research students from the Kunming University of Science and Technology, they help me to fabricate the experimental samples. Without theirs helps, I cannot complete this work. Thank you for your valuable partnership.



I thank my all of the teaching and non-teaching staff, and the classmates, from the Department of Applied Physics, the Hong Kong Polytechnic University, for offering me much inspiration through stimulating discussions and the technical assistance on my research work. I would also like to thank for the time we have spent together over the last three years. They have given me the strength to overcome the difficulty encountered in my journey towards this degree.

As always, I offer my special thanks to my family, my father Jiliang WANG, my mother, Ping YANG, my twin sister Shu YANG, for their encouragement during my study. This work would not be possible without their precious support and encouragement.



List of Contents

Certificate of Originality	i
Abstract	ii
List of Publications	v
Acknowledge	vi
List of Contents	viii
List of Figures	xiii
List of Tables	xxiv
List of Abbreviations	xxv
1. Introduction	1
1.1 Background	1
1.2 Objectives of research	3
1.3 Outline of the thesis	4
2. Literature review of Ln ³⁺ -doped UC lasers	7
2.1 Introduction	7
2.2 The UC mechanisms	7
2.2.1 ESA mechanism	8
2.2.2 ETU mechanism	9



THE HONG KONG POLYTECHNIC UNIVERSITY

2.2.3 PA mechanism	11
2.2.4 EMU mechanism	13
2.3 The Ln ³⁺ -doped UC lasers	14
2.3.1 The Ln ³⁺ -doped bulk crystal UC lasers	15
2.3.2 The Ln ³⁺ -doped UC fiber lasers	19
2.3.3 The Ln ³⁺ -doped UC microsphere lasers	24
2.3.4 The Ln ³⁺ -doped UC nanoparticles lasers.....	28
2.3.5 Summary.....	30
3. White-light WGMs lasing from Ln ³⁺ -doped UC β-NaYF ₄ hexagonal microrods.....	32
3.1 Introduction.....	32
3.2 Fabrication methods of Ln ³⁺ -doped UC β-NaYF ₄ hexagonal microrods	34
3.3 Physical and optical properties	35
3.3.1 Optical measurement setup.....	35
3.3.2 Physical properties of β-NaYF ₄ hexagonal microrods	37
3.4 Photoluminescence properties of β-NaYF ₄ hexagonal microrods by modulating Ln ³⁺ ions doping	41
3.5 RGB and white-light lasing emissions from the Ln ³⁺ -doped β-NaYF ₄ hexagonal microrods	48
3.6 Summary	54



4.	Influence of plasmonic effect on the UC emission of Ln^{3+} -doped $\beta\text{-NaYF}_4$ hexagonal microrods	56
4.1	Introduction.....	56
4.2	Design and fabrication of hexagonal microrods on Ag thin film	57
4.2.1	Simulation methods and results	57
4.2.2	Optical measurement setup.....	58
4.3	Photoluminescence characteristics of the Ln^{3+} -doped $\beta\text{-NaYF}_4$ hexagonal microrods deposited on Ag substrate	59
4.3.1	Influence of the Ag thin film	59
4.3.2	Polarization characteristics of the excitation and emission lights	64
4.4	The plasmonic effect on UC lasing emission characteristics of $\beta\text{-NaYF}_4$ hexagonal microrods	67
4.5	Summary	70
5.	The effect of surface defects of Ln^{3+} -doped KLu_2F_7 UC nanoparticles on UC characteristics.....	71
5.1	Introduction.....	71
5.2	Fabrication methods of KLu_2F_7 UC nanoparticles and microcavities	72
5.3	Physical and optical properties of KLu_2F_7 UC nanoparticles	74
5.3.1	TEM, HAADF-STEM characteristic measurement of KLu_2F_7 UC nanoparticles	74



5.3.2 Physical properties of KLu_2F_7 UC nanoparticles	76
5.4 The enhancement of UC photoluminescence by suppressing the surface defects of the UC nanoparticles	84
5.5 Design and realization of lasing emission from the recovered KLu_2F_7 UC nanoparticles.....	92
5.6 Summary	94
6. Optical properties of Ln^{3+} -doped LuF_3 UC nanoparticles.....	96
6.1 Introduction.....	96
6.2 Fabrication of LuF_3 nanoparticles.....	97
6.2.1 Fabrication methods	97
6.2.2 The thermal annealing methods.....	98
6.3 Physical and optical properties of Ln^{3+} -doped LuF_3 UC nanoparticles.....	98
6.3.1 XRD, TEM, optical characteristics measurement of LuF_3 UC nanoparticles	98
6.3.2 General properties of LuF_3	100
6.3.3 Photoluminescence properties with the relationship of the morphology of the LuF_3 nanoparticles	101
6.4 Growth mechanism of LuF_3 nanoparticles	102
6.4.1 Growth and coalescence processes of LuF_3 nanoparticles	102
6.4.2 Tunable morphology and growth mechanisms.....	108



6.5	Summary	113
7.	Conclusions and outlook	114
7.1	Conclusions.....	114
7.2	Outlook	116
	References.....	118



List of Figures

Figure 1.1 Energy level diagram of Ln^{3+} ions with dominant visible emission transitions observed designated by arrows representing the approximate color of the fluorescence. 2

Figure 2.1 The ESA mechanism of the UC laser process. “a” and “b” shows the two pump sources..... 8

Figure 2.2 The ETU mechanism for two Ln^{3+} ions doped UC mechanism. “D” and “A” are donor and acceptor ions, respectively..... 10

Figure 2.3 Photon avalanche UC emission in Ln^{3+} -doped materials. “D” and “A” are donor and acceptor ions, respectively. 12

Figure 2.4 EMU mechanism process of the UC process in Ln^{3+} -doped materials. “D”, “L”, “M” and “A” are donor, migrate, migrate and acceptor ions, respectively. 13

Figure 2.5 A sample diagram of Ln^{3+} -doped bulk crystal UC lasers resonator..... 15

Figure 2.6 A sample diagram of Ln^{3+} -doped fiber UC lasers resonator..... 19

Figure 2.7 The Ln^{3+} -doped microsphere UC lasers. (a) Schematic diagram, (b) modal field. 24



- Figure 2.8 Microcavity laser based on Ln^{3+} -doped UC nanoparticles. (a) A bottle-like microcavity which is fabricated by coating a mixture of silica resin and UC nanoparticles onto an optical fiber. (b) The core-shell-shell structure of the UC nanoparticles..... 28
- Figure 3.1 The photoluminescence and lasing characteristic measurement setup..... 35
- Figure 3.2 SEM images of (a) 100% Yb^{3+} -1% Er^{3+} , (b) 20% Yb^{3+} -1% Er^{3+} and (c) 40% Yb^{3+} -2% Tm^{3+} co-doped $\beta\text{-NaYF}_4$ hexagonal microrods. (d) XRD patterns of the corresponding co-doped $\beta\text{-NaYF}_4$ hexagonal microrods..... 38
- Figure 3.3 (a) SEM images of the as-synthesized Yb^{3+} , Er^{3+} , and Tm^{3+} tri-doped $\beta\text{-NaYF}_4$ hexagonal microrods. (b) Elemental mapping of a $\beta\text{-NaYF}_4$, (c) HR-TEM image of a $\beta\text{-NaYF}_4$ hexagonal microrod. (d) Electron diffraction image and (e) XRD pattern of $\beta\text{-NaYF}_4$ hexagonal microrods..... 39
- Figure 3.4 Size distribution of Yb^{3+} , Er^{3+} , and Tm^{3+} tri-doped $\beta\text{-NaYF}_4$ hexagonal microrods corresponding to Figure 3.3 a. 40
- Figure 3.5 Energy level diagram of the Yb^{3+} , Er^{3+} , Tm^{3+} tri-doped $\beta\text{-NaYF}_4$ hexagonal microrod under 980nm NIR excitation. The mechanisms of the UC population, radiative and non-radiative recombination as well as cross-relaxation transitions, are indicated in the diagram..... 41
- Figure 3.6 (a) The photoluminescence spectra and (b) the ratio of emission intensity between green and red emission changes of the Yb^{3+} , Er^{3+} co-doped $\beta\text{-NaYF}_4$ hexagonal



- microrods under CW 980 nm laser excitation when the concentration of Yb^{3+} varies from 15% to 100%. The concentration of Er^{3+} ions is fixed at 1%. 42
- Figure 3.7 Photoluminescence spectra of the Yb^{3+} , Tm^{3+} co-doped $\beta\text{-NaYF}_4$ hexagonal microrods under the CW 980 nm laser excitation by modulating the concentration of Yb^{3+} . The concentration of Yb^{3+} is changed from 50% to 20%, and the concentration of Tm^{3+} is fixed at 2%. 44
- Figure 3.8 (a) Photoluminescence spectra and (b) the ratio of emission intensity between green and blue emission as well as red and blue changes of the Yb^{3+} , Tm^{3+} , Er^{3+} tri-doped $\beta\text{-NaYF}_4$ hexagonal microrods under CW 980 nm excitation by modulating the concentration of Er^{3+} . (c) CIE chromaticity image of the tri-doped $\beta\text{-NaYF}_4$ hexagonal microrods. 45
- Figure 3.9 Photoluminescence spectra of the doped $\beta\text{-NaYF}_4$ hexagonal microrods under CW 980 nm excitation at a pumped power of 1 MW/cm^2 . The inset photos show the corresponding emission profile. 47
- Figure 3.10 Lasing emission spectra of three individual $\beta\text{-NaYF}_4$ hexagonal microrods with different doping concentrations under 980 nm ns-pulsed laser excitation. The insets show the corresponding optical images with emission wavelengths of 654, 540 and 450 nm captured by the optical camera. (d) The corresponding intensity vs pump density curves. Numerical simulation of optical field distribution inside a $100\% \text{Yb}^{3+}$, $1\% \text{Er}^{3+}$ co-doped $\beta\text{-NaYF}_4$ hexagonal microrods emitted at 654 nm is shown in the inset of Figure d. The yellow dashed-line indicates the formation of one round-trip. 48



Figure 3.11 Plots of the threshold, P_{th} , versus radius, R , of the Ln^{3+} doped β -NaYF ₄ hexagonal microrods at the RGB emissions.....	50
Figure 3.12 (a) UC intensity as a function of pump density and (b) lasing line width of the RGB emissions for a 40% Yb ³⁺ , 2% Tm ³⁺ , and 0.5% Er ³⁺ tri-doping hexagonal microrod with radius is 4 μ m.....	51
Figure 3.13 Emission spectra of the a 40% Yb ³⁺ , 2% Tm ³⁺ , and 0.5% Er ³⁺ tri-doped hexagonal microrod under 980 nm ns-pulsed excitation, the pump density is (a) 1 and (b) 21.6 mJ/cm ² . The inset in Figure 3.13(b) shows the corresponding single particles picture capture from the optical microscopy under 980 nm ns-pulsed excitation at room temperature.	53
Figure 3.14 The plot of CIE1931 color coordinates of the doped microrods under lasing emission with different (a) radius R with pumped power kept at 21.5 mJ/cm ² and (b) pumped power with radius R kept at 4 μ m.	53
Figure 4.1 The optical measurement setup	58
Figure 4.2 The schematic diagram of the optical resonator.....	60
Figure 4.3 Plot of calculated Q-factor of a β -NaYF ₄ : Yb ³⁺ , Er ³⁺ , Tm ³⁺ hexagonal microrod deposited on an Ag-coated (50 nm) substrate, which is also protected by MgF ₂ dielectric layer with different thickness h	61



- Figure 4.4 The measured photoluminescence UC spectra from a microrod deposited on an Ag-coated substrate with different thicknesses ($h = 0, 5, 50$ nm) of MgF_2 protection layer and without Ag..... 61
- Figure 4.5 UC spontaneous emission spectra of a $\beta\text{-NaYF}_4: x\% \text{Yb}^{3+}, 1\% \text{Er}^{3+}$ hexagonal microrods (with $r \sim 4 \mu\text{m}$) for x equal to (a) 20%, (b) 40% and (c) 60%..... 63
- Figure 4.6 UC spontaneous emission spectra of a doped $\beta\text{-NaYF}_4: \text{Yb}^{3+}, \text{Tm}^{3+}$ hexagonal microrods with a radius equal to (a) 3 and (b) 2 μm 63
- Figure 4.7 UC spontaneous emission characteristics of (a) $\beta\text{-NaYF}_4: \text{Yb}^{3+}, \text{Er}^{3+}$ hexagonal microrods and (b) $\beta\text{-NaYF}_4: \text{Yb}^{3+}, \text{Tm}^{3+}$ hexagonal microrods (with $r \sim 4 \mu\text{m}$) under the influence of excitation polarizations (i.e. $\Theta_{\text{in}} = 90^\circ$ and 0°)..... 64
- Figure 4.8 Plot of emission spectra of a $\beta\text{-NaYF}_4: \text{Yb}^{3+}, \text{Er}^{3+}, \text{Tm}^{3+}$ hexagonal microrods at different output polarization, Θ_{out} . The microrod is deposited on an Ag-coated substrate and under CW 980 nm laser excitation with two orthogonal orientations ($\Theta_{\text{in}} = 90^\circ$ perpendicular and $\Theta_{\text{in}} = 0^\circ$ is parallel to the length of the microrod)..... 65
- Figure 4.9 (a) Photos of microrod under CW 980 nm laser excitation with two orthogonal orientations. (b) A two-dimensional plot of emission intensity versus Θ_{in} and emission wavelength intensity. 66
- Figure 4.10 Near-field profile of a $\beta\text{-NaYF}_4: \text{Yb}^{3+}, \text{Er}^{3+}, \text{Tm}^{3+}$ hexagonal microrod (with $r \sim 4 \mu\text{m}$) deposited on the substrate with/without Ag coating under (a) edge and (b) center excitation..... 67



- Figure 4.11 The intensity of the UC lasing emission as a function of pump density with and without deposited on the Ag-coated substrate for the three-color emission peaks (i.e. 450 nm, 540 nm and 654 nm). (b) The corresponding emission spectra of the hexagonal microrods with and without deposition on the Ag-coated substrate at the pumped power of 3.5 mJ/cm². 68
- Figure 4.12 (a) Numerical simulation results of resonant modes inside a hexagonal microrod with different wavelengths (450, 540 and 654 nm). (b) Near-field photo of a hexagonal microrod under 980 nm excitation. (c) Numerical simulation results of resonant modes inside a hexagonal microrod deposited on an Ag-coated substrate with different wavelengths (450, 540 and 654nm). (d) Near-field photo of a hexagonal microrod deposited on an Ag-coated substrate under 980 nm excitation..... 69
- Figure 5.1 Schematic diagram of the thermal annealing process of KLu₂F₇:38% Yb³⁺, 2% Er³⁺ UC nanoparticles..... 76
- Figure 5.2 Photoluminescence spectra of the KLu₂F₇:38% Yb³⁺, 2% Er³⁺ UC nanoparticles *versus* different annealing temperature..... 77
- Figure 5.3 XRD patterns of KLu₂F₇:38% Yb³⁺, 2% Er³⁺ UC nanoparticles before and after the thermal annealing and the standard JCPDS card 27-0459..... 77
- Figure 5.4 (a) TEM, (b) HR-TEM image, (c) FFT profile and (d) particle size distribution profile of the KLu₂F₇ nanoparticles before the thermal annealing. (e) TEM, (f) HR-TEM



- image, (g) FFT profile and (h) particle size distribution KLu_2F_7 nanoparticles after the thermal annealing process..... 79
- Figure 5.5(a) Atomic-scale and (b) magnified blue circle area in (a) images of $\text{KLu}_2\text{F}_7:38\% \text{Yb}^{3+}, 2\% \text{Er}^{3+}$ UC nanoparticles before the thermal annealing process. .. 80
- Figure 5.6 (a) Crystal structure mode of KLu_2F_7 . (Distances between two Lu^{3+} in different positions are $d_{(\text{Lu}4-\text{Lu}1)}=3.52\text{\AA}$, $d_{(\text{Lu}4-\text{Lu}2)}=3.48\text{\AA}$, $d_{(\text{Lu}4-\text{Lu}3)}=3.49\text{\AA}$ and $d_{(\text{Lu}2-\text{Lu}3)}=3.50\text{\AA}$ in the cluster.) (b) Atomic resolution crystal experimental and simulated structure images of a $\text{KLu}_2\text{F}_7:38\% \text{Yb}^{3+}, 2\% \text{Er}^{3+}$ UC nanoparticle before the thermal annealing. The averaged distance between the ionic clusters (3.76-3.83 \AA) is substantially larger than the ionic distance within the clusters (3.48-3.52 \AA). The atomic structure of tetrad clusters that in a KLu_2F_7 host matrix Lu^{3+} ions are separated as arrays of discrete clusters at the sub-lattice level can be clearly observed in the (100) projection..... 81
- Figure 5.7 HAADF-STEM images of $\text{KLu}_2\text{F}_7:38\% \text{Yb}^{3+}, 2\% \text{Er}^{3+}$ UC nanoparticles (a) before and (b) after the thermal annealing at 240°C . Intensity profiles recorded by scanning along with the directions (c) orange and (d) green arrows of the UC nanoparticles as shown in Figures (a) and (b) respectively. Enlarged crystal edge structure images (e) before and (f) after the thermal annealing..... 82
- Figure 5.8 (a) Crystal structure mode of KLu_2F_7 in the (010) projection. (b) The HR-TEM image of a $\text{KLu}_2\text{F}_7:38\% \text{Yb}^{3+}, 2\% \text{Er}^{3+}$ UC nanoparticle after the thermal annealing. .. 84



- Figure 5.9 (a) photoluminescence spectra of the $\text{KLu}_2\text{F}_7:38\% \text{Yb}^{3+}, 2\% \text{Er}^{3+}$ UC nanoparticles. Decay curves of (b) $^4\text{S}_{3/2} \rightarrow ^4\text{I}_{15/2}$ transition (@543 nm), (c) $^4\text{F}_{9/2} \rightarrow ^4\text{I}_{15/2}$ transition (@668 nm), and (d) $^2\text{F}_{5/2} \rightarrow ^2\text{F}_{7/2}$ transition (@980 nm) of the UC nanoparticles. 84
- Figure 5.10 Simplified energy transfer diagram of the UC nanoparticles under continuous wave (CW) 980 nm laser excitation..... 85
- Figure 5.11 Room temperature UC photoluminescence spectra of $\text{KLu}_2\text{F}_7: x\% \text{Yb}^{3+}, 2\% \text{Er}^{3+}$ ($x=18-98$) UC nanoparticles after the thermal annealing process..... 87
- Figure 5.12 (a) Before and (b) after the thermal annealing obtained through the excitation of 980 nm with different laser pulse excitation with pulsewidth from CW to 6 ns. 88
- Figure 5.13 Proposed energy transfer process of $\text{KLu}_2\text{F}_7:\text{Yb}^{3+}, \text{Er}^{3+}$ UC nanoparticles under 980 nm short and long pulsed laser excitation. UC emission spectra of $\text{KLu}_2\text{F}_7:38\% \text{Yb}^{3+}, 2\% \text{Er}^{3+}$ UC nanoparticles..... 89
- Figure 5.14 UC photoluminescence spectra of the $\text{KLu}_2\text{F}_7:38\% \text{Yb}^{3+}, 2\% \text{Er}^{3+}$ UC nanoparticles under the excitation of 980 nm in 298K (room temperature) and 77K. . 90
- Figure 5.15 (a) Time-dependent Er^{3+} emission profiles of the $\text{KLu}_2\text{F}_7:38\% \text{Yb}^{3+}, 2\% \text{Er}^{3+}$ UC nanoparticles after the thermal annealing at 543 and 668 nm upon a pulsed excitation at 980 nm with a duration of 10 ms. (b) Corresponding R:G emission intensity ratio measured as a function of excitation duration. 91
- Figure 5.16 Power dependence of the red to green UC emission intensity ratio after the thermal annealing under the excitation of CW 980 nm laser and a pulsed laser (6ns). 92



- Figure 5.17 (a) Lasing spectra of a microcavity using $\text{KLu}_2\text{F}_7:38\% \text{Yb}^{3+}, 2\% \text{Er}^{3+}$ UC nanoparticles as the gain medium under 980 nm pulse laser excitation at room temperature. The inset shows the photo of the laser microcavity. (b) Output power and emission linewidth *versus* excitation power. (c) Measured values of P_{th} and $\Delta\lambda$ *versus* D for the green emission based on the lasing microcavity. 93
- Figure 6.1 Schematic diagram of the single nanoparticle photoluminescence measurement setup. PMT1, PMT2: photomultiplier tubes; M is Ag reflection mirror, L1 and L2 are Lens; F is filter, F1: 975 nm band-pass Filter; F2: 550nm short-pass Filter; F4: 654nm band-pass Filter; GM: Galvanometer scanning mirrors; DM1: 975 nm short-pass dichroic mirror; DM2: 550nm short-pass dichroic mirror; DM3: 654 nm long-pass dichroic mirror. 99
- Figure 6.2 (a) XRD patterns of $\text{LuF}_3: \text{Yb}^{3+}, \text{Er}^{3+}$ nanoparticles at different synthetic temperature and (JCPDS No.32-0612). TEM images of $\text{LuF}_3: \text{Yb}^{3+}, \text{Er}^{3+}$ nanoparticles at different reaction temperature. (b) 280 °C, (c) 290 °C, (d) 300 °C, (e) 305 °C, (f) 310 °C. The scale bars are 50nm. 100
- Figure 6.3 TEM images $\text{LuF}_3: \text{Yb}^{3+}, \text{Er}^{3+}$ nanoparticles at 290 °C for (a) 60, (b) 90, (c) 120, and (d) 150 mins reaction time. Scale bars, 50nm. (e) Photoluminescence spectra of the LuF_3 nanoparticles under CW 980 nm excitation at room temperature. 101
- Figure 6.4 (a) HRTEM and (b) SAED images of a $\text{LuF}_3: \text{Yb}^{3+}, \text{Er}^{3+}$ nanoparticles obtained under the optimized fabrication conditions. (c) Atomic-resolution crystal structure image



- of the as-synthesized LuF_3 UCNC. The inset is the magnifying diagram of olive rectangular and the orange circles present the single atoms. The atomic model of (d) and (e) are the corresponding regions as indicated by arrows in (c) respectively. (f) Energy transfer of the UC diagram of the Yb^{3+} - Er^{3+} co-doped UC nanoparticle. UC nanoparticle absorbs NIR light and emits UC green and red emissions. Violet line is the nonradiative transitions..... 103
- Figure 6.5 (a) HAADF-STEM image of the LuF_3 amorphous cluster, the inset is the FFT. (b) EDS spectrum of $\text{LuF}_3: \text{Yb}^{3+}, \text{Er}^{3+}$ amorphous clusters when the sample reaction time is 30min. It can be confirmed that there are also K, Lu, F, Yb, Er elements. 104
- Figure 6.6 (a) Sequential time-resolved *in-situ* TEM images showing the crystallization process of $\text{LuF}_3: \text{Yb}^{3+}, \text{Er}^{3+}$ single nanoparticle. (b) Sequences of *in situ* TEM images indicate the growth of LuF_3 . The scale bar is 2nm. (Electron beam density, 4.8 A/cm^2). 105
- Figure 6.7 Sequential *in situ* HR-TEM images shown the details particle attachment process of the two nanoparticles with the assistance of the amorphous nanoclusters at the edges of the nanoparticles. Scale bar is 5nm. 107
- Figure 6.8 Sequential time-resolved *in situ* TEM images showing the process of growth based on amorphous clusters. Scale bar is 5nm. 107
- Figure 6.9 Schematic illustration of the co-precipitation and the thermal annealing method for the synthesis of LuF_3 nanoparticles..... 108



Figure 6.10 (a) Typical TEM, (b) HR-TEM image and (c) the size distribution of LuF₃: Yb³⁺, Er³⁺ nanoparticles after the thermal annealing process at 240 °C for 90 min. 109

Figure 6.11 (a) Raman spectra; (b) the emission spectra of LuF₃: Yb³⁺, Er³⁺ nanoparticles, and (c) the emission intensity changes under CW 980 nm excitation at room temperature (The pink and blue lines represent the nanoparticles before and after the thermal annealing process respectively). 110

Figure 6.12 The mechanism of the thermal annealing method on the revised surface defect, green and orange spheres are the amorphous cluster and crystallized phase respectively. (b) and (c) show a super-resolution image of Yb³⁺-Er³⁺ co-doped LuF₃ nanoparticles before and after the thermal annealing method captured by using super-resolution microscopy and the three-dimensional representation of the wide-field UC emission image under CW 980 nm excitation. (d) And (e) show the intensity recording over the number of scans under CW 980 nm excitation solely for the selected areas..... 111



List of Tables

Table 2.1 Recent development of Ln^{3+} -doped single bulk crystal UC lasers	17
Table 2.2 Recent development of Ln^{3+} -doped fiber UC lasers.....	21
Table 2.3 Recent development of Ln^{3+} -doped microsphere UC lasers	26
Table 2.4 Recent development UC lasers using Ln^{3+} -doped UC nanoparticles as the gain media.....	29
Table 4.1 The refractive indices of MgF_2 , Ag, SiO_2 at different wavelengths.....	58



List of Abbreviations

UV	Ultraviolet
NUV	Near-ultraviolet
ESA	Excited-state absorption
ETU	Energy transfer upconversion
PA	Photon avalanche
EMU	Energy migration-mediated upconversion
RGB	Red/green/blue
XRD	X-ray diffraction
TEM	Transmission electron microscopy
SEM	Scanning electron microscope
HR	High resolution
CW	Continuous wave
FP	Fabry-Perot
WGMs	Whispering gallery modes
NIR	Near-infrared
SPR	Surface plasmon resonance
UC	Upconversion
HAADF	High angle annular dark field
STEM	Scanning transmission electron microscopy
FFT	Fast Fourier transform
SAED	Selected area electron diffraction
EBT	Energy back transfer
CR	Cross relaxation
ET	Energy transfer
EDS	Energy-dispersive X-ray spectroscopy
Ln ³⁺	Lanthanide



1. Introduction

1.1 Background

Upconversion (UC) process involves the transfer of light from long- to short-wavelength (i.e. the increase of photon energy).[1] The concept of UC in multiple energy level systems was first proposed by Bloembergen in 1959.[2] UC emission is achieved via energy transfer between lanthanide (Ln^{3+}) ions and the wavelength of the UC process is controlled by the selection of suitable rare-earth dopants. In addition, the use of suitable host crystal lattices has a significant role to obtain effective UC process. This is because the crystal lattice can influence the f - f electronic transition of the dopants and shows strongly effect on the energy exchange interaction between the dopants. Therefore, the UC emission characteristics are dependent on the use of Ln^{3+} ions as well as the host matrix materials.

Trivalent rare-earth ions such as Er^{3+} , Tm^{3+} , Yb^{3+} , Ho^{3+} , Pr^{3+} , etc. are promising sensitizers/activators to obtain UC luminescence under infrared (IR) excitation. Figure 1.1 shows the energy transfer diagram of different rare-earth ions.[3] It is noted that each rare-earth ion supports multiple emission wavelengths and different rare-earth ion has different emission energy (or different emission wavelength). Furthermore, rare-earth ions have relatively discrete energy levels, the linewidth of the corresponding emission wavelength is much narrow than that of the semiconductor materials. Hence, due to the rich of the emission wavelength from IR to ultraviolet (UV) and relatively narrow linewidth of the emission spectra, rare-earth ions show enormous applications such as light emitting displays and lasers.



high UC efficiency, or which materials are suitable to be used as the laser gain medium. To the best of our understanding, there is no detailed study on the design of high-performance UC lasers has been recently reported and hence this is the motivation of my Ph.D. study.

1.2 Objectives of research

Ln^{3+} ions doped UC luminescence fluoride-based materials have been used to produce multi-colors emission because of their abundant amount of energy levels. It is believed that RGB (red/green/blue) colors can be obtained by modulating the concentration and different ratio of activator ions (e.g. Er^{3+} , Tm^{3+} , Ho^{3+} , Yb^{3+} , and Eu^{3+}) to generate UC white-light emission. Hence, the first objective of this thesis is to demonstrate the possibility of realizing UC white-light lasers by using rare-earth ions doped $\beta\text{-NaYF}_4$ hexagonal microrods as the laser cavity.

Relatively low UC emission efficiency is one of the challenges, which should be overcome for the achievement of lasing emission from using Ln^{3+} -doped materials as the laser gain medium. Therefore, the second objective of this thesis is investigating and deducing different methods to improve the UC lasing efficiency of Ln^{3+} -doped UC lasers.



1.3 Outline of the thesis

In this thesis, we propose to use Ln^{3+} -doped UC crystals, including the micro- and nanoparticles, to obtain effective multi-wavelength lasing emission under NIR excitation at room temperature. This thesis is organized as follows:

In chapter 2, the development and history of Ln^{3+} -doped UC lasers are reviewed. The strategies to overcome the limitations and problems of UC lasers are proposed.

In chapter 3, Ln^{3+} (i.e. Yb^{3+} , Er^{3+} , and Tm^{3+})-doped $\beta\text{-NaYF}_4$ hexagonal microrods are used to support UC lasing emission under NIR laser excitation. A single $\beta\text{-NaYF}_4$ hexagonal microrod is utilized as the gain medium and resonator to support whispering gallery modes (WGMs) and obtain multi-wavelength lasing emission under the 980 nm ns-pulsed laser excitation. In order to maximize the UC laser emission, the corresponding Ln^{3+} ions concentration is optimized with a suitable selection of the size of the microcavities. We demonstrate that the lasing colors from blue to green, red and white can be achieved from the single $\beta\text{-NaYF}_4$ microcavities.

In chapter 4, we propose to employ the plasmonic effect to enhance the UC efficiency and reduce the value of the lasing threshold from the Ln^{3+} -doped single $\beta\text{-NaYF}_4$ hexagonal microrods. Here, Ag film is used to excite the plasmonic effect. Our results show that the spontaneous emission of UC intensity can be increased by more than 10 times and the values of the lasing threshold can be decreased by 50%. Here, we note that the UC improvement is because of the optical coupling between the WGMs and the surface plasmonic resonance (SPR) modes.



In chapter 5, we demonstrate that the suppression of surface-related deactivations in Ln^{3+} (i.e. Yb^{3+} , Er^{3+}) -doped UC KLu_2F_7 nanoparticles can improve the corresponding UC efficiency. The influence of surface-related deactivations on the lasing characteristics of the nanoparticles is also investigated. In the study, we show visually that the improvement of UC photoluminescence is mainly due to the suppression of surface-related deactivations of the nanoparticles. This can be done by using aberration corrected high angle annular dark field (HAADF) scanning transmission electron microscopy (STEM) to directly observe the surface conditions of $\text{KLu}_2\text{F}_7:\text{Yb}^{3+},\text{Er}^{3+}$ bare core UC nanoparticles in atomic scale. Due to the very thin and uniform thickness of the nanoparticles, we observe unambiguously that the removal of surface defects enhances UC photoluminescence. The realization of dominant green lasing emission under 980 nm ns-pulsed laser excitation further confirm the high crystallinity of the nanoparticles after using the thermal annealing method.

In chapter 6, we investigate the growth process of UC $\text{LuF}_3:\text{Yb}^{3+}, \text{Er}^{3+}$ nanoparticles by using *in situ* transmission electron microscopy (TEM) imaging technique to deduce the corresponding surface defects restoration mechanism. We verify that the enhancement of UC intensity can be realized when the particles surface clusters are changed from the amorphous state to the crystallized state. Because the amorphous clusters at the amorphous acting as the defect centers would suppress the UC energy transfer process. Hence, it is shown that the enhancement of UC emission intensity from the $\text{LuF}_3:\text{Yb}^{3+}, \text{Er}^{3+}$ nanoparticles can be attributed to the removal of surface defects by using the thermal annealing method.



Chapter 7, theoretical investigations and experimental results of my Ph.D. work are summarized. The future development and potential applications of Ln^{3+} -doped deep ultraviolet (UV) UC lasers are discussed.



2. Literature review of Ln^{3+} -doped UC lasers

2.1 Introduction

Upconversion (UC) stimulation, which provides a simple alternative to non-linear optical technology for converting infrared light to visible and deep-ultraviolet (NUV) lasing, was first developed in 1971.[6] This type of lasers finds a broad area of applications including solid-state displays, underwater surveillance, diverse and so on. The mechanism of UC involves energy transfer processes from low to high energy states. Thus, the UC process requires multiple photon absorption in order to achieve radiative recombination at higher energy states. An efficient UC laser requires the presence of a metastable state, which acts as an intermediated state, between the ground and excited states.[7] Hence, a suitable selection of hosts and dopants are an important procedure to realize UC lasers with desired optical characteristics. In this chapter, UC energy transfer mechanisms and the UC lasing characteristics of the recent development of lanthanide (Ln^{3+})-doped lasers (i.e. bulk crystal, fiber, micro or nanoparticles) are discussed in detail.

2.2 The UC mechanisms

UC process converts near-infrared (NIR) light to higher energy photon emission through four distinct processes which are characterized by mechanisms of photon absorption and energy transfer. Excited-state absorption (ESA), energy transfer upconversion (ETU), photon avalanche



(PA) and energy migration-mediated upconversion (EMU) are the four UC processes that can be used to support UC lasing under NIR light excitation.[8]

2.2.1 ESA mechanism

As shown in Figure 2.1, the excited-state absorption accelerates the inverted population of carriers to the higher energy levels through sequential absorption of two photons from single ions is called ESA. The first absorbed photon (absorption path *a*) inverted populates to a long-lived metastable state E1 and then the second absorbed photon (absorption path *b*) is absorbed to promote carriers at the metastable state (level E1) to a higher energy state (level E2). The radiative transition from level E2 to ground state contributes to high energy UC emission. Hence, ESA is also called two-step absorption.

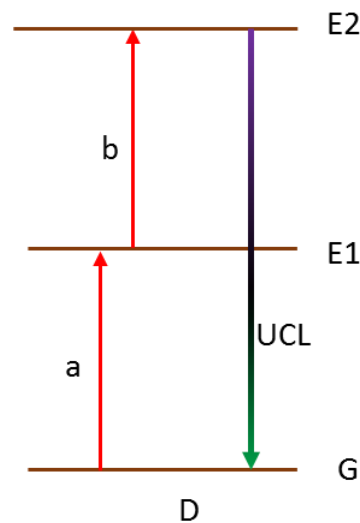


Figure 2.1 The ESA mechanism of the UC laser process. “a” and “b” shows the two pump sources.



As the ESA process involves the use of single Ln^{3+} ion doping and more than one radiative transition can be supported, those lead to a relative low UC emission efficiency. The other problem of the ESA process is that the energy of the two absorbed photons “*a*” and “*b*” are in general different (see also chapter 2.3.1). Therefore, two pumping sources, which should be overlapped on the optical materials along the entire propagation pathway, are required to support the ESA process.[9] For the pumping sources in pulsed operation, the two pumping sources should also be synchronized perfectly to achieve population inversion in level E2. In addition, the polarization of the pumping sources should be carefully controlled during the pumping process. Thus, the ESA process is a bit difficult to be implemented for practical applications.

2.2.2 ETU mechanism

ETU mechanism, which was first proposed by Auael in 1966, allows photons to be absorbed by the donor ions and then transferred energy to the adjacent acceptor ions.[10] The donors and acceptors are two different Ln^{3+} ions with energy matching during the energy transfer process. Under optical excitation, the transitions from ground to excited states of the donor ions occur due to absorption of a photon. The population in excited either decays to the ground state or transfer its energy to level E1 of the acceptor ions and then excites to level E2 by the cooperation energy transfer process. The rapid relaxation from level E2 to the ground state of the acceptor ions contribute to the UC emission, see Figure 2.2.

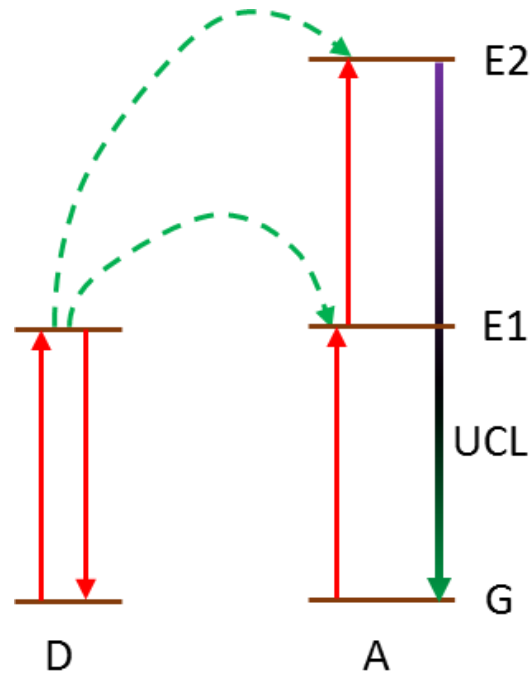


Figure 2.2 The ETU mechanism for two Ln^{3+} ions doped UC mechanism. “D” and “A” are donor and acceptor ions, respectively.

Here, Yb^{3+} is a typical donor allows effective absorption of NIR photons. The donor ions cooperatively transfer its energy by one or more steps to the adjacent acceptor ions such as Er^{3+} or Tm^{3+} ions. In the ETU process, energy transfer efficiency can be maximized by optimizing the dopants concentration.[11] In addition, by increasing the concentration of the dopants, the distance between the donors and acceptors can be decreased, resulting in the development of the energy transfer process. The radiative transition process is mainly mediated by photons so that the matrix host with low photons energy can promote energy transfer efficiency. Therefore, the choice of the matrix host is also very important for improving UC efficiency. One of the advantages to realize



UC emission via ETU is only a single excitation wavelength is required to implement the UC process.

2.2.3 PA mechanism

PA process, which involves donors and acceptors ions in the energy transfer process, is the most effective UC mechanism and was first discovered by Chivian and co-workers.[\[12\]](#) Figure 2.3 shows a schematic mechanism of the energy transfer process based on PA mechanism with the presence of donors and acceptors. Below the PA threshold, the population (for the donors) at the intermediate state level E1 is produced based on the ESA process and the neighboring excited ion pair relaxation. There is mismatching between the pump energy and the energy gap from the ground state to the intermediated state level E1. The cross relaxation dominates the energy transfer between the excited ions (donor ions) and the neighboring ground state ions (acceptor ions). Therefore, the intermediate level for donors and acceptors can be produced effectively. When the excitation value exceeds the PA threshold, the intermediated state level E1 and the excited state level E2 would be excited via the repeat process. Finally, the UC emission occurs when the carriers at the level E2 relax into the ground state.

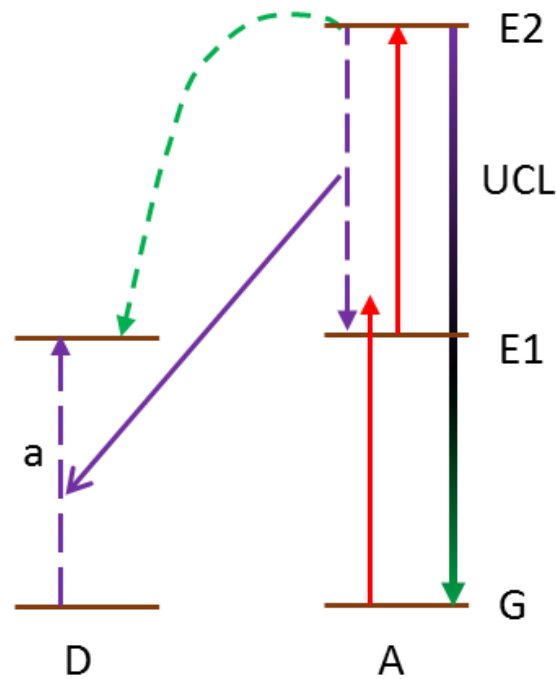


Figure 2.3 Photon avalanche UC emission in Ln^{3+} -doped materials. “D” and “A” are donor and acceptor ions, respectively.

The requirement of the PA process is that the metastable state (E1 level) should have two ions to support photon absorption (to level E2) and subsequent energy transfer process (to level E1). Under appropriate excitation situation, the two ions can form four, eight, etc., which can produce photon avalanches at the metastable levels. The PA process requires a minimum pump intensity and is characterized by a pump threshold. Here, it should be noted that the PA process shows a very high-efficiency UC emission because of the high density of acceptors (ground state) that naturally surrounding each donor.[13-15] But, the major challenge of PA mechanism in practical

applications is the low absorption of the pump photons due to the low steady-state density of absorbers in the metastable level.[16, 17]

2.2.4 EMU mechanism

EMU mechanism is characterized by the migration (or hopping) of excitation energy via the migratory ions sub-lattice. Once the acceptor ions are located far away from donor ions, the UC process could occur under the assistance of the energy migration medium. Liu's group first proposed the EMU process on the $\text{NaYF}_4@ \text{NaGdF}_4@ \text{NaGdF}_4$ core-shell-shell nanoparticles and Ln^{3+} -doped $\text{NaGdF}_4@ \text{NaGdF}_4$ core-shell nanoparticles.[18, 19] To produce high efficient EMU process, the arrays of the migrator ions via the core-shell structure are introduced to improve the energy transfer process from the donors to the acceptors. The important characteristic of the EMU process is that the excited energy absorbs by the donors should be maintained by the energy transfer process to the acceptor ions.

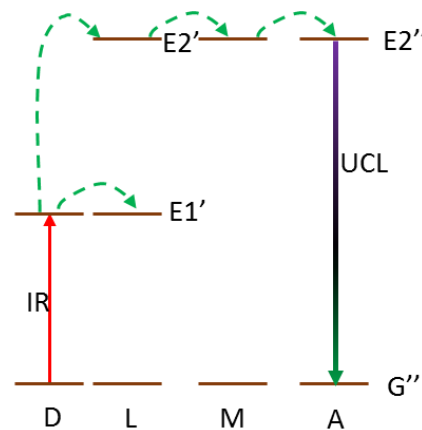


Figure 2.4 EMU mechanism process of the UC process in Ln^{3+} -doped materials. “D”, “L”, “M” and “A” are donor, migrate, migrate and acceptor ions, respectively.



Figure 2.4 shows the EMU process of the Ln^{3+} -doped core-shell nanoparticles. In the core-shell nanoparticles, the energy migrates ions (“L” and “M”) are located at the sub-lattices and the acceptor ions (“A”) are embedded inside the host lattices. Initially, donor ions (“D”) absorbs multi-photon from the pump light to achieve population inversion from ground state to excited state. Then, the donor ions transfer its accumulated energy to the first migrator ion (“L”), as well as to the second migrator ion (“M”) through the layer-interface between the core and shell. Finally, the energy is transferred to the acceptors (activator such as Dy^{3+} , Sm^{3+} , Tb^{3+} , Eu^{3+}) via the shell-shell interface. As a result, UC emission is obtained from the acceptor ions via radiative recombination between level “E2” and the ground state “G”.

2.3 The Ln^{3+} -doped UC lasers

The above UC processes have been applied to realize UC lasers with cavities fabricated by bulk crystals, fibers, microspheres, and nanoparticles. In the following section, we reviewed the development of these four types of lasers in detailed.

2.3.1 The Ln^{3+} -doped bulk crystal UC lasers

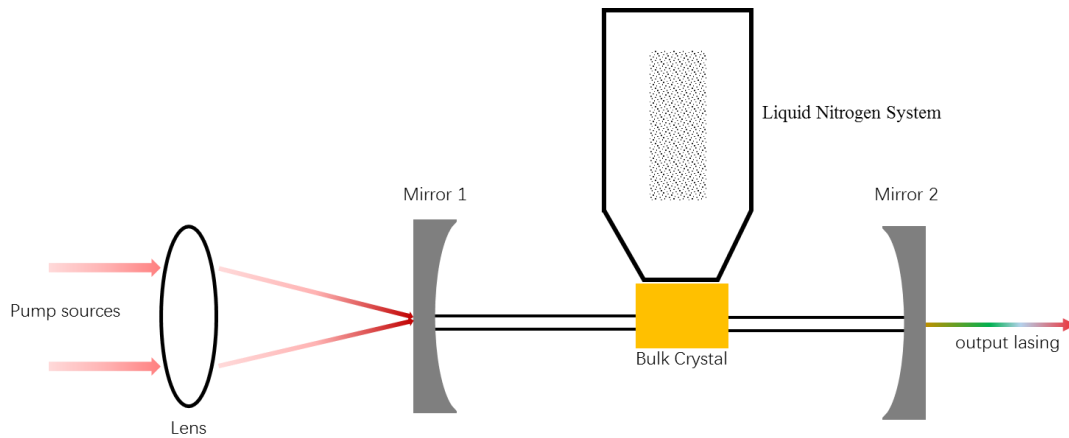


Figure 2.5 A sample diagram of Ln^{3+} -doped bulk crystal UC lasers resonator.

Figure 2.5 shows a typical schematic diagram of a UC laser using Ln^{3+} -doped single crystal as the laser gain medium. In order to obtain lasing emission, a Fabry-Perot (FP) resonator is formed by using two dielectric mirrors. Pump light is focused into the crystal through the left-hand-side mirror to realize the optical gain. Lasing light is collected from the other mirror on the right-hand side of the resonator. A cooler is directly connected to the bulk crystal to maintain its operating temperature at 77 K. The first Ln^{3+} -doped bulk crystal UC laser was reported by Johnson and Guggenheim in 1971.[6] They used monoclinic BaY_2F_8 bulk crystal as the UC matrix host, Yb^{3+} as the donor ions and $\text{Er}^{3+}/\text{Ho}^{3+}$ as the acceptor ions to achieve ETU process. The laser was pumped by Xeon flash lamp at 77 K and red/green pulsed lasing was obtained due to population inversion from the metastable levels of $\text{Er}^{3+}/\text{Ho}^{3+}$ ions. The first continuous wave (CW) UC laser (emission



at 550 nm) was demonstrated in 1987 by using Er^{3+} doped YAlO_3 crystal as the gain medium.[\[20\]](#) The laser was pumped by a dual wavelength dye laser and operating at a temperature below 77 K.

Table 2.1 lists the recent advancement of UC lasers by using the bulk crystals as the gain media. It is noted that the operating temperature of the early developed UC lasers was at or below 77 K. One of the reasons for the low-temperature operation may be due to the excess heating accumulation, which suppresses population inversion at the metastable state of acceptor ions, at the bulk crystal under CW excitation. On the other hand, the recent development of room temperature UC lasers was mainly in pulsed lasers operation. Hence, the heating effect has a significant influence on the operation characteristics of the bulk crystal UC lasers.

Dual-wavelength pumping scheme is mainly used to achieve ESA process for the realization of UC lasing when using the single-ions doped bulk crystal as the gain medium (see also in chapter 2.2.1). For example, the dual-wavelength dye laser is used to pump $^4\text{I}_{15/2}$ to $^4\text{I}_{9/2}$ state and $^4\text{I}_{11/2}$ to $^4\text{F}_{5/2}$ intermediated state of Er^{3+} ions simultaneously to obtain 549 nm green lasing emission. It is noted that the performance of the single-doped UC lasers is dependent significantly on the spatial overlap of the two-pump sources. If there is a mismatch of radial intensity, the UC lasing emission would be limited or difficult to be obtained. The reason for the popularity of using the ESA process to achieve lasing from bulk crystal UC lasers may be due to the simplification of the growth of the bulk crystal. This is because only a single dopant is required to be introduced on the host system.

Table 2.1 Recent development of Ln³⁺-doped single bulk crystal UC lasers

<i>Host</i>	<i>Dop.</i>	<i>l</i>	<i>T</i>	<i>Pump source</i>	<i>Threshold</i>	<i>Output light</i>	<i>Peak power</i>	<i>Mech.</i>	<i>Eff.</i>	<i>Year Pub.</i>	<i>Ref.</i>
BaY ₂ F ₈	Yb, Er /Ho		77 K	Xenon flash lamp	170/355 J	670/550 nm		ETU		1971	[6]
YAlO ₃	Er	3 mm	< 77 K	CW DLs 792+839 nm	100-150 mW	550 nm, CW	1 mW	ESA	0.5%	1987	[20]
YAlO ₃	Er	3 mm	< 90 K	CW DL 792 +839 nm	80 mW	550 nm, CW	0.5-5 mW	ESA	0.2%	1988	[21]
LaF ₃	Nd	3 mm	20 K	CW DL 578 nm	230 mW	380 nm, CW	12 mW	ESA		1988	[22]
YLiF ₄	Er	2 mm	40 K	CW DL 797nm	17 mW	551 nm, CW	4.2 mW	ESA	3.2%	1989	[23]
YLiF ₄	Tm	10 mm	75 K	Pulsed DL 649 + 780	4 J/cm ²	450 nm, pulsed	180 μJ	ESA	1.3%	1989	[24]
YLiF ₄	Er	3.5 mm	16 K	CW DL 653nm	10 mW	469nm, CW	6 mW	ESA	4.6%	1990	[25]
YLiF ₄	Er	3.5 mm	10 K	Chopped SSL 969 nm	170 mW	469 nm, pulsed	2 mW	ESA	0.2%	1990	[25]
YLiF ₄	Er	2 mm	77/50 K	CW diode laser 802 nm	48/22 mW	551 nm, pulsed	0.5/2.3 mW	ESA	2/3%	1990	[26]
YLiF ₄	Tm	20 mm	RT	Flashlamp pumped DL 781+649 nm	2.6 J/cm ²	453 nm, pulsed		ESA		1990	[27]



YLiF ₄	Er	3 mm	< 80 K	Chopped CW SSL 1500 nm	50 mW	560, 551, 460 nm, pulsed	12 mW	ESA	1992	[28]
YLiF ₄	Tm	3 mm	70 K	CW SSL 784nm + DCM DL 648 nm	10-50 mW	450 nm, pulsed	10 mW	ESA	1992	[29]
BaY ₂ F ₈	Yb, Tm	0.4 - 1.0 mm	RT	Chopped CW diode- laser 960 nm	70/190 mW	649 nm /456, 512 nm, pulsed		ETU	1994	[30]
YLiF ₄	Er	6.9 mm	RT	Pulsed SSL 810 nm + CW 647 nm		551 nm, pulsed	0.95 mJ	ESA	1993	[31]
BaY ₂ F ₈	Yb, Tm	0.5 mm	RT	Chopped CW SSL 960 nm		348 nm, pulsed		ETU	1994	[32]
YAlO ₃	Er	10 mm	7 K	CW SSL 960 nm	3 mW	550 nm, pulsed	33 mW	PA	3.5%	1995 [33]

Dop. – Dopants, *l* – Crystal length, *T* – Temperature, *Mech.* – Mechanism; RT – Room temperature, *Eff.* – Efficiency; CW – Continuous-wave, DL – Dye laser, SSL – Solid-state laser.

2.3.2 The Ln^{3+} -doped UC fiber lasers

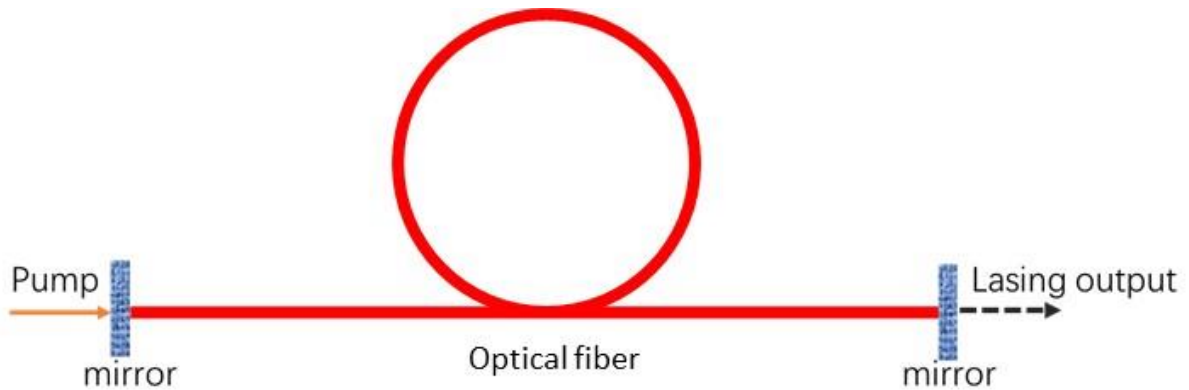


Figure 2.6 A sample diagram of Ln^{3+} -doped fiber UC lasers resonator.

Figure 2.6 shows a typical configuration of the UC fiber laser [34]. The core of the optical fiber is doped with Ln^{3+} ions. The laser cavity of the UC fiber laser is formed by using two termination mirrors located at the two ends of the fiber. Light coupled into the fiber through the left-hand side of the mirror is used to excite the gain medium of the fiber. Lasing emission is obtained from the right-hand-side mirror of the fiber laser.

The fiber core composes of heavy metal fluoride-doped glass, with which the dopants are Lu^{3+} , Pr^{3+} , Nd^{3+} , Ho^{3+} , Er^{3+} , and Tm^{3+} ions, can produce high-efficient room temperature UC laser. The most common fiber material used to fabricate the UC fiber laser is the fluorozirconate (ZBLAN) glass. This is because ZBLAN has narrow phonon spectra and low optical absorption loss at room temperature. In addition, the ZBLAN glass has board transmission window, low dispersion for the optical photon, and low refractive index.



The first UC laser fiber was demonstrated in 1990 using Tm^{3+} doped ZBLAN as the core of the fiber. Dual pumping (647+676 nm) excitation was used to excite the 1.7 m long fiber.[34] Lasing emissions were observed at 455nm ($^1\text{D}_2 \rightarrow ^3\text{F}_4$ transition) and 480 nm ($^1\text{G}_4 \rightarrow ^3\text{H}_6$ transition) based on the ESA process at 77 K under pulsed operation. The first room-temperature CW lasing emission was reported in the same year by using 1 m long ZBLAN fiber doped with Ho^{3+} ions.[35] As we can see, the suppression of heat effect is due to the long interaction length as well as the strong optical confinement structure of pumped and gain region of the fiber. Hence, UC fiber lasers can produce the stimulated CW lasing emission at room temperature.

Over the past few years, higher optical performance and shorter lasing wavelength have also been realized from UC fiber lasers. Table 2.2 reviews the recent development of Ln^{3+} -doped UC fiber lasers. The UC fiber lasers show higher efficiency and better control of wavelength tunability than that of the bulk crystal UC lasers. The remarkable performance of the fiber lasers is due to 1) long pump/gain medium interaction length of fiber host, and 2) strong optical confinement. According to Table 2.2, the ESA mechanism is also a popular mechanism in the realization UC fiber lasers. This may be due to the simplification of the growth of doped glass fibers as only one dopant is required to introduce on the host system.

Table 2.2 Recent development of Ln³⁺-doped fiber UC lasers

<i>Host</i>	<i>Dop.</i>	<i>CD</i>	<i>l</i>	<i>T</i>	<i>Pump source</i>	<i>Threshold</i>	<i>Output light</i>	<i>Peak power</i>	<i>Mech.</i>	<i>Eff.</i>	<i>Year Pub.</i>	<i>Ref.</i>
ZBLAN	Tm	3 μm	1.7 m	77 K	CW Krypton ion laser 676+647 nm	90 mW	455, 488 nm, pulsed	0.4 mW	ESA		1990	[34]
ZBLAN	Ho	2.7 μm	1.0 m	RT	CW Krypton ion laser 647 nm		540, 553 nm, CW	10 mW	GSA +ESA	3.5 %	1990	[35]
ZBLAN	Er		2.4 m	RT	SSL 801nm	100 mW	546 nm, CW	23 mW	ESA	5 %	1991	[36]
ZBLAN	Pr		1.2 m	RT	CW SSL 1010+835nm	200 mW	635 nm, CW 605 nm, CW 520/491 nm, CW	180 mW 30 mW 1 mW	ESA	10 % 3.3 %	1991	[37]
ZBLAN	Er	0.8 μm		RT	CW diode laser 1112- 1123 nm	46 mW	480 nm, CW	57 mW	ESA		1992	[38]
ZBLAN	Ho	11 μm	0.22 m	RT	CW DL 640-653 nm	128 mW	546-550 nm	12 mW	ESA	3.9 %	1993	[39]
ZBLAN	Yb, Pr	5.7 μm	1.2 m	RT	SSL 800 nm	70 mW	635nm, CW	25 mW	ET	7 %	1991	[40]
ZBLAN	Tm	3 μm	1.6 m	RT	CW diode laser 1135 nm	22 mW	482 nm, CW	5 mW	ESA		1996	[41]
ZBLAN	Er	1.1 μm		RT	CW diode laser 801 nm	20 mW	543 nm, CW	3 mW	ESA	7.5 %	1993	[42]



ZBLAN	Er	2.1 μm	1.5 m	RT	CW diode laser 971 nm	18 mW	544 nm, CW	11.7 mW	ESA	7.8 %	1994	[43]
ZBLAN	Tm	12 μm	0.35 m	RT	CW SSL 1064 nm	50 mW	803-816 nm, CW	1.2 W	ESA		1994	[44]
ZBLAN	Tm		1.5 m	RT	CW SSL 645+1064 nm	230 mW	455 nm, CW	3 mW	ESA		1994	[45]
ZBLAN	Pr, Yb	1.7 μm	1.7 m	RT	CW diode laser 856 nm	55 mW 85 mW	520 nm, CW 490 nm, CW	80 mW 130 mW	ETU	0.75 % 0.53 %	1996	[46]
ZBLAN	Nd	2.2 μm	0.39 m	RT	CW DL 590 nm	225 mW	412 nm, CW	0.5 mW	ESA	0.15 %	1995	[47]
ZBLAN	Yb, Pr	3 μm	0.6 m 0.6 m 0.42 m 0.26 m	RT	CW SSL 860 nm	42 mW 29 mW 21 mW 60 mW	635 nm 615 nm 520 nm 493 nm	300 mW 45 mW 20 mW 4 mW	PA	39 % 10.4 % 10 % 2 %	1995	[48]
ZBLAN	Er	6.5 μm	1 m	RT	CW HeNe laser 632nm+CW Diode laser 980 nm		402nm 407nm		ESA		1996	[49]
ZBLAN	Tm	3 μm	2 m	RT	CW Diode laser 1123 nm	800 mW	481 nm, CW	230 mW	ESA	15.6 %	1997	[50]
ZBLAN	Tm	3 μm		RT	CW Diode laser 1210 + DL 649 nm	15 mW	480 nm, CW	20 mW	ESA		1997	[51]
ZBLAN	Yb, Pr	3 μm	0.35/0. 19 m 0.045 m	RT	CW SSL 830 nm	100/450 mW 125 mW	520 nm, CW 490 nm, CW	9/3 mW 8 mW	ETU	1.5/0.37 % 1.6 %	2004	[52]



ZBLAN	Er	5.5 μm	0.45 m	RT	Pulse DL 976 nm	110 mW	543nm, pulsed	6.9 mW	ESA	30 %	2016	[53]
ZBLAN	Yb, Pr	1.3 μm	0.34 m	RT	CW diode laser 850 nm		492 nm, pulsed 520 nm, pulsed 635 nm, pulsed	10 mW	ETU	10 %	2010	[54]

Dop. – Dopants, l – Fiber length, CD – Core diameter, T – Temperature, RT – Room temperature, CW – Continuous-wave, DL – Dye laser, SSL – Solid-state laser; ZBLAN – ZrF₄-BaF₂-LaF₃-AlF₃-NaF

2.3.3 The Ln^{3+} -doped UC microsphere lasers

Figure 2.7 shows a typical configuration of a UC microsphere laser. In general, round-trip propagation of light is formed at the air-dielectric interface of the resonators through internal reflection (i.e. red arrows). Due to the strong optical confinement of light, optical loss of the microcavity can be significantly reduced if the surface roughness of the interface is negligible. [55-57] In addition, the microsphere has a high Q factor and low excitation threshold. [58-60] Hence, most of the reported microcavity UC lasers have microsphere configuration, see Table 2.3.

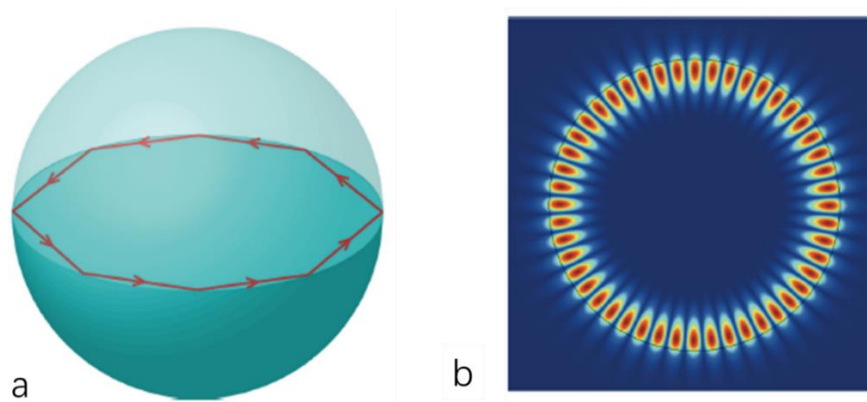


Figure 2.7 The Ln^{3+} -doped microsphere UC lasers. (a) Schematic diagram, (b) modal field.

It is reported that the realization of the low threshold and narrow linewidth UC laser can be obtained by using resonant modes with a large ratio of quality factor/volume. Therefore, microcavity resonators with a microsphere shape have been proposed. [61] The microsphere lasers show excellent optical performance such as low threshold and narrowing lasing emission linewidth.



Ln^{3+} ions (i.e. $\text{Er}^{3+}/\text{Tm}^{3+}$) doped ZBLAN is commonly used to fabricate the microspheres. The size of the microspheres varies from 30 to 120 μm . The emission wavelength of the microcavities is either green or blue in color dependent on the choice of the dopants, see also Table 2.3.

Table 2.3 Recent development of Ln^{3+} -doped microsphere UC lasers

<i>Host</i>	<i>Dop.</i>	<i>D</i>	<i>T</i>	<i>Pump source</i>	<i>Threshold</i>	<i>Output light</i>	<i>Peak power</i>	<i>Mech.</i>	<i>Year</i>	<i>Ref.</i>
ZBLAN	Er	120 μm	RT	Pulsed diode laser 801 nm	30 μW	540 nm		ESA	1999	[62]
ZBLAN	Tm	65 μm	RT	Pulsed SSL 1064 nm	20 mW	480 nm		ESA	1999	[63]
ZBLAN	Er	30 μm	RT	Pulsed SSL 800 nm	4 mW	550 nm		ESA	2002	[64]
ZBNA	Er	120 μm	RT	Pulsed diode laser 978 nm	3 μW	550 nm	50 mW	ESA	2010	[65]
ZBLAN	Yb, Er	110 μm	RT	Pulsed diode laser 978 nm	16.8 μW	550 nm		ETU	2018	[66]

Dop. - Dopants, D – Diameter, T – Temperature, RT – Room temperature, CW – Continuous wave, DL – Dye laser, SSL – Solid-state laser; ZBNA – $\text{ZrF}_4\text{-BaF}_2\text{-NaF-AlF}_3$, ZBLAN – $\text{ZrF}_4\text{-BaF}_2\text{-LaF}_3\text{-AlF}_3\text{-NaF}$



The first UC microsphere laser was demonstrated in 1999 by W. V. Klitzing, et al. They used Er^{3+} doped ZBLAN as the microsphere with a diameter of 120 μm .[\[62, 64\]](#) Diode laser at 801 nm was used to pump the microsphere. Total internal reflection from the dielectric-to-air interface of the microsphere confined the lasing modes (i.e. WGMs) of the laser. Lasing emission can be observed at 540 nm ($^4\text{S}_{3/2} \rightarrow ^4\text{I}_{15/2}$ transition) based on the ESA process at room temperature under pulsed operation. The lowest threshold was reported to be 30 μW due to the small modal volume and high finesse of the microsphere. On the other hand, the first CW UC microsphere laser emitted at a blue wavelength of 480 nm was also reported in 1999.[\[63\]](#) The diameter of the Tm^{3+} doped ZBLAN microsphere is 65 μm . Several years later, the lower threshold, higher stability, and better optical performance short wavelength UC microsphere lasers have also been realized. Table 2.3 reviews the recent development of Ln^{3+} -doped UC microsphere lasers. The UC microsphere lasers show very low threshold value than that of the bulk crystal UC lasers. The remarkable performance of the microsphere lasers is due to 1) high-quality factor, 2) small modal volume, and 3) extremely strong optical confinement. According to Table 2.3, the ZBLAN glass is the main optical medium used to fabricate UC microsphere lasers. This may be due to the difficulty of finding other materials with optical performance (i.e. low optical absorption loss, high optical damage threshold, low fabrication cost, etc.) compatible with that of ZBLAN medium.

2.3.4 The Ln^{3+} -doped UC nanoparticles lasers

Figure 2.8a shows a typical configuration of a microcavity laser using UC nanoparticles as the gain medium. Figure 2.8b shows the schematic diagram of a UC core-shell-shell nanoparticles commonly used to realize UC lasing emission. This is because the use of core-shell-shell structure significantly improves the UC efficiency - the surface passivated effect of core-shell configuration reduces the surface quenching effects and suppresses energy transfer from the dopant ions to the crystal surface.[67-71] Table 2.4 summarizes the recent investigations on the use of UC nanoparticles to realize UC lasing emission.

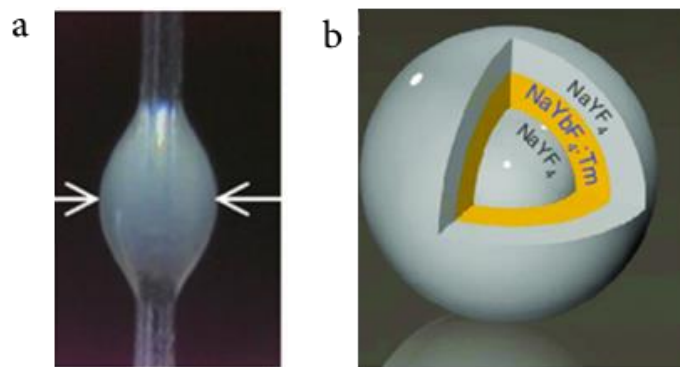


Figure 2.8 Microcavity laser based on Ln^{3+} -doped UC nanoparticles. (a) A bottle-like microcavity which is fabricated by coating a mixture of silica resin and UC nanoparticles onto an optical fiber. (b) The core-shell-shell structure of the UC nanoparticles.

Table 2.4 Recent development UC lasers using Ln³⁺-doped UC nanoparticles as the gain media

<i>Host</i>	<i>Dop.</i>	<i>D</i>	<i>T</i>	<i>Pump source</i>	<i>Threshold</i>	<i>Output light</i>	<i>Mech.</i>	<i>Year Pub.</i>	<i>Ref.</i>
NaYF ₄	Yb ³⁺ , Er ³⁺	80 μm	RT	Pulsed SSL 980 nm	8.5 kW/cm ²	408 nm			[72]
					6.5 kW/cm ²	550 nm	EMU	2013	
					5.5 kW/cm ²	655 nm			
NaYF ₄	Yb ³⁺ , Tm ³⁺	75 μm	RT	Pulsed SSL 980 nm	86 mJ/cm ²	310 nm	EMU	2016	[73]
NaYF ₄	Tm ³⁺	5 μm	RT	CW 1064 nm	45 kW/cm ² 17 kW/cm ²	450 nm 807 nm	PA	2018	[74]

Dop. - Dopants, D – Diameter, T – Temperature, Mech. – mechanism, RT – Room temperature, CW – Continuous-wave, DL – Dye laser, SSL – Solid-state laser

The first UC nanoparticles laser was demonstrated in 2013.[72] The laser cavities were fabricated by coating a mixture of silica resin and NaYF₄:Yb/Er@NaYF₄ core-shell NCs onto an optical fiber with a diameter of 80 μm. Lasing emissions at 408, 550 and 655 nm can be obtained simultaneously using 980 nm ns-pulsed laser excitation at room temperature. Subsequently, UC nanoparticles laser emitted at 310 nm was also realized by using Yb³⁺-Tm³⁺ co-doped NaYF₄ core-shell-core UC nanoparticles as the gain medium under pulsed operation at room temperature.[73] The UC process of these nanoparticles is mainly due to EMU mechanism. In 2018, CW lasing from microcavity using Tm³⁺ doped UC nanoparticles as the gain medium has also demonstrated. It must be noted that the corresponding UC mechanism is due to the PA process. The microcavities were fabricated by coating the UC nanoparticles at the polystyrene cavity surface. The threshold



of UC lasing is as low as 14 kW cm^{-2} so that CW lasing emission at room temperature can be sustained.[74] This remarkable performance of the UC nanoparticles based on the microcavities laser is due to 1) the use of NaYF_4 host,[75-78] which can promote high UC efficiency, 2) small mode volume, and 3) extremely strong optical confinement. According to Table 2.4, NaYF_4 is the only choice of nanoparticles to realize UC lasing emission. This is because NaYF_4 is found to be the most effective host to sustain UC process at room temperature.

2.3.5 Summary

During the past decades, Ln^{3+} -doped UC lasers have achieved a wide range of lasing wavelength from visible to UV, significant suppression of lasing threshold and linewidth as well as reduction of cavity size from meter long fiber to microcavity structure. This is mainly due to the improvement of optical confinement and high-optical-quality of laser cavities. Ln^{3+} ions (i.e. $\text{Er}^{3+}/\text{Tm}^{3+}$) doped NaYF_4 nanoparticles is the recent popular nanomaterial to realize UC laser. So far, the UC lasers fabricated by UC nanoparticles have shown excellent laser performance compatible with that of the semiconductor lasers.

However, the laser performance of the available developed UC lasers is still not sufficient for practical applications. For example, white-light lasers, which show to have enormous applications in white-light display, is difficult to fabricate from Ln^{3+} -doped UC nanoparticles. In addition, the reported UC efficiency of the available UC nanoparticles is still insufficient for practical applications. Therefore, it is necessary to improve the design of lasing cavities for better UC lasing



performance. In this thesis, we explained the possibilities to realize white-light laser by using UC microparticles as the lasing cavities as well as the optical gain media. We also proposed to use the plasmonic effect to improve the lasing characteristics of UC microparticles. On the other hand, we found that the reduction of surface quenching effects can suppress surface-related deactivations and improve UC efficiency of UC nanoparticles. This can be done by using the aberration-corrected high angle annular dark field (HAADF) scanning transmission electron microscopy (STEM) to study the relationship between the surface conditions and UC efficiency from the Ln^{3+} -doped nanoparticles. The growth process of Ln^{3+} -doped nanoparticles is also studied by using *in situ* transmission electron microscopy (TEM) imaging technique to deduce the corresponding surface defects restoration mechanism so that better UC efficiency can be obtained.



3. White-light WGMs lasing from Ln^{3+} -doped UC β - NaYF_4 hexagonal microrods

3.1 Introduction

The realization of white-light lasers finds novel applications such as those in the field of display technology.[\[79-82\]](#) White-light lasers show advantages over conventional white-light emitting-diodes due to their low beam divergence and high emission intensity. Therefore, they have attracted the interest of scientists on the development of practical applications such as three-dimensional optical tweezers, fluorescence microscopy, and true-color three-dimensional holograms. Furthermore, white-light lasers potentially play an important role in consumer products such as headlights and spotlights of automobiles (e.g. BMW i8), as well as laser lighting. Research and development of white-light lasers will bring revolutionary change and subversion to the application of lasers.[\[80, 83-85\]](#)

To achieve white-light lasing, the excitation of multi-color emissions based on the mixture of three primary colors red/green/blue (RGB) should be considered. Due to the ability of photons to carry energy and information, it is more advantageous to use white-light lasers as alternative light sources for optical communication and high power cutting, compared to monochromatic lasers with narrow wavelength range. The current technology to obtain white-light lasers is based on the broadening of emission range triggered by highly nonlinear optical processes through extremely high input power of light. For example, white-light pulses can be generated by focusing on high-



power femtosecond pulses a transparent material.[86] Using this technique, white-light laser sources had been commercialized as a product for scientific applications. However, the drawbacks of using nonlinear optical processes are the high production and operation cost. Recently, a monolithic multi-segment ZnCdSSe crystal-based semiconductor nanosheet, which demonstrates lasing emission in the RGB regimes, shows potential in the realization of low-cost and compact white-light laser diodes.[81] Nevertheless, it is difficult to excite red, green and blue lasing emissions simultaneously in the same lasing cavity, which poses a challenge to achieve white-light lasing emission with the UC material.

Recently, lanthanide (Ln^{3+}) rare earth -doped upconversion (UC) luminescence fluoride-based materials have been used to produce white-light spontaneous emission because of their abundant amount of energy levels.[87] As the UC emission originates from the Ln^{3+} rare earth ions, the RGB can be controlled by modulating the concentration of activator ions (Er^{3+} , Tm^{3+} , Ho^{3+} , Yb^{3+} , and Eu^{3+} and so forth), changing the excitation power or tuning the concentration of sensitizer ions (such as Yb^{3+}) within any defined location to generate white-light emission. Besides, the low cost and compact near-infrared (NIR) laser diodes can be used as the excitation sources. Therefore, we propose using Yb^{3+} , Er^{3+} , and Tm^{3+} tri-doped hexagonal-phase $\beta\text{-NaYF}_4$ microrods to produce RGB lasing under NIR excitation. The hexagonal-phase $\beta\text{-NaYF}_4$ microrods play the role as the material host to achieve energy transfer from Yb^{3+} ions to Er^{3+} ions for green and red emissions, or Tm^{3+} ions for blue emission. In addition, to achieve lasing emission, lasing cavities should be introduced. Here, the hexagonal-phase $\beta\text{-NaYF}_4$ effectively forms hexagonal cavities



for lasing emission, and by controlling their sizes, the difference in lasing threshold between the red, green and blue lasing modes can be minimized.

3.2 Fabrication methods of Ln^{3+} -doped UC $\beta\text{-NaYF}_4$ hexagonal microrods

The $\beta\text{-NaYF}_4\text{: Ln}^{3+}$ ($\text{Ln}^{3+}=\text{Yb}^{3+}/\text{Er}^{3+}/\text{Tm}^{3+}$) hexagonal microrods were prepared by hydrothermal method. The reagents include rare-earth ($\text{Ln}=\text{Yb}$, Er , Tm) oxides (99.99% purity obtained from Aladdin, China), ethylenediamine tetraacetic acid (EDTA > 99.5%, obtained from Tianjin Fengchuan Chemical Reagent Co., Ltd., China), sodium hydroxide (NaOH > 96.0%, Tianjin Fengchuan Chemical Reagent Co., Ltd., China), ammonium fluoride (NH_4F > 96.0%, Tianjin Fengchuan Chemical Reagent Co., Ltd., China) and hydrochloric acid (HCl , 12M, need to be diluted with deionized water for 1M). All chemicals are of analytical grade and were used directly without further purification.

To prepare the Yb^{3+} , Er^{3+} -doped $\beta\text{-NaYF}_4$ (1 mmol) microrods, Yb_2O_3 , Y_2O_3 , and Er_2O_3 powder were first dissolved in dilute nitrate solution and the residual nitrate was removed by heating and evaporation, resulting in the formation of a clear solution of $\text{Ln}(\text{NO}_3)_3$ ($\text{Ln}=\text{Tm}$, Yb , Er). Subsequently, 12.5 ml of an aqueous solution containing 0.4g EDTA and 1.05 ml of NaOH aqueous solution (5.0 M) were mixed under stirring until the solution becomes clear. After that, 5 ml of $\text{Ln}(\text{NO}_3)_3$ aqueous solutions (0.2 M), 8 mL of NH_4F (2.0 M) aqueous solutions and 7 ml dilute hydrochloric acid (1 M) were added to the mixture. After additional agitation for 90 min on

a magnetic stirrer, the resultant solution was transferred to a 50 mL autoclave and maintained at 200°C for 40 hours. Finally, the autoclave was cooled down to room temperature. The precipitates were separated by centrifugation, washed with deionized water and ethanol for three times, and then dried in air at 80 °C for 8 hours. Yb^{3+} and Tm^{3+} co-doped $\beta\text{-NaYF}_4$ hexagonal microrods and Yb^{3+} , Er^{3+} , Tm^{3+} tri-doped $\beta\text{-NaYF}_4$ hexagonal microrods can also be prepared by a similar process as described above with the change of rare-earth ions.

3.3 Physical and optical properties

3.3.1 Optical measurement setup

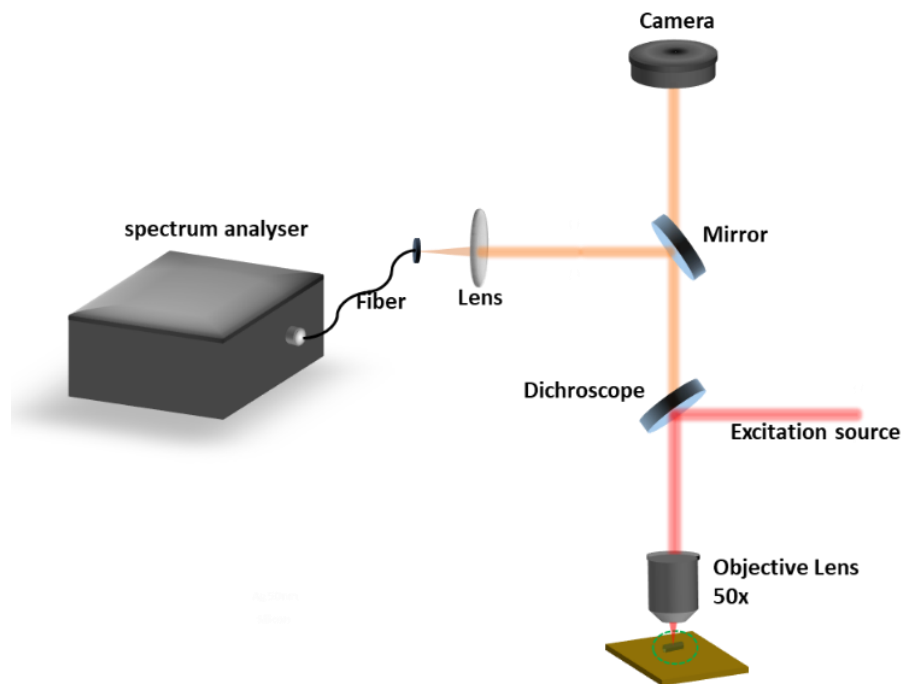


Figure 3.1 The photoluminescence and lasing characteristic measurement setup.



We used an optical microscope (Leica DM1000 LED) to measure the lasing and photoluminescence spectra, as shown in Figure 3.1. Firstly, $\beta\text{-NaYF}_4$ hexagonal microrods were dispersed in the quartz plate, and then by modulating the X-Y-Z translation stage of the optical microscope, we can control the positions of the single $\beta\text{-NaYF}_4$ hexagonal microrods. A 50×0.75 N.A. objective lens was used to observe and collect the optical information of the single $\beta\text{-NaYF}_4$ hexagonal microrods. As for the optical spectral analyzer, Oriel MS257 monochromator (i.e., spectral resolution can be changed from 0.1 nm to 5 nm, here we used the spectral resolution with 0.1 nm for maximum accuracy) attached to a photomultiplier tube was used. The dichroscope mirror used reflects NIR (800-1200 nm) and transmits visible (300-790 nm) waves. During optical measurement, the excitation source was introduced and was reflected by the dichroscope. Through the objective lens, the excitation source was focused on a single $\beta\text{-NaYF}_4$ hexagonal microrod surface. The emission from the Ln^{3+} -doped hexagonal microrods can then be collected at the same objective lens, which passes through the dichroscope and eventually reaches the spectral analyzer. All of the optical characteristics of lasers were measured at room temperature in an atmospheric environment.

To measure the lasing characteristics of the sample, a frequency-tripled 355 nm Q-switched Nd:YAG pulsed laser was used to generate 980 nm ns-pulses as the pump source. The frequency and pulse width were respectively 10 Hz and 6 ns, and the diameter of the light beam was 0.8 cm. The horizontally polarized pump laser beams were obtained by feeding the pulses from the



Nd:YAG laser into an optical parametric oscillator. As for the measurement of photoluminescence spectra, continuous wave (CW) 980 nm laser was used instead.

3.3.2 Physical properties of β -NaYF₄ hexagonal microrods

The XRD data for the β -NaYF₄ powder were recorded by using the Bruker AXS D2 phaser equipment with a graphite-monochromatized Cu K α radiation (1.5406 Å). The TEM images and elemental mapping images were measured by a JEOL-JEM 2100F transmission electron microscope operating at an acceleration voltage of 200 kV. Teledyne Leeman Labs -Prodigy Inductively coupled plasma -optical emission spectrometry (ICP-OES) with 1.1 kW power was also used to analyze the doped concentration of Ln³⁺ ions in 0.1 g of the 40% Yb³⁺, 2% Tm³⁺, 0.5% Er³⁺ tri-doped β -NaYF₄ hexagonal microrods.

The physical characteristics of the samples are shown in the following figure, Figure 3.2a-c show the SEM (scanning electron microscope) images of Ln³⁺ rare earth co-doped β -NaYF₄ microrods by changing the Ln³⁺ concentrations, and Figure 3.2d shows the corresponding XRD patterns. The SEM images show that the 100% Yb³⁺-1% Er³⁺, 20% Yb³⁺-1% Er³⁺, and 40% Yb³⁺-2% Tm³⁺ co-doped β -NaYF₄ appears in the form of microrods with hexagonal cross-sections, which facilitates the propagation of whispering gallery modes (WGMs) to support lasing emission. The XRD data also shows that we have successfully fabricated the single-phase β -NaYF₄ without the other phases by using the hydrothermal method.

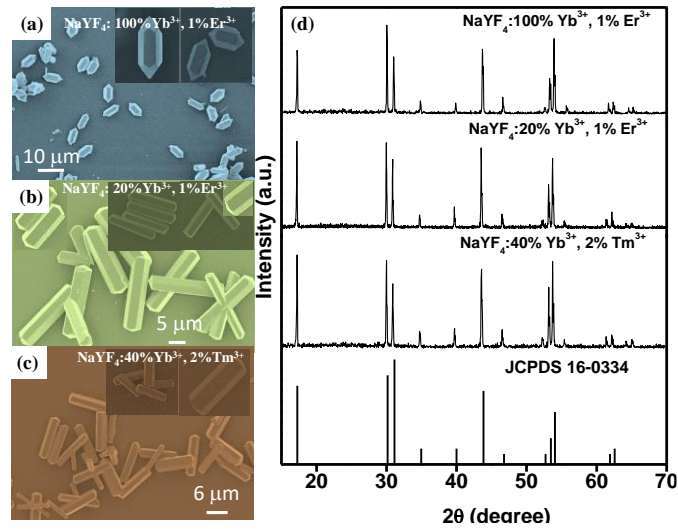


Figure 3.2 SEM images of (a) 100% Yb³⁺-1 %Er³⁺, (b) 20% Yb³⁺-1% Er³⁺ and (c) 40% Yb³⁺-2% Tm³⁺ co-doped β -NaYF₄ hexagonal microrods. (d) XRD patterns of the corresponding co-doped β -NaYF₄ hexagonal microrods.

To obtain the RGB UC lasing emissions from the same cavity, the Yb³⁺, Er³⁺, and Tm³⁺ tri-doped β -NaYF₄ hexagonal microrods were also fabricated, and their characterization results through SEM, TEM and XRD are shown in Figure 3.3. The Figure 3.3a shows the SEM image of Yb³⁺, Er³⁺, and Tm³⁺ tri-doped β -NaYF₄, it can be observed that the microscale β -NaYF₄ shows two sharp ends, with an average radius of 3 μ m (see Figure 3.4). The inset of Figure 3.3a shows the close-up view of a single β -NaYF₄ hexagonal microrod, which reveals that the β -NaYF₄ has six flat surfaces and the ends are of the hexagonal pyramid structure. Figure 3.3b is the mapping images, which confirms that each of the rare earth elements (Yb, Er, and Tm) is distributed uniformly over a single β -NaYF₄ hexagonal microrod. Figure 3.3c presents the high-resolution



TEM image measured at the edge of a single $\beta\text{-NaYF}_4$ hexagonal microrod. According to the lattice structure of the $\beta\text{-NaYF}_4$ crystal, the (001), and (100) planes can be indexed on the image, with the space group $P6_3/m$. The corresponding electron diffraction image is also shown in Figure 3.3d, which suggests that the fabricated single $\beta\text{-NaYF}_4$ hexagonal microrod is highly crystalline. The XRD patterns of $\text{Yb}^{3+}\text{-Er}^{3+}\text{-Tm}^{3+}$ tri-doped $\beta\text{-NaYF}_4$ hexagonal microrods are given in Figure 3.3e, resembling that of the $\beta\text{-NaYF}_4$ crystal (JCPDS file number 16-0334) closely.

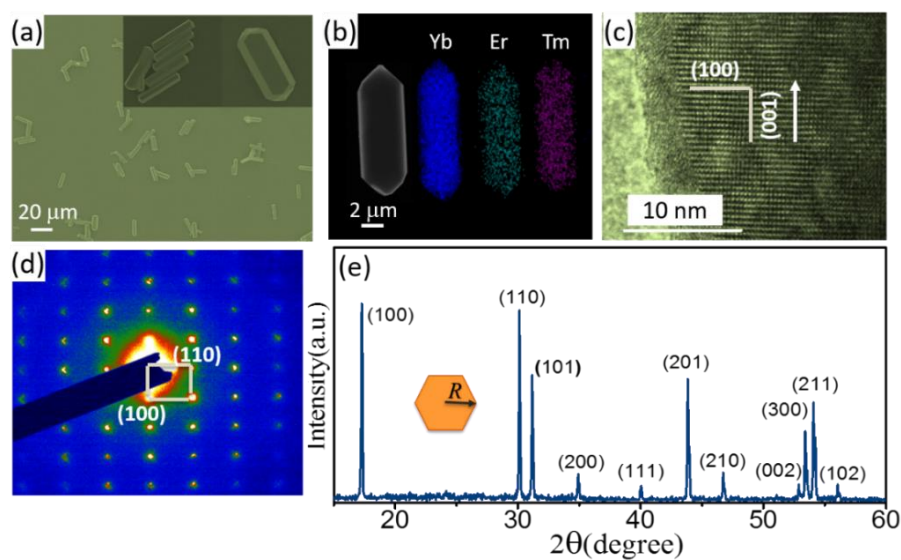


Figure 3.3 (a) SEM images of the as-synthesized Yb^{3+} , Er^{3+} , and Tm^{3+} tri-doped $\beta\text{-NaYF}_4$ hexagonal microrods. (b) Elemental mapping of a $\beta\text{-NaYF}_4$, (c) HR-TEM image of a $\beta\text{-NaYF}_4$ hexagonal microrod. (d) Electron diffraction image and (e) XRD pattern of $\beta\text{-NaYF}_4$ hexagonal microrods.

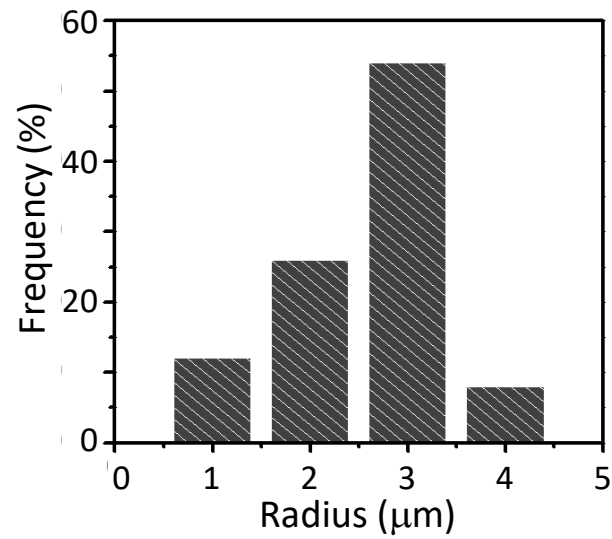


Figure 3.4 Size distribution of Yb^{3+} , Er^{3+} , and Tm^{3+} tri-doped $\beta\text{-NaYF}_4$ hexagonal microrods corresponding to Figure 3.3 a.

3.4 Photoluminescence properties of $\beta\text{-NaYF}_4$ hexagonal microrods by modulating Ln^{3+} ions doping

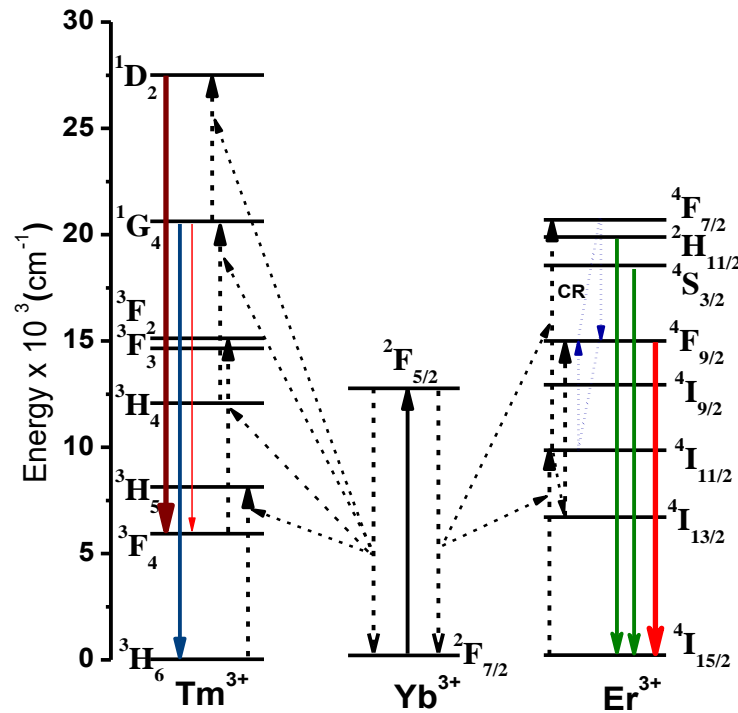


Figure 3.5 Energy level diagram of the Yb^{3+} , Er^{3+} , Tm^{3+} tri-doped $\beta\text{-NaYF}_4$ hexagonal microrod under 980nm NIR excitation. The mechanisms of the UC population, radiative and non-radiative recombination as well as cross-relaxation transitions, are indicated in the diagram.

Figure 3.5 shows the energy level diagrams of Yb^{3+} , Er^{3+} , and Tm^{3+} tri-doped $\beta\text{-NaYF}_4$ hexagonal microrods under the 980nm NIR excitation. There are numerous energy levels for the Yb^{3+} , Er^{3+} and Tm^{3+} ions. The Er^{3+} ions can lead to $^4\text{F}_{9/2} \rightarrow ^4\text{I}_{15/2}$ (654 nm -red), $^2\text{H}_{11/2} \rightarrow ^4\text{I}_{15/2}$ (520

nm -green) and $^4\text{S}_{3/2} \rightarrow ^4\text{I}_{15/2}$ (540 nm - green) transitions.[89] These red and green transitions belong to the 2-photon absorption process. According to the reference, it is expected that high concentration doping of Yb^{3+} could enhance the red emission peak, whereas a low concentration of Yb^{3+} will enhance the green emission peak due to the suppression of cross-relaxation process. On the other hand, the doping of Tm^{3+} ions can support $^1\text{D}_2 \rightarrow ^3\text{F}_4$ (450 nm - blue) and $^1\text{G}_4 \rightarrow ^3\text{H}_6$ (475 nm - blue) transitions.[90] However, the blue transition belongs to 3-photon absorption process so its UC efficiency is less than that of the red and green transitions through 2-photon absorption. Therefore, to obtain a high output of white-light emission at a high excitation power, the doping concentrations of both Yb^{3+} and Tm^{3+} are selected first to maximize blue emission intensity. Then, the doping concentration of Er^{3+} is selected subsequently to simultaneously modulate the relative intensities of RGB emission to control the final emission colors.

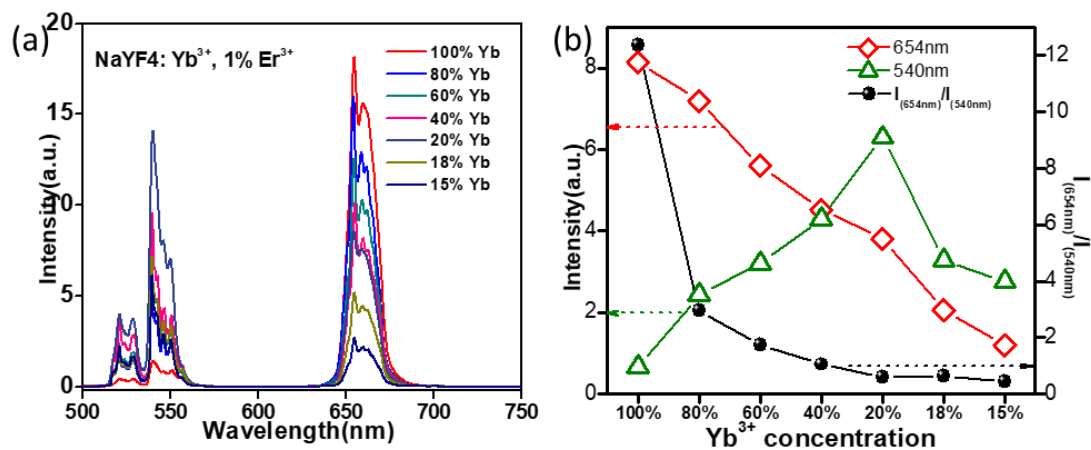


Figure 3.6 (a) The photoluminescence spectra and (b) the ratio of emission intensity between green and red emission changes of the $\text{Yb}^{3+}, \text{Er}^{3+}$ co-doped $\beta\text{-NaYF}_4$ hexagonal microrods under CW



980 nm laser excitation when the concentration of Yb^{3+} varies from 15% to 100%. The concentration of Er^{3+} ions is fixed at 1%.

In the photoluminescence experiment, the CW 980 nm laser beam was focused into a laser spot of 8- μm diameter through an objective lens so that high pump intensity of 1 MW/cm^2 can be obtained to excite the single $\beta\text{-NaYF}_4$ microrod. Figure 3.6a shows the photoluminescence spectra of $x\%$ Yb^{3+} , 1% Er^{3+} ($15 < x < 100$) doped single $\beta\text{-NaYF}_4$ hexagonal microrods under CW 980 nm excitation with source power density of 1 MW/cm^2 , and Figure 3.6b shows the corresponding ratio between the 645 nm (red) and 540 nm (green) emission intensities (i.e. $I_{654\text{nm}}/I_{540\text{nm}}$) in relation to the Yb^{3+} concentration. The emission band located at 654 nm is due to the ${}^4\text{F}_{9/2} \rightarrow {}^4\text{I}_{15/2}$ transitions of the Er^{3+} , while the green emissions located at 540 nm and 520 nm are due to the ${}^2\text{H}_{11/2} \rightarrow {}^4\text{I}_{15/2}$ and ${}^4\text{S}_{3/2} \rightarrow {}^4\text{I}_{15/2}$ transitions, respectively. It can be observed that when the concentration of Yb^{3+} is 100%, the red emission is dominant, because the high concentration of Yb^{3+} promotes the cross-relaxation process (i.e. ${}^4\text{F}_{7/2} \rightarrow {}^4\text{F}_{9/2}$ and ${}^4\text{I}_{11/2} \rightarrow {}^4\text{F}_{9/2}$ transitions between the two nearby Er^{3+} ions).[\[91\]](#) When decreasing the concentration of Yb^{3+} , the red emission intensity decreases, but the green emission increases initially and is maximized at a concentration of Yb^{3+} equals to 20%, followed by an intensity reduction because of the concentration quenching phenomenon. Therefore, by decreasing the concentration of Yb^{3+} , the emission colors can be modulated from red to green flexibly.

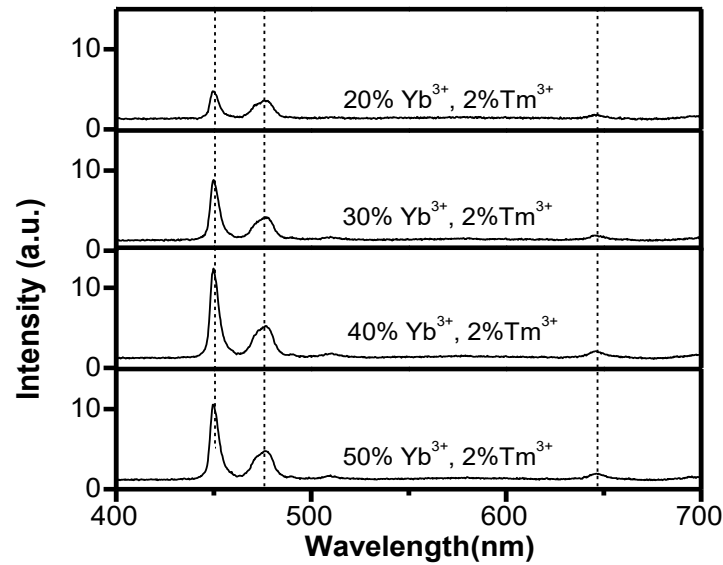


Figure 3.7 Photoluminescence spectra of the Yb^{3+} , Tm^{3+} co-doped $\beta\text{-NaYF}_4$ hexagonal microrods under the CW 980 nm laser excitation by modulating the concentration of Yb^{3+} . The concentration of Yb^{3+} is changed from 50% to 20%, and the concentration of Tm^{3+} is fixed at 2%.

Figure 3.7 shows the $y\% \text{Yb}^{3+}$, $2\% \text{Tm}^{3+}$ ($20 < y < 50$) co-doped $\beta\text{-NaYF}_4$ hexagonal microrods under the CW 980 nm pump with a power of 1 MW/cm^2 in order to optimize the blue emission intensity. According to the spectra, there are two blue peaks located at 450 and 475 nm. The 450 and 475 nm emission peaks correspond to the $^1\text{D}_2 \rightarrow ^3\text{F}_4$, and $^1\text{G}_4 \rightarrow ^3\text{H}_6$ transitions of Tm^{3+} respectively. The emission wavelength located at 647 nm (due to $^1\text{G}_4 \rightarrow ^3\text{F}_4$ transition of Tm^{3+}) is very weak and is negligible due to the concentration quenching effect of the fluorescence. The emission located at 450 nm is optimized when the concentration of Yb^{3+} is 40%.

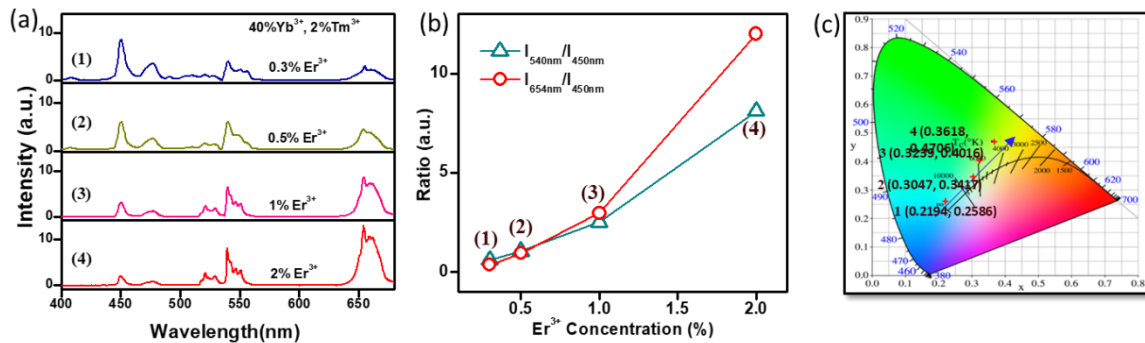


Figure 3.8 (a) Photoluminescence spectra and (b) the ratio of emission intensity between green and blue emission as well as red and blue changes of the Yb^{3+} , Tm^{3+} , Er^{3+} tri-doped $\beta\text{-NaYF}_4$ hexagonal microrods under CW 980 nm excitation by modulating the concentration of Er^{3+} . (c) CIE chromaticity image of the tri-doped $\beta\text{-NaYF}_4$ hexagonal microrods.

As mentioned before, because the blue emission is triggered by 3-photon absorption UC process, the UC efficiency is relatively lower when compared with that of the red and green emission (due to 2-photon UC). Therefore, in order to obtain the relatively high UC efficiency, we need to first optimize the blue emission in the Tm^{3+} , Yb^{3+} co-doped microrod, followed by the doping of Er^{3+} to modulate the relative intensity of red, green and blue intensities for white emission with high efficiency. In Figure 3.7, the blue emission is optimized when the concentration of Yb^{3+} is 40%, so we kept the concentration of Yb^{3+} and Tm^{3+} to be 40% and 2% respectively. Then, the concentration of Er^{3+} is used to control the relative emission intensity between the red, green and blue peaks in order to deduce a relatively high-efficiency white-light emission. Figure 3.8(a) shows the 40% Yb^{3+} , 2% Tm^{3+} , $z\%$ Er^{3+} ($0.3 < z < 2$) tri-doped $\beta\text{-NaYF}_4$ hexagonal



microrods under CW 980 nm excitation with pumped power of 1 MW/cm², and Figure 3.8b shows the corresponding ratio of emission intensity between green and blue light as well as red and blue lights. Figure 3.8c also shows the CIE chromaticity by increasing the concentration of Er³⁺. All of the above experiments are carried out at room temperature. White-light emission can be obtained from Yb³⁺, Tm³⁺, Er³⁺ tri-doped β-NaYF₄ hexagonal microrods under CW 980 nm excitation at 1 MW/cm². In addition, the corresponding 1931 CIE chromaticity coordinates by changing the concentration of Er³⁺ are given in Figure 3.8c. At low Er³⁺ concentrations, the blue emission has relatively high intensity. However, by increasing the concentration of Er³⁺, green and red emissions are increased and become dominant. When the concentration of Er³⁺ is equal to 0.5%, white-light emission with chromaticity coordinate of ($x = 0.3047$, $y = 0.3417$) can be obtained and the emission intensity in the single particle is optimized. This coordinate falls exactly within the white region of the 1931 CIE diagram and is very close to the standard equal energy white-light emission ($x = 0.33$ and $y = 0.33$). Hence, the concentration of Yb³⁺, Tm³⁺, and Er³⁺ are selected to be 40%, 2%, and 0.5% respectively to obtain the relatively high-efficiency white-light emission from the single β-NaYF₄ hexagonal microrods.

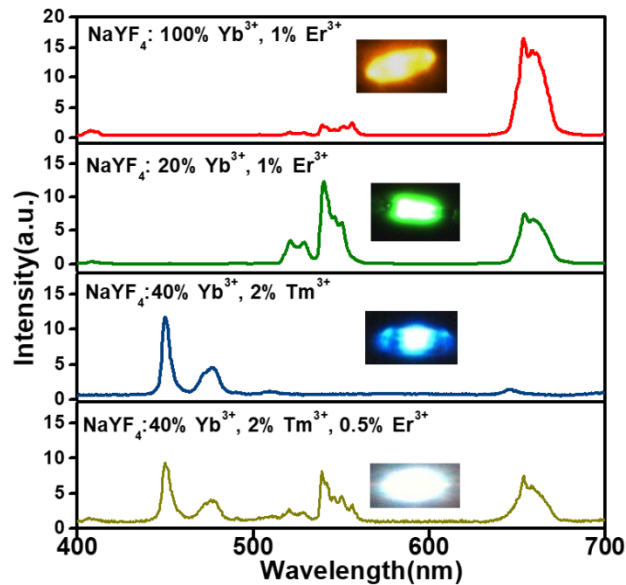


Figure 3.9 Photoluminescence spectra of the doped $\beta\text{-NaYF}_4$ hexagonal microrods under CW 980 nm excitation at a pumped power of 1 MW/cm^2 . The inset photos show the corresponding emission profile.

Figure 3.9 shows the photoluminescence spectra of the selected red, green, blue and white doped $\beta\text{-NaYF}_4$ hexagonal microrods with the optimized doping concentrations, as well as their corresponding pictures taken by the experimental setup camera. In this measurements, RGB emission intensities are maximized via the co-doping concentrations of 100% Yb^{3+} -1% Er^{3+} , 20% Yb^{3+} -1% Er^{3+} , and 40% Yb^{3+} -2% Tm^{3+} , respectively. Furthermore, 40% Yb^{3+} -2% Tm^{3+} -0.5% Er^{3+} tri-doped $\beta\text{-NaYF}_4$ hexagonal microrods are found to achieve effective white-light emission. As shown in Figure 3.9, the relative intensities of the RGB emission peaks are just slightly reduced from their maximum values so that the UC efficiency of the white-light emission is optimal.

3.5 RGB and white-light lasing emissions from the Ln^{3+} -doped β - NaYF_4 hexagonal microrods

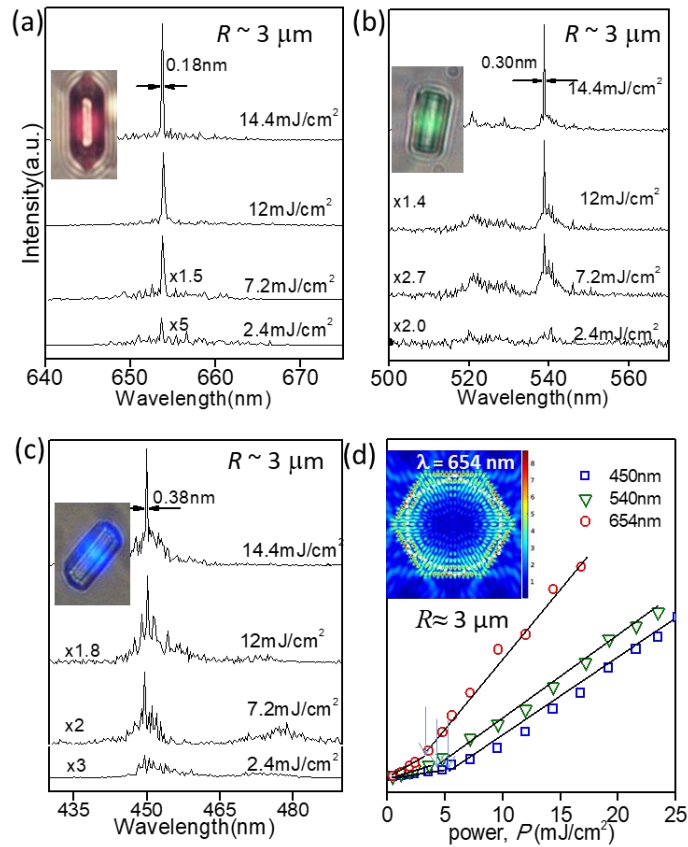


Figure 3.10 Lasing emission spectra of three individual β - NaYF_4 hexagonal microrods with different doping concentrations under 980 nm ns-pulsed laser excitation. The insets show the corresponding optical images with emission wavelengths of 654, 540 and 450 nm captured by the optical camera. (d) The corresponding intensity vs pump density curves. Numerical simulation of optical field distribution inside a 100% Yb^{3+} , 1% Er^{3+} co-doped β - NaYF_4 hexagonal microrods



emitted at 654 nm is shown in the inset of Figure d. The yellow dashed-line indicates the formation of one round-trip.

Figure 3.10 shows the RGB blue lasing spectra of (a) 100% Yb^{3+} , 1% Er^{3+} , (b) 20% Yb^{3+} , 1% Er^{3+} , and (c) 40% Yb^{3+} , 2% Tm^{3+} doping $\beta\text{-NaYF}_4$ single microrods of radius $\sim 3 \mu\text{m}$, under the excitation by 980 nm ns-pulsed laser. The inset of Figure 3.10a-c show the corresponding pictures captured by the camera from the optical microscope. As seen from the emission spectra in Figure 3.10a, when the excitation is low (2.4 mJ/cm^2), the spectra show broadband with the center located at 654 nm and this band corresponds to spontaneous emission. By increasing the excitation power density, the spectral line is narrowed, and UC lasing emission is achieved with a linewidth less than 0.4 nm when the excitation power is 7.2 mJ/cm^2 . This means that the UC red lasing emission with a single mode can be obtained in the single $\beta\text{-NaYF}_4$ hexagonal microrod. Figure 3.10b-c also show similar behavior of the microrods with green and blue lasing emissions, compared to that of in Figure 3.10a, in which the broad emission peak transforms into a narrowed lasing peak of linewidth below 0.4 nm when the power density is increased beyond the lasing threshold. The UC intensity vs pump density curves of these RGB emission spectra are also plotted in Figure 3.10d in order to measure the threshold associated with the lasing emissions. In each of the curves, a kink exists, representing the pump threshold (P_{th}). It is found that P_{th} is 3.0, 3.78 and 4.8 mJ/cm^2 for 654 nm, 540 nm and 450 nm emission, respectively. This result shows that it is easier to obtain red lasing emission compared with blue and green lasing emissions. It is believed that the $\beta\text{-NaYF}_4$ hexagonal microrods support lasing emission through the optical feedback supported by the six



flat surfaces. The inset of Figure 3.10d shows the numerical simulation of optical field profile (cross-section) of the 100% Yb^{3+} , 1% Er^{3+} co-doped $\beta\text{-NaYF}_4$ hexagonal microrods with the UC emission located at 654 nm. The six flat surfaces of the microrods support WGMs via total internal reflection (see the white dashed line). However, due to their relatively high cavity losses and a high threshold, Fabry-Perot (FP) modes or quasi-WGMs are not supported inside microrods. Furthermore, with lower lasing output power, the linewidth of the blue lasing emission is generally larger than that of the green lasing, followed by the red lasing line width. It was shown that the linewidth of a single-mode semiconductor laser is inversely proportional to its output power.

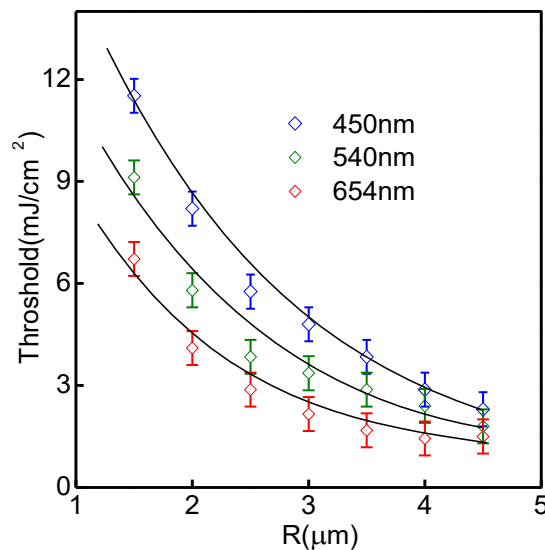


Figure 3.11 Plots of the threshold, P_{th} , versus radius, R , of the Ln^{3+} doped $\beta\text{-NaYF}_4$ hexagonal microrods at the RGB emissions.

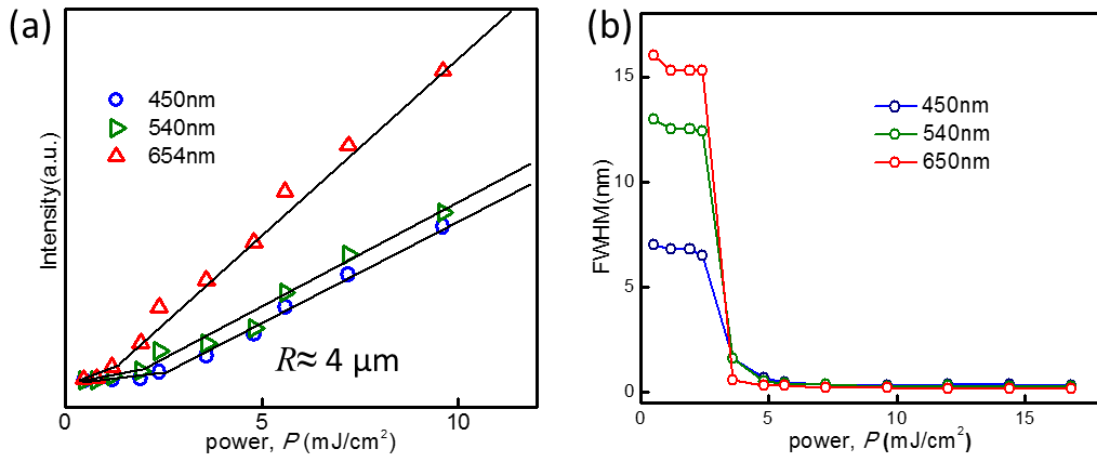


Figure 3.12 (a) UC intensity as a function of pump density and (b) lasing line width of the RGB emissions for a 40% Yb^{3+} , 2% Tm^{3+} , and 0.5% Er^{3+} tri-doping hexagonal microrod with radius is 4 μm .

In order to achieve UC white-light lasing emission, we used 40% Yb^{3+} -2% Tm^{3+} -0.5% Er^{3+} tri-doped β - NaYF_4 hexagonal microrods to measure the RGB lasing spectra. To obtain the RGB lasing emissions within the same cavity, we need to measure the threshold of the lasing emission initially by changing the cavity's radius. This is to make sure that lasing of the three base colors can be achieved under the same excitation density. Figure 3.11 shows the lasing threshold of the red, green and blue lasing for 40% Yb^{3+} , 2% Tm^{3+} , 0.5% Er^{3+} tri-doped β - NaYF_4 hexagonal microrods when the cavity radius is changed from 0.5 to 4.5 μm . Under 980 nm ns-pulsed excitation, it was observed that the threshold of red lasing is lower compared to that of the green and blue ones, which means that red lasing is easier to be obtained. This phenomenon is similar to

that presented in Figure 3.10. Besides, by increasing the radius, the threshold of the three emission wavelengths decreases. Therefore, a larger cavity makes it easier to obtain UC lasing emission. Here, we selected the microrods with radius $4\ \mu\text{m}$ because this value of radius enabled us to maintain stable single-mode lasing in our lasing measurement.

Figure 3.12a plots the UC intensity vs pump density curves of the 40% Yb^{3+} , 2% Tm^{3+} , 0.5% Er^{3+} tri-doped $\beta\text{-NaYF}_4$ hexagonal microrods (radius $R = 4\ \mu\text{m}$) for the RGB lasing emissions. Figure 3.12b plots the red, green and blue emission linewidth versus pump power density. From the results, a kink from the UC intensity vs pump density curves is observed, which demonstrates narrowing of emission spectra simultaneously from the RGB lasing modes.

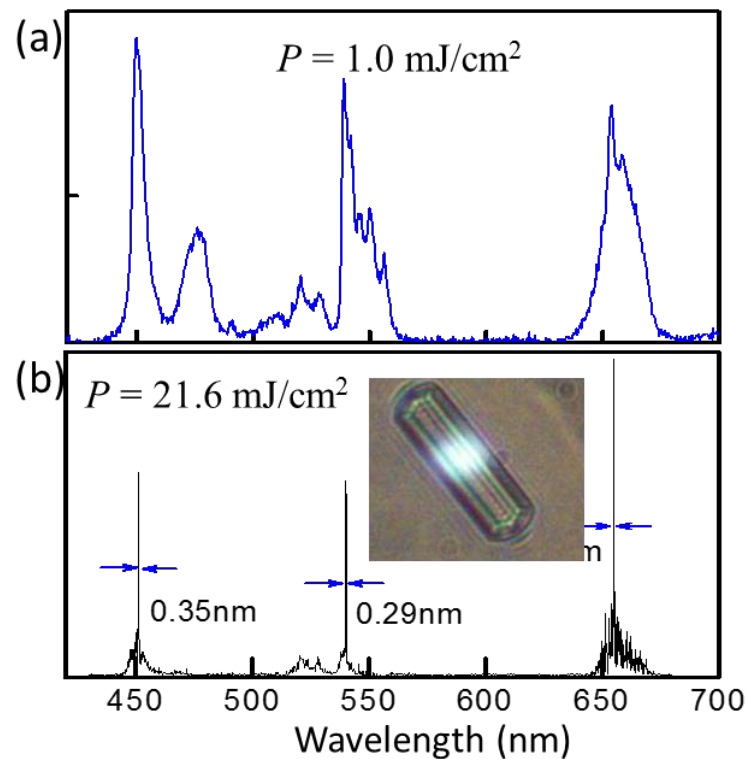


Figure 3.13 Emission spectra of the a 40% Yb^{3+} , 2% Tm^{3+} , and 0.5% Er^{3+} tri-doped hexagonal microrod under 980 nm ns-pulsed excitation, the pump density is (a) 1 and (b) 21.6 mJ/cm^2 . The inset in Figure 3.13(b) shows the corresponding single particles picture capture from the optical microscopy under 980 nm ns-pulsed excitation at room temperature.

Under 980 nm ns-pulsed laser excitation, Figure 3.13 shows the emission spectra of the tri-doped $\beta\text{-NaYF}_4$ microrods under the pump power density of 1.0 and 21.6 mJ/cm^2 . It is observed that when the excitation pump density is 21.6 mJ/cm^2 , the sample sustains single-mode lasing emission with the emission wavelength is located at 654, 540 and 450 nm. According to the inset of Figure 3.13, it can be observed that the white-light lasing is achieved under the pulsed laser excitation from the flat surface of the hexagonal microrod.

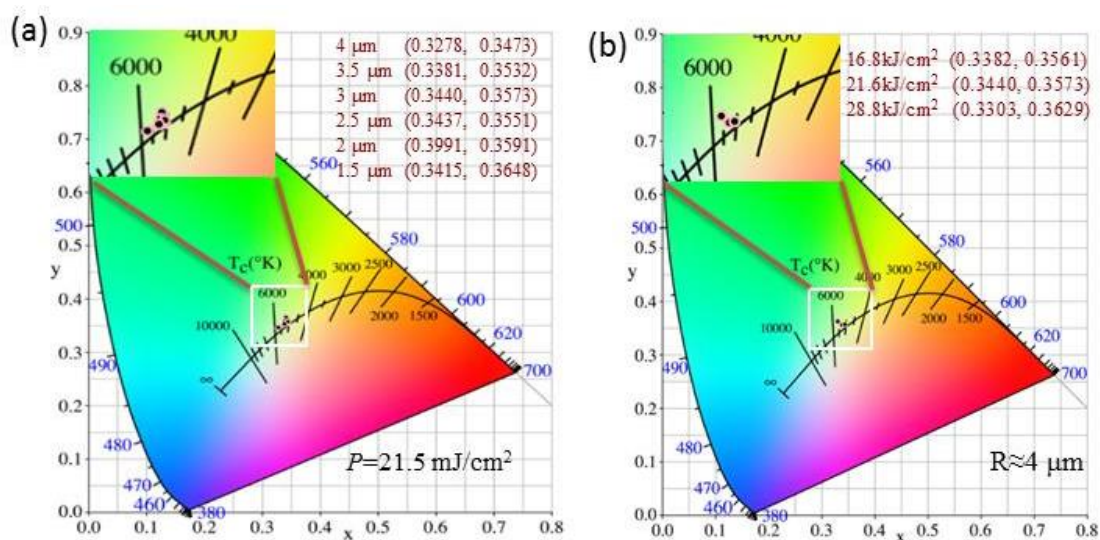


Figure 3.14 The plot of CIE1931 color coordinates of the doped microrods under lasing emission with different (a) radius R with pumped power kept at 21.5 mJ/cm^2 and (b) pumped power with radius R kept at 4 μm .



The corresponding CIE 1931 color diagram coordinate is calculated to determine the lasing color. Figure 3.14a shows the CIE of the lasing emission from the 40% Yb³⁺, 2% Tm³⁺, 0.5% Er³⁺ tri-doped β -NaYF₄ by fixing the excitation power at 21.5 mJ/cm² with a radius R varying from 1.5 to 4 μ m. These values are very close to the white point of CIE standard illuminant (with coordinates $x = 0.33$ and $y = 0.33$). Figure 3.14b shows the CIE of the lasing emission from a 40% Yb³⁺, 2% Tm³⁺, 0.5% Er³⁺ tri-doped β -NaYF₄ ($R = 4 \mu$ m) at different pump powers. In this case, the CIE is also located in the white area with little change over the ranges of operating conditions.

3.6 Summary

The optimal concentrations of the Ln³⁺ ions in β -NaYF₄ hexagonal microrods are obtained to support UC white-light lasing emission. The UC efficiency of the tri-doped β -NaYF₄ hexagonal microrods is measured using an integrating sphere. It is found that the quantum efficiency for the white-light emission via NIR laser excitation at room temperature is close to 0.01%, which is as good as our recent reported Ln³⁺-doped β -NaYF₄ core-shell nanoparticles. In the experiment, we find the optimal concentrations of 40% of Yb³⁺ and 2% of Tm³⁺ to ensure that blue emission at 450 nm is optimized. Then, we further change the doping concentration of Er³⁺ to modulate the relative intensity of RGB emissions and obtain the white-light emission from the same single microparticle. It is found that 0.5% of Er³⁺ is sufficient to excite RGB emission peaks simultaneously with similar emission intensities, and white-light emission can be generated according to the CIE calculation.



We demonstrate that the β - NaYF_4 hexagonal microrods support WGMs lasing at 654, 540 and 450 nm simultaneously with linewidths less than 0.4 nm. It is noted that the red lasing emission is easier to be obtained than the other two colors. On the other hand, the corresponding lasing threshold can be reduced by increasing the radius of the microrods. Therefore, to make sure that those RGB lasing emissions can emit simultaneously from the same cavity, we choose the microrods with radius, $R = 4 \mu\text{m}$. Under 980 nm ns-pulsed excitation, the lasing spectra of the micro-rods corresponds to the CIE 1931 color diagram coordinate ($x = 0.3440$, $y = 0.3573$). These values are very close to that of the white point of CIE standard illuminant with coordinates ($x = 0.33$ and $y = 0.33$).



4. Influence of plasmonic effect on the UC emission of Ln^{3+} -doped $\beta\text{-NaYF}_4$ hexagonal microrods

4.1 Introduction

In chapter 3, we investigated the multicolor lasing properties of the lanthanide (Ln^{3+})-doped $\beta\text{-NaYF}_4$ hexagonal microrods. Wide range of the color from blue to red lasing can be obtained based on the Ln^{3+} -doped materials, which means that color-tunable laser can also be realized by doping Ln^{3+} ions. However, their upconversion (UC) efficiency of the lasers are low (below 0.1%) and their low UC efficiency leads to the high excitation threshold of the lasing emission. Therefore, we are motivated to search for new methods to reduce the threshold of the Ln^{3+} -doped microcavity lasers. Hence, the low threshold UC lasers can find further applications in biomedical imaging, all-optical on-chip information processing, and optogenetics.

Here, we propose to employ the plasmonic effect to enhance the UC efficiency of the Ln^{3+} -doped $\beta\text{-NaYF}_4$ hexagonal microrods.[\[92-95\]](#) This is possible because recent investigations had reported that the Ln^{3+} -doped nanoparticles show intense improvement of UC emission intensity by up to 30 times through the use of surface plasmon resonance (SPR) when the resonance wavelength matched with the UC nanoparticles emission wavelength.[\[96-98\]](#) The improvement is the result of effective coupling between the excited fluorophores of the UC nanoparticles and the SPR of the metal nanoparticles. In addition, a similar phenomenon is observed in a long metal stripe embedded in Er^{3+} doped phosphate glass, which supported stimulated emission of surface



plasmon polaritons.[99] These findings motivate us to use the SPR in reducing the threshold of the UC lasing emission in our Ln³⁺ -doped β -NaYF₄ microcavity lasers.[100]

In this chapter, we have shown unambiguously that the excitation threshold of red/green/blue (RGB) lasing emissions from Yb³⁺-Er³⁺-Tm³⁺ tri-doped β -NaYF₄ hexagonal microrods can be decreased via SPR by placing the tri-doped β -NaYF₄ hexagonal microrods on an Ag-coated substrate. Hence, we observe: 1) SPR modes supported by the use of an Ag-coated substrate under high-power excitation. 2) Low absorption loss from the Ag coating through the use of micro-sized hexagonal rods. 3) The decrease of the lasing threshold by half through the interaction between the whispering gallery modes (WGMs) from the hexagonal cavities and SPR modes from the Ag layer. We also have shown that these improvements are due to the change in the lasing pathway in the lasing cavities by the plasmonic effect.

4.2 Design and fabrication of hexagonal microrods on Ag thin film

4.2.1 Simulation methods and results

2-D finite element method (COMSOL Multiphysics 5.0) was used to calculate the WGMs of the laser microcavities. The β -NaYF₄ hexagonal microrods with radius 2 μ m were considered in the design. Ag layer coated substrate also introduced in the calculation to study the influence of plasmonic effects. Thin layers of MgF₂ and Ag were deposited onto the quartz plate to form the substrate. In the calculation, it is assumed that the microrods and the substrate are surrounded by air. By using the eigenfrequency methods, WGMs were solved in the form of complex eigenfrequency, $f (= f_r + if_i)$ and the mode quality factor is defined as $Q = f_r/(2f_i)$. The refractive

index of $\beta\text{-NaYF}_4$ was set to 1.623 for all wavelength. The refractive indices are given in Table 4.1

Table 4.1 The refractive indices of MgF_2 , Ag, SiO_2 at different wavelengths

	450 nm	540 nm	654 nm
MgF_2	1.3815	1.3787	1.3767
Ag	$0.04 - 2.6484i$	$0.056895 - 3.5047i$	$0.051288 - 4.4404i$
SiO_2	1.4656	1.4603	1.4564

4.2.2 Optical measurement setup

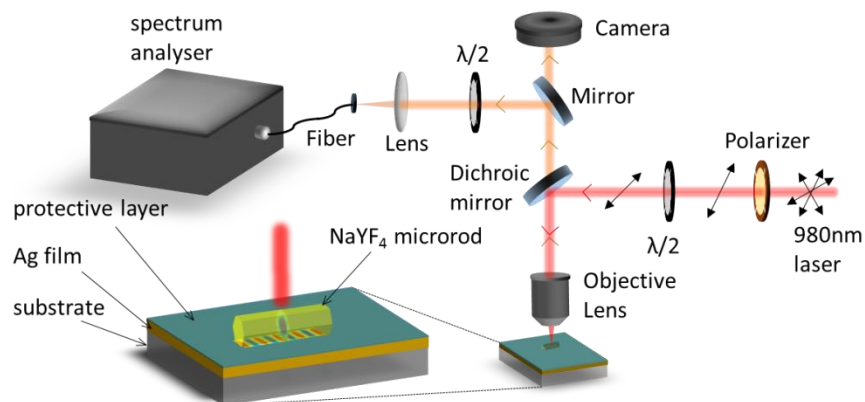


Figure 4.1 The optical measurement setup

Figure 4.1 shows the spectral measurement setup which is a modification from that given in Chapter 3. In this setup, the polarization of the 980 nm excitation laser is controlled by using $\lambda/2$



waveplate and polarizer (i.e. on the right-hand side of the objective lens). Lasing characteristics of the β -NaYF₄ were studied by using a frequency-tripled 355 nm Q-switched Nd: YAG pulsed laser (6 ns, 10 Hz) with a beam diameter of 0.8 cm as the main excitation source. 980 nm laser beams, which were polarized horizontally, were generated by an optical parametric oscillator. The sample was placed on an X-Y-Z translation stage of a light-field optical microscope (Leica DM1000 LED) for the optical (photoluminescence and lasing spectra) characterizations. A 50 \times 0.75 N.A. objective lens was used to excite and to collect light emission from the sample. The recorded light was then analyzed by an Oriel MS257 monochromator (spectral resolution is 0.1 nm) attached to a photomultiplier tube. The measurement was carried out at room temperature in an atmospheric ambiance. For photoluminescence measurement, we used continuous wave (CW) laser 980 nm as the excitation source.

4.3 Photoluminescence characteristics of the Ln³⁺ -doped β -NaYF₄ hexagonal microrods deposited on Ag substrate

4.3.1 Influence of the Ag thin film

To introduce the plasmonic effect, we used Yb³⁺-Er³⁺-Tm³⁺ tri-doped β -NaYF₄ hexagonal microrods on a SiO₂ substrate coated with Ag layer of 50 nm thickness (this value of Ag has optimized for the surface smoothness). Figure 4.2 shows the schematic diagram of the optical resonator. In the diagram, an MgF₂ film of thickness h is inserted between the β -NaYF₄ hexagonal microrods (with radius $r = 2 \mu\text{m}$) and the Ag layer. To study the dependence of the photoluminescence intensity due to the plasmonic effect on h , Figure 4.3 plots the computer

simulation results (i.e. using finite element method) of the Q-factor versus the thickness h of the proposed optical resonator at three primary colors (i.e. at wavelengths of 450 nm, 540 nm and 654 nm). The simulation results show that the MgF_2 layer is not necessary to introduce to the system to maximize the corresponding Q factor of the optical resonator. This is because the $\beta\text{-NaYF}_4$ rod is of micro-size so that the profile of the plasmon modes can extend toward the microrods and avoid penetrating into the Ag layer. Consequently, the MgF_2 layer does not contribute to the reduction of absorption loss arisen from the Ag layer.

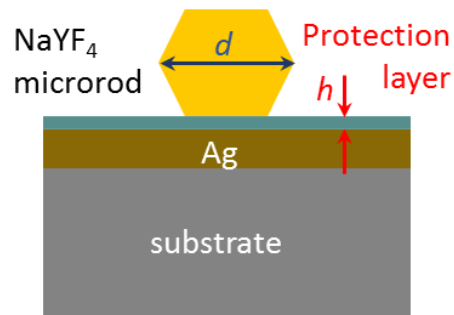


Figure 4.2 The schematic diagram of the optical resonator

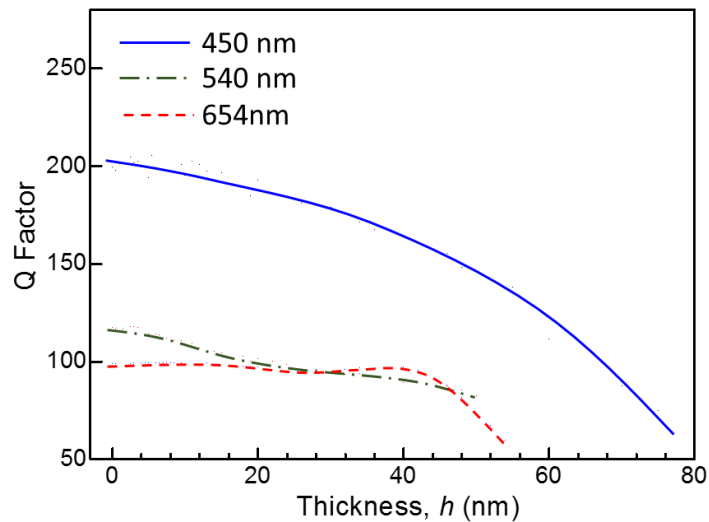


Figure 4.3 Plot of calculated Q-factor of a $\beta\text{-NaYF}_4$: Yb^{3+} , Er^{3+} , Tm^{3+} hexagonal microrod deposited on an Ag-coated (50 nm) substrate, which is also protected by MgF_2 dielectric layer with different thickness h .

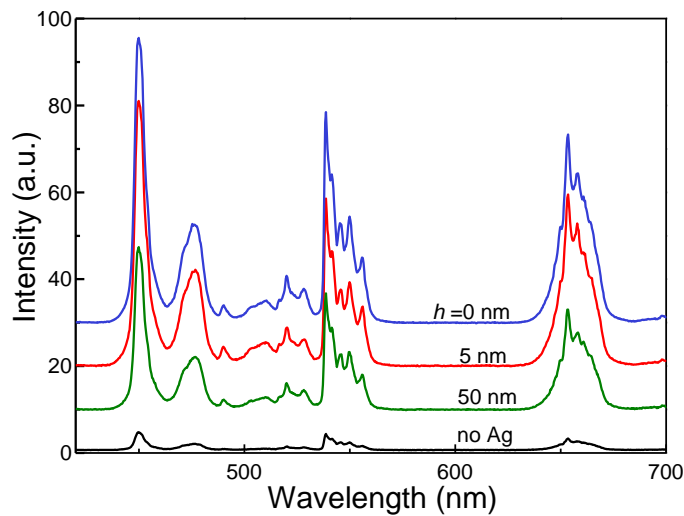


Figure 4.4 The measured photoluminescence UC spectra from a microrod deposited on an Ag-coated substrate with different thicknesses ($h = 0, 5, 50$ nm) of MgF_2 protection layer and without Ag.

Figure 4.4 plots the measured spontaneous emission spectra of a $\beta\text{-NaYF}_4$: Yb^{3+} , Er^{3+} , Tm^{3+} hexagonal microrod at different the MgF_2 thicknesses h . Under CW 980 nm laser excitation, the spectra show the blue UC emission peak at 450 nm can be increased by 16 times (the relative intensity increased from 3.95 to 65), the green emission peak at 540 nm can be increased by 13 times (the relative intensity increased from 3.6 to 48) and the red emission peak at 654 nm can be increased by 13 times (the relative intensity increased from 3.25 to 44), when there is no MgF_2



protection ($h = 0$ nm). The RGB emission intensities show more than 10 times of increase and such effect is the greatest for the blue emission. On the other hand, we find that by increasing the value of the MgF₂ thickness, the enhancement reduces with h and this results consistent with the simulation results given in Figure 4.3. It should be mentioned that the intensity enhancement is independent of the rare earth doping concentration and the type of the dopants (Figures 4.5). According to Figure 4.5, the UC spontaneous emission spectra of single β -NaYF₄: $x\%$ Yb³⁺, 1%Er³⁺ hexagonal microrods (i.e. x ranging from 20% to 60%) have enhancement of about 11 times for all the values of x . This means that the influence of the plasmonic effect is independent of the concentration of the rare earth dopant. In addition, the plasmonic effect with different sizes of the microrods is also studied. As shown in Figure 4.6. The influence of plasmonic effects can be amplified when the particles size is increased. We have measured the UC spontaneous emission spectra of Yb³⁺ and Tm³⁺ doped β -NaYF₄ hexagonal microrods with different radius. It is observed that the microrods with a larger radius have stronger enhancement under the influence of plasmonic effect (e.g. microrods with a radius of 3 and 2 μ m have an enhancement of emission intensity by 9.3 and 5.5 times, respectively). This is because a microrod with a large radius has a large surface area to interact with the Ag layer so that the plasmonic effect can be increased.

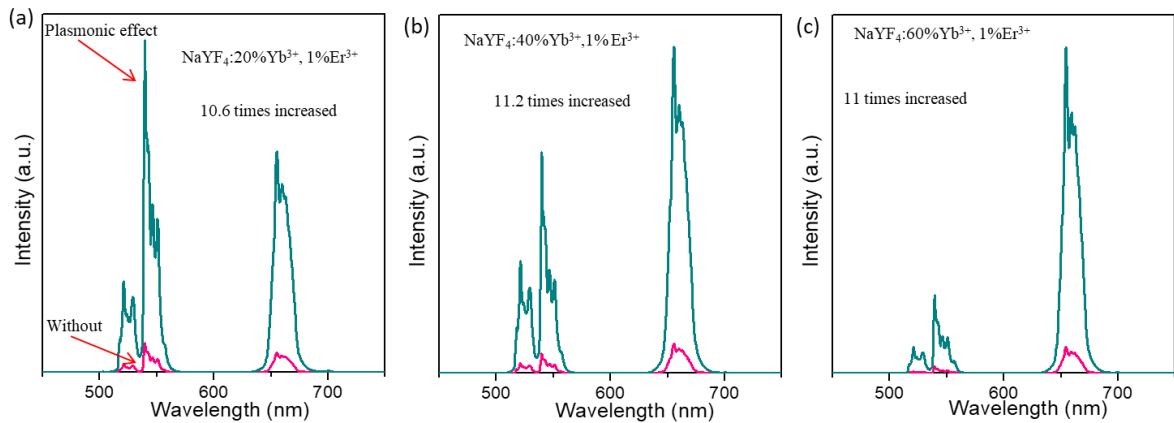


Figure 4.5 UC spontaneous emission spectra of a $\beta\text{-NaYF}_4: x\% \text{Yb}^{3+}, 1\% \text{Er}^{3+}$ hexagonal microrods (with $r \sim 4 \mu\text{m}$) for x equal to (a) 20%, (b) 40% and (c) 60%.

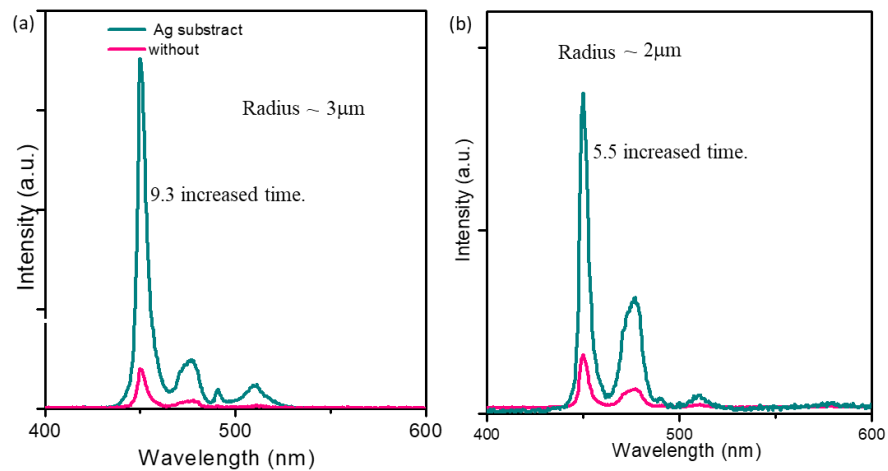


Figure 4.6 UC spontaneous emission spectra of a doped $\beta\text{-NaYF}_4: \text{Yb}^{3+}, \text{Tm}^{3+}$ hexagonal microrods with a radius equal to (a) 3 and (b) 2 μm .

4.3.2 Polarization characteristics of the excitation and emission lights

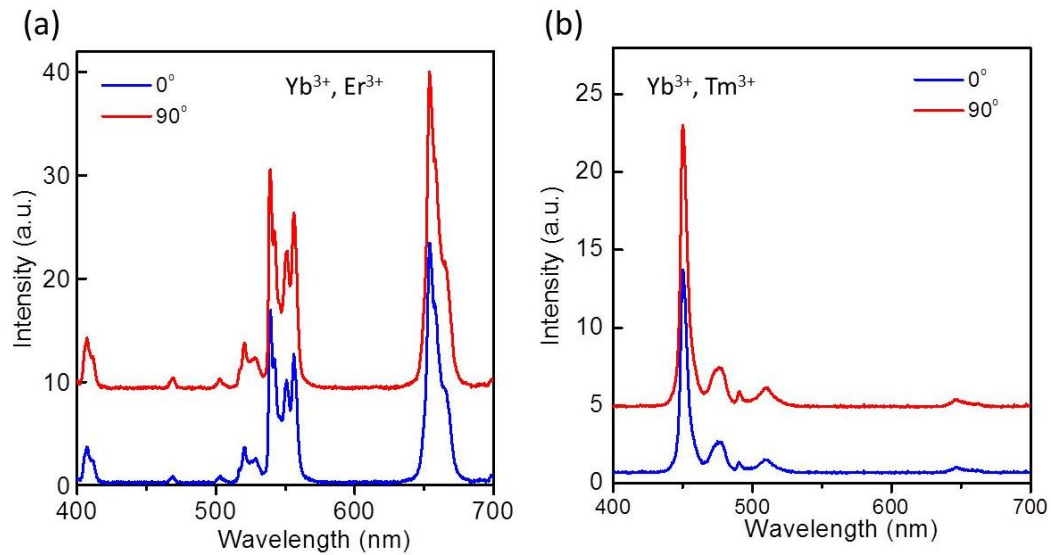


Figure 4.7 UC spontaneous emission characteristics of (a) β -NaYF₄: Yb³⁺, Er³⁺ hexagonal microrods and (b) β -NaYF₄: Yb³⁺, Tm³⁺ hexagonal microrods (with $r \sim 4 \mu\text{m}$) under the influence of excitation polarizations (i.e. $\Theta_{in} = 90^\circ$ and 0°).

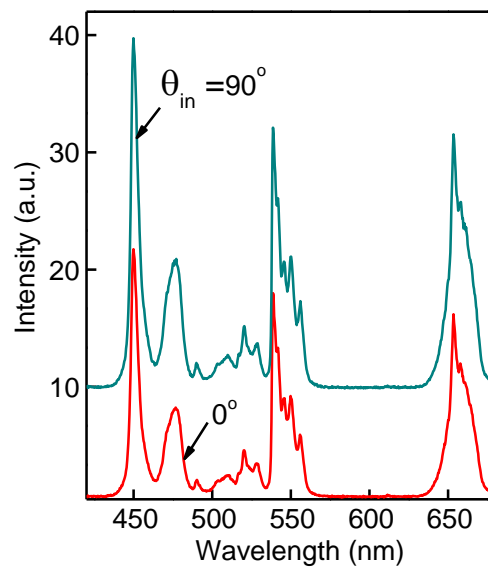




Figure 4.8 Plot of emission spectra of a β -NaYF₄: Yb³⁺, Er³⁺, Tm³⁺ hexagonal microrods at different output polarization, Θ_{out} . The microrod is deposited on an Ag-coated substrate and under CW 980 nm laser excitation with two orthogonal orientations ($\Theta_{in} = 90^\circ$ perpendicular and $\Theta_{in} = 0^\circ$ is parallel to the length of the microrod).

Figure 4.7 and 4.8 plot the emission spectra from a β -NaYF₄:Yb³⁺, Er³⁺/Tm³⁺ and β -NaYF₄: Yb³⁺, Er³⁺, Tm³⁺ hexagonal microrods (radius $r \sim 2 \mu\text{m}$) respectively. The microrods are deposited on an Ag-coated (50 nm) substrate and under the excitation of CW 980 nm laser with two orthogonal polarizations, Θ_{in} (i.e. $\Theta_{in} = 90^\circ$ represents the polarization of the 980 nm laser is in a direction perpendicular to the length of the microrod). According to the emission spectra, the emission intensity can be increased by 30% when Θ_{in} changes from 0° to 90° (for both Figure 4.7 and Figure 4.8).

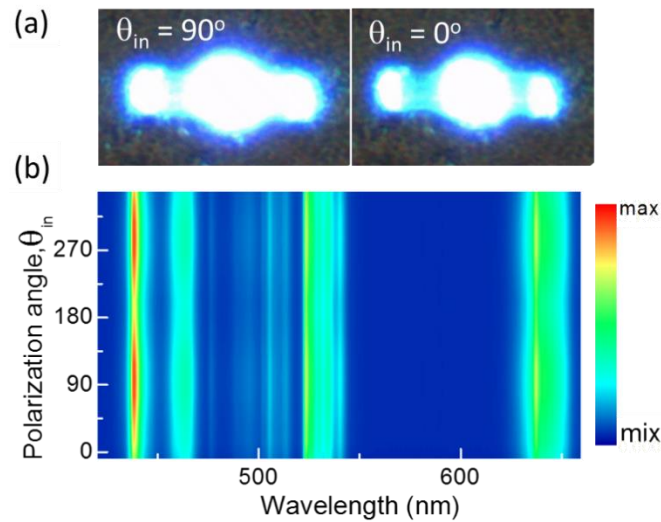




Figure 4.9 (a) Photos of microrod under CW 980 nm laser excitation with two orthogonal orientations. (b) A two-dimensional plot of emission intensity versus Θ_{in} and emission wavelength intensity.

In order to measure the effect of polarization angle Θ on the emission intensity of the microrod, we varied Θ and measure the corresponding photoluminescence spectra. Figure 4.9a shows the near-field profile of the microrods under the CW 980 nm laser excitation at the middle of the microrods for $\Theta_{\text{in}} = 0^\circ$ and 90° . It is observed that the emission intensity has been enhanced when the excitation degree is changed from 0° ($\Theta_{\text{in}} = 0^\circ$) to 90° ($\Theta_{\text{in}} = 90^\circ$). In addition, the emission light is propagated to the other edge of the microrod. This means that with the assistance of the plasmonic effect, the UC light can propagate along the length of the microrod. This claim is valid because the light propagation cannot be observed on the microrods deposited on the substrate without Ag coating. Therefore, our theoretical studies and experimental observations confirmed that the enhancement of spontaneous emission intensity in the $\beta\text{-NaYF}_4: \text{Yb}^{3+}, \text{Er}^{3+}, \text{Tm}^{3+}$ hexagonal microrods is due to the plasmonic effect with the existence of the Ag-coated substrates. Figure 4.10 shows the near-field profile of a $\beta\text{-NaYF}_4: \text{Yb}^{3+}, \text{Er}^{3+}, \text{Tm}^{3+}$ hexagonal microrod deposited on the substrate with/without Ag coating under the edge and center excitation. With the assistance of the plasmonic effect, the UC emission could propagate along the length of the microrod. However, when no plasmon effect is introduced, light propagation is not supported.

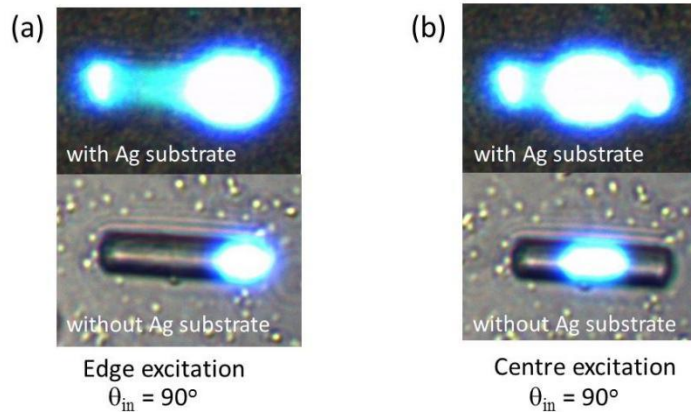


Figure 4.10 Near-field profile of a $\beta\text{-NaYF}_4\text{:Yb}^{3+}, \text{Er}^{3+}, \text{Tm}^{3+}$ hexagonal microrod (with $r \sim 4 \mu\text{m}$) deposited on the substrate with/without Ag coating under (a) edge and (b) center excitation.

4.4 The plasmonic effect on UC lasing emission characteristics of $\beta\text{-NaYF}_4$ hexagonal microrods

To study the plasmonic effect on the lasing emission from the single hexagonal microrod, we measured the lasing spectra of a microrod ($r = 2 \mu\text{m}$) deposited on a substrate with and without Ag-coating, see Figure 4.11. The excitation source is a 980 nm pulsed (6 ns) laser with polarization $\Theta_{\text{in}} = 90^\circ$. To measure the lasing threshold of the $\beta\text{-NaYF}_4$ hexagonal microrod, the UC emission intensity versus excitation power is measured. The intensity of the UC lasing emission as a function of pump density for three emission wavelengths measured at around 450, 540, and 654 nm are shown in Figure 4.11a. The kinks (i.e. lasing threshold) appear at the UC intensity vs pump density curves shows that the lasing threshold for the case with Ag-coated substrate is lower than that without Ag-coated substrate by $\sim 50\%$ (red, green, and blue threshold reduces from 2.0, 2.0 and

2.3 to 0.89, 1.16 and 1.16 mJ/cm^2 respectively). The lasing spectra for the two laser configurations under the excitation power of $3.5 \text{ mJ}/\text{cm}^2$ are given in Figure 4.11b. The results show that the spectral linewidth is less than 0.4 nm for both configurations. Therefore, this means that the bare microrod is able to sustain lasing emission, and the introduction of the plasmonic effect reduces the lasing threshold by 50%.

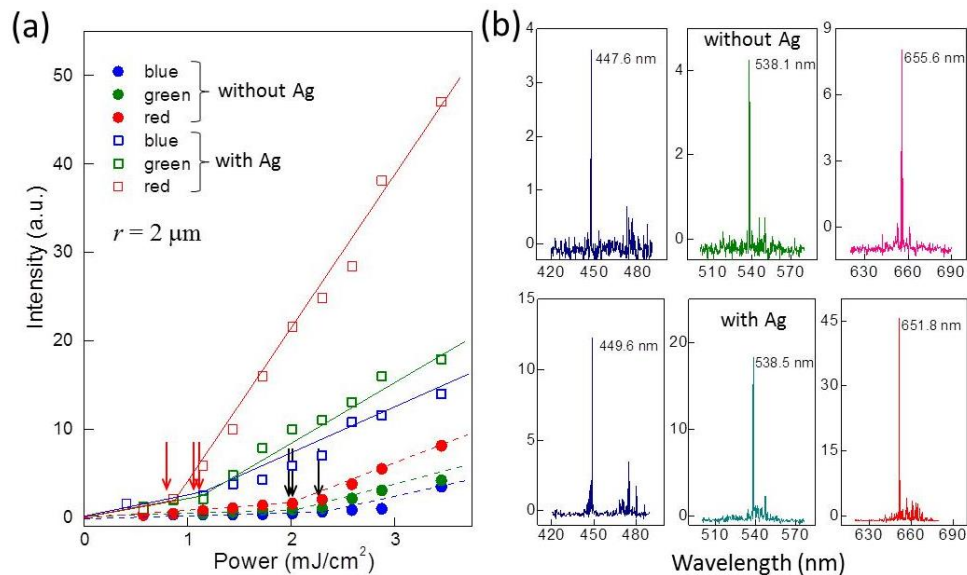


Figure 4.11 The intensity of the UC lasing emission as a function of pump density with and without deposited on the Ag-coated substrate for the three-color emission peaks (i.e. 450 nm, 540 nm and 654 nm). (b) The corresponding emission spectra of the hexagonal microrods with and without deposition on the Ag-coated substrate at the pumped power of $3.5 \text{ mJ}/\text{cm}^2$.

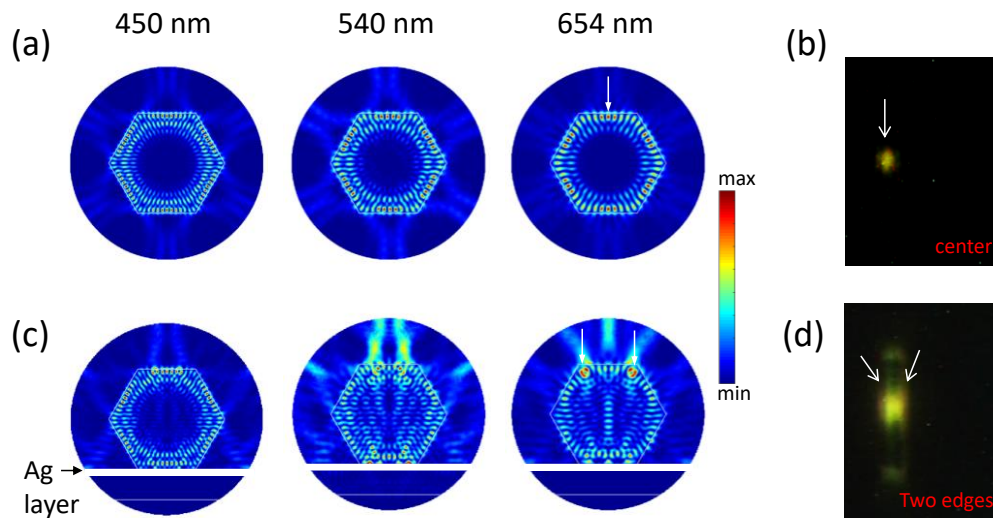


Figure 4.12 (a) Numerical simulation results of resonant modes inside a hexagonal microrod with different wavelengths (450, 540 and 654 nm). (b) Near-field photo of a hexagonal microrod under 980 nm excitation. (c) Numerical simulation results of resonant modes inside a hexagonal microrod deposited on an Ag-coated substrate with different wavelengths (450, 540 and 654nm). (d) Near-field photo of a hexagonal microrod deposited on an Ag-coated substrate under 980 nm excitation.

The previous investigation on the modal profile of hexagonal microrods under lasing action has suggested the support of WGMs. Resonant oscillation is obtained through total internal reflection at the center of the flat surface of the hexagonal structure, see Figure 4.12a. In fact, experimental measurement has shown the near-field image of the hexagonal microrods under lasing operation has an intense spot appearing at the center of the flat surface, see Figure 4.12b. To understand the influence of SPR on the modal characteristics of the hexagonal microrods under



lasing operation, we performed computer simulation on the modal characteristics of the hexagonal microrods with $r = 2 \mu\text{m}$ (diameter is $4 \mu\text{m}$) deposited on an Ag-coated substrate, see Figure 4.12c. The resonant wavelengths are selected to be around 450, 540 and 654 nm in the calculation. As we can see, only TM modes supported inside the microrods and it seems that optical feedback is established between the two flat surfaces parallel to the Ag layer (i.e. it is more obvious for the green and red modes, see the white arrows). The near-field on the flat surface opposite to the Ag-coated substrate shows the two edges of the flat surface having intense spots. Figure 4.12d displays the near-field profile of the microrods deposited on Ag-coated substrate under lasing operation. It is clearly observed that two spots appear at the edge of the flat surface. Hence, it is believed that the plasmonic mode on the interface between the microrod and Ag layer coupled to the original WGMs to form modified WGMs with lower cavity loss to support lasing emission.

4.5 Summary

The enhancement of light emission from the Yb^{3+} - Er^{3+} - Tm^{3+} tri-doped β - NaYF_4 hexagonal microrods via the influence of the SPR was studied. This can be achieved by placing the microrods on Ag-coated substrates. For the microrod excited below the lasing threshold, we observe the enhancement of the UC spontaneous emission through the presence of SPR by 10 times. For the microrods under lasing operation, we show that the presence of SPR reduced the lasing threshold by 50%. This is due to the coupling between the WGMs of the bare microrod and the SPR modes propagating on the surface of the Ag layer.



5. The effect of surface defects of Ln^{3+} -doped KLu_2F_7 UC nanoparticles on UC characteristics

5.1 Introduction

Because the large surface to volume ratio for the nanoparticles, there are a lot of lanthanides are doped at the nanoparticle surface. This means that the surface defects would deactivate the lanthanide and then decrease the UC emission process. Recently, core-shell upconversion (UC) nanoparticles have shown to have high photoluminescence efficiency and they are expected to be useful for the applications in optical imaging-guided bio-imaging, therapeutic, anti-counterfeiting and solar cells.[\[101-104\]](#) This is because the outer coating removes the influence of quenching effect due to the isolation of core from the surrounding passivation agents (e.g. ligand, solvent).[\[105\]](#) Therefore, surface-related deactivation can be effectively suppressed. In addition, the surface trapping of the doped ions, which results in the fluorescence quenching, can be significantly suppressed by the fabrication of the core-shell structure.[\[106\]](#) Recently the studies have shown that the preparation of the NaGdF_4 shell of NaGdF_4 : Yb/Tm core UC nanoparticles can improve the photoluminescence intensity by more than 450 times, which is an indirect proof of the removal of core's surface defects.[\[107\]](#) However, at present, there is still no direct observation demonstrate that the restoration of surface-related defects for the nanoparticles indeed contributes to the improvement of UC efficiency.



In this chapter, we use a the thermal annealing process to restore the lanthanide (Ln^{3+}) -doped KLu_2F_7 bare core UC nanoparticles from surface defects (*i.e.* disorder, vacancy, and interstitial defects) to study the mechanism of surface defects on the effect of UC photoluminescence. The use of UC KLu_2F_7 nanoparticles, which has a uniform thickness of less than 10 atomic layers, provides the possibility to obtain high-resolution (HR) transmission electron microscopy (TEM) image through the use of aberration-corrected high angle annular dark field (HAADF) scanning transmission electron microscopy (STEM). Surface defects can be restored by using the thermal annealing method and the corresponding photoluminescence intensity can be increased by an order of magnitude. This proves that the surface defects are related to the surface luminescence quenching centers of the UC nanoparticles. The dominant green lasing emission, which decay lifetime is three times shorter than that of the red lasing emission, is also observed under 980 nm ns-pulsed laser excitation. This result can suggest that the restoration of surface defects from $\text{KLu}_2\text{F}_7: 38\% \text{Yb}^{3+}, 2\% \text{Er}^{3+}$ UC nanoparticles can suppress non-radiative recombination at the short transient time. Hence, we verify unambiguously the restoration of surface defects can significantly enhance UC photoluminescence intensity.

5.2 Fabrication methods of KLu_2F_7 UC nanoparticles and microcavities

$\text{KLu}_2\text{F}_7: 38\% \text{Yb}^{3+}, 2\% \text{Er}^{3+}$ UC nanoparticles were fabricated by using the co-precipitation method. For the synthesis of RECl_3 ($\text{RE}=\text{Lu}, \text{Yb}, \text{Er}$) solution, high purity Yb_2O_3 (0.38 mmol, 99.99%, Aladdin), Lu_2O_3 (0.6 mmol, 99.99%, Aladdin) and Er_2O_3 (0.02 mmol, 99.99%, Aladdin)



were added to concentrated hydrochloric acid in a 100 mL beaker and then heated to 200 °C. The obtained RECl₃ in 1mL DI water was magnetically mixed with OA (Oleic Acid, 8 mL, 85%, Aladdin) and ODE (1-Octadecene, 12 mL, >90%, Aladdin) in a 100 mL three-neck round-bottom flask. The mixture was degassed under an N₂ flow and heated to 150°C for 1 h to form a clear solution and remove water in the flask, and then cooled to room temperature. A methanol solution (9 mL, 99.9%, Aladdin) containing NH₄F (3 mmol, 98%, Aladdin) and KOH (2 mmol, 95%, Aladdin) was added into the OA and ODE solution and heated to 50 °C for 30 min. After that, the solution was slowly heated to 110°C and kept for 30 min to remove methanol and the remaining water completely. Then the reaction mixture was quickly heated to 290 °C and aged for 1h. After the solution was left to cool down to room temperature, ethanol was added to precipitate the UC nanoparticles. The product was washed with cyclohexane and ethanol for three times, before the final KLu₂F₇:38% Yb³⁺, 2% Er³⁺ UC nanoparticles were re-dispersed in 5mL cyclohexane in preparation for their further use. In the washing process, the volume ratio of cyclohexane and ethanol for the first two times is set 4:10 and the final one is 10:4. Samples of KLu₂F₇ with different concentration (28%, 38%, 48%, 58%, 78%, and 98%) Yb³⁺ and 2% Er³⁺ can also be synthesized by a similar procedure except for different moles of Lu₂O₃ and Yb₂O₃ involved in the reaction.

The thermal annealing method of KLu₂F₇:Yb³⁺, Er³⁺ UC nanoparticles. 8 mL OA and 12 mL ODE were mixed in a three-neck round-bottom flask, and then 0.5 mmol as-prepared bare core UC nanoparticles were added into the solution under an N₂ flow without the addition of K, Lu and F ions. The mixed solution was heated to 80 °C to evaporate cyclohexane with stirring. After 30 min, the mixture was heated to the annealing temperature of 240 °C for 1.5 h, respectively. Finally,



the samples were cooled down to room temperature. The annealed UC nanoparticles were washed by a solution with a volume ratio of cyclohexane: ethanol equal to 4:10 eight times and subsequently washed by another solution with a volume ratio of cyclohexane: ethanol equal to 10:4. For the optical testing, the concentrations of the KLu₂F₇:38% Yb³⁺, 2% Er³⁺ UC nanoparticles was fixed to 0.03 mg/mL.

Synthesis of microcavities. Microcavities were fabricated by coating a small drop of UC nanoparticle and silica resin on bare optical fibers. Then, the coated fibers are suspended vertically to form an elliptical microcavity. By increasing the amount of mixture, we can control the diameter of the elliptical microcavity.

5.3 Physical and optical properties of KLu₂F₇ UC nanoparticles

5.3.1 TEM, HAADF-STEM characteristic measurement of KLu₂F₇ UC nanoparticles

HAADF-STEM images were measured by a JEOL JEM-ARM200F TEM/STEM with a spherical aberration corrector. The operation of HAADF HR-TEM imaging can be explained as follows. 1) Before measuring the HAADF HR-TEM, we need to make sure that the UC nanoparticles are cleaned. 2) When we record the HAADF HR-TEM images, we need to reduce the bombardment of the electron beam to the UC nanoparticles by choosing a super short dwell time (*i.e.* 3 μs, it should be mentioned that the typical dwell time is > 10 μs). Then, a minimum spot size (*i.e.* 1 in the 10 levels of electron beam spots of ARM200F) of the electron beam is



selected to minimize the damage to the UC nanoparticles. Finally, we further optimize the magnification of the microscope such that the atoms of the UC nanoparticles can still be clearly observed and simultaneously the damage of the UC nanoparticles is minimized. If the electron beam energy is too high, the surface damage of the UC nanoparticles cannot be avoided. Here, we found that 10 M is the best enlargement factor, which can help us to observe a clear image of atoms without damaging them. 3) Select a suitable geometry of the UC nanoparticles for the HAADF HR-TEM imaging is also important to capture a clear image on an atomic scale. We selected a UC nanoparticle with a uniform thickness so that this allows us to easily control the energy of the electron beam.

General Characterization. XRD was performed using a D8 Focus diffractometer (Bruker) with $\text{Cu-K}\alpha$ radiation ($\lambda=0.15405$ nm) in the 2θ range from 10° to 80° . The particle morphology and thickness were studied with field TEM and HR-TEM, carried out using U.S. FEI Tecnai G2 F20 operating at 200kV. The UC photoluminescence spectra of the samples under the excitation of 980 nm near-infrared (NIR) resource with different pulsed width were recorded by HITACHI-F-7000 spectrophotometer at a different temperature. The decay curves were measured on an Edinburgh instruments FLS980 spectrometer. The emission and excitation spectra of the sample were recorded on a HITACHI F-7000 fluorescence spectrophotometer using a static 150 W Xe lamp as the excitation source. For the laser measurement, a Continuum Panther EX optical parametric oscillator and a 355 nm frequency-tripled Continuum Powerlite DLS 9010 Q-switched Nd: YAG laser were used to generate 980 nm pump pulses of width and repetition rate of ≈ 6 ns and 10 Hz, respectively.



5.3.2 Physical properties of KLu_2F_7 UC nanoparticles

Figure 5.1 shows the diagram of fabrication methods of the $\text{KLu}_2\text{F}_7:38\% \text{Yb}^{3+}, 2\% \text{Er}^{3+}$ UC nanoparticles with a high Yb^{3+} concentration doping. In this fabrication process, the as-growth UC nanoparticles are cooled down and then washed for few times before measuring the thermal annealing to avoid Ostwald ripening. In addition, in order to make sure that, during the annealing process, UC nanoparticle core-shell structure cannot be formed, we need to wash the fabricated as-growth UC nanoparticles many times to make sure K, Lu, and F ions at surface are removed, and the annealing temperature is lower than the formation temperature of the shell structure. This annealing temperature is selected at 240°C to optimize the UC photoluminescent efficiency (Figure 5.2). And the XRD patterns of the glasses before and after the thermal annealing processes are measured as shown in Figure 5.3. After the thermal annealing process, the XRD pattern shows the good crystallinity compared with that of as-growth sample.

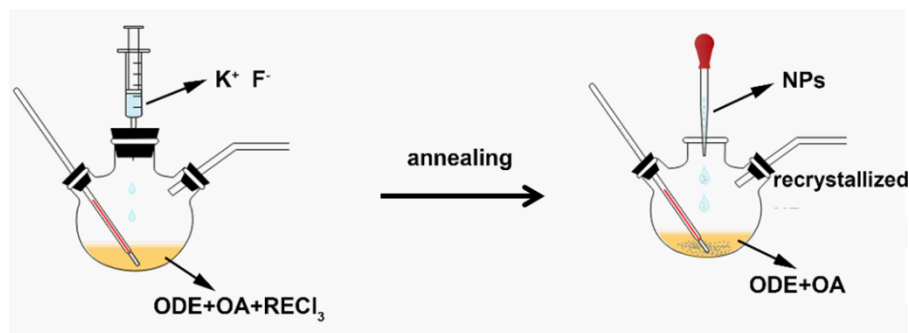


Figure 5.1 Schematic diagram of the thermal annealing process of $\text{KLu}_2\text{F}_7:38\% \text{Yb}^{3+}, 2\% \text{Er}^{3+}$ UC nanoparticles.

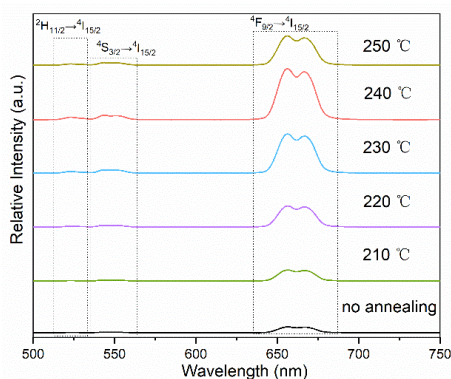


Figure 5.2 Photoluminescence spectra of the $\text{KLu}_2\text{F}_7:38\% \text{Yb}^{3+}, 2\% \text{Er}^{3+}$ UC nanoparticles *versus* different annealing temperature.

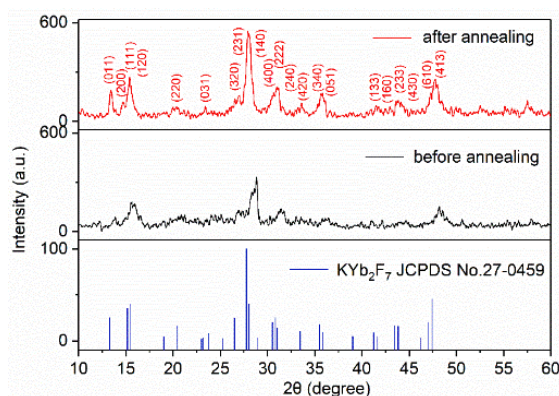


Figure 5.3 XRD patterns of $\text{KLu}_2\text{F}_7:38\% \text{Yb}^{3+}, 2\% \text{Er}^{3+}$ UC nanoparticles before and after the thermal annealing and the standard JCPDS card 27-0459.

In order to study the detail information of the structure of the KLu_2F_7 nanoparticles, the TEM images of $\text{Yb}^{3+}/\text{Er}^{3+}$ doped KLu_2F_7 UC nanoparticles were measured as shown in Figures 5.4a and 5.4(e). The HR-TEM images for KLu_2F_7 nanoparticles before and after the annealing process clearly show the lattice fringes at the interior of the UC nanoparticles, which are shown in Figures



5.4b and 5.4f respectively. In addition, lattice fringes and fast Fourier transform (FFT) reflections are observed, the d-spacing of which was attributed to the KLu_2F_7 UC nanoparticles structure. The lattice fringes show a plane spacing of 0.660 nm corresponding to the (011) plane, clearly indicating good internal crystallization KLu_2F_7 nanoparticles. For the as-growth KLu_2F_7 nanoparticles, an epitaxial amorphous phase is observed at the edge area, while the UC nanoparticles after the thermal annealing showed well-defined edge configuration. The KLu_2F_7 nanoparticles exhibit a monodisperse size distribution of about 30 nm without aggregation before and after the thermal annealing process, see Figures 5.4d and 5.4h. This means that the thermal annealing process does not increase the KLu_2F_7 UC nanoparticles size, but improve the crystallinity of KLu_2F_7 nanoparticles.

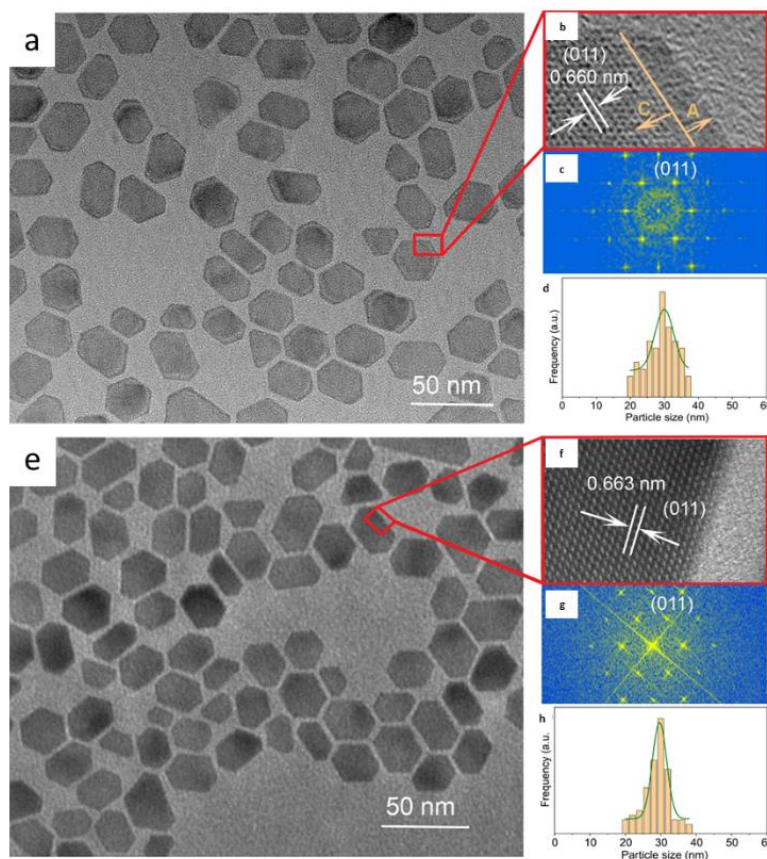


Figure 5.4 (a) TEM, (b) HR-TEM image, (c) FFT profile and (d) particle size distribution profile of the KLu_2F_7 nanoparticles before the thermal annealing. (e) TEM, (f) HR-TEM image, (g) FFT profile and (h) particle size distribution KLu_2F_7 nanoparticles after the thermal annealing process.

The HAADF-STEM images of $\text{KLu}_2\text{F}_7:38\% \text{Yb}^{3+}, 2\% \text{Er}^{3+}$ UC nanoparticles before the thermal annealing process are measured as shown in Figure 5.5. Before the annealing process, the HR-TEM images present a good crystallinity inside of the nanoparticles, but there are many defect and amorphous clusters (disordered ions) at the particles surface areas. After the annealing process,



the HR-TEM images present a good crystallinity at the particles surface areas. The detailed observation are was studies by the following HAADF STEM measurement.

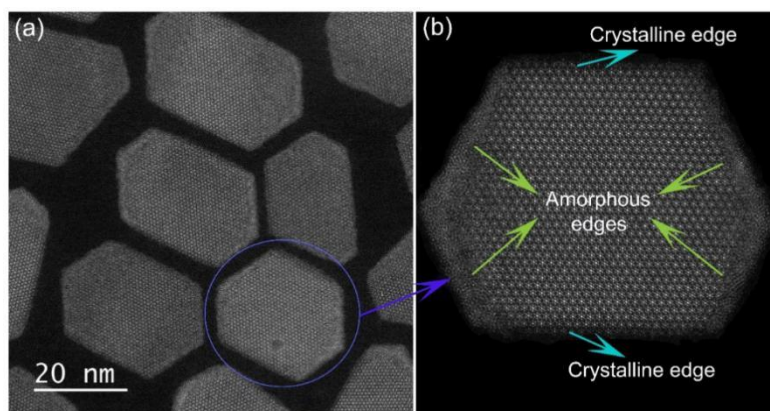


Figure 5.5(a) Atomic-scale and (b) magnified blue circle area in (a) images of $\text{KLu}_2\text{F}_7:38\% \text{Yb}^{3+}$, $2\% \text{Er}^{3+}$ UC nanoparticles before the thermal annealing process.

The atomic structure of KLu_2F_7 UC nanoparticles overlaps with the atomic position of Lu to show a higher contrast, while the overlap with the single atomic position of Lu shows that the contrast projected along the A axis is weak. The positional difference between the overlapping atomic position and the single atomic position column can be clearly observed (Figure 5.6a). The magnified HAADF-STEM images exhibit an overlay of the orthorhombic (011) atomic model and agree well with the experimental atom positions (Figure 5.6b). All the atom columns are clearly resolved, and the contrast is homogeneous across the entire image. This verifies that Yb^{3+} and Er^{3+}



ions substitute the crystal sites of Lu^{3+} successfully in an atom-scale, instead of entering the interstitial sites in the matrix.

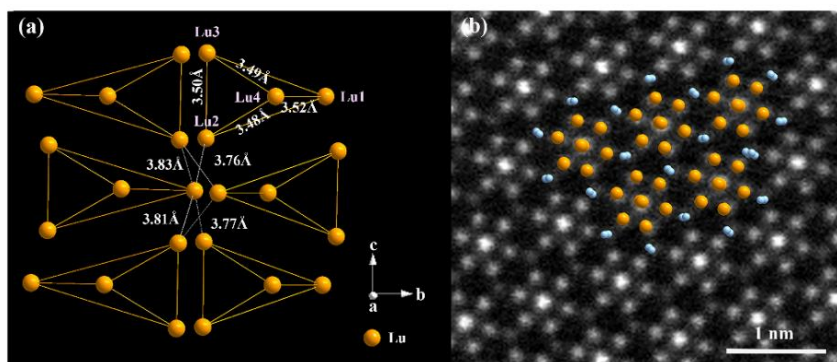


Figure 5.6 (a) Crystal structure mode of KLu_2F_7 . (Distances between two Lu^{3+} in different positions are $d_{(\text{Lu}4-\text{Lu}1)}=3.52\text{Å}$, $d_{(\text{Lu}4-\text{Lu}2)}=3.48\text{Å}$, $d_{(\text{Lu}4-\text{Lu}3)}=3.49\text{Å}$ and $d_{(\text{Lu}2-\text{Lu}3)}=3.50\text{Å}$ in the cluster.) (b) Atomic resolution crystal experimental and simulated structure images of a $\text{KLu}_2\text{F}_7:38\% \text{Yb}^{3+}$, $2\% \text{Er}^{3+}$ UC nanoparticle before the thermal annealing. The averaged distance between the ionic clusters ($3.76\text{-}3.83\text{ Å}$) is substantially larger than the ionic distance within the clusters ($3.48\text{-}3.52\text{ Å}$). The atomic structure of tetrad clusters that in a KLu_2F_7 host matrix Lu^{3+} ions are separated as arrays of discrete clusters at the sub-lattice level can be clearly observed in the (100) projection.

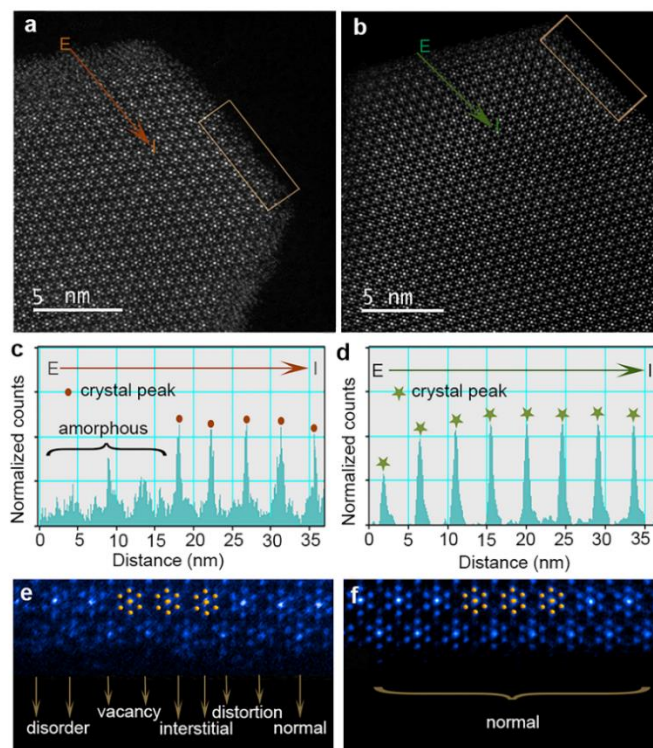


Figure 5.7 HAADF-STEM images of $\text{KLu}_2\text{F}_7:38\% \text{Yb}^{3+}, 2\% \text{Er}^{3+}$ UC nanoparticles (a) before and (b) after the thermal annealing at 240°C . Intensity profiles recorded by scanning along with the directions (c) orange and (d) green arrows of the UC nanoparticles as shown in Figures (a) and (b) respectively. Enlarged crystal edge structure images (e) before and (f) after the thermal annealing.

The comparison HAADF-TEM images of the KLu_2F_7 before and after the annealing process are shown in Figure 5.7. We observe that after the thermal annealing process, the amorphous or the disorder atoms at the surface of the particles shows good crystallinity and the atoms at the center of the particle still shown good crystallinity. The fundamental behavior of the edge structure is characterized by the peak-to-valley intensities. Figures 5.7c and 5.7d show the intensity profile



before and after the thermal annealing respectively extracted from the experiment (*i.e.* see the arrow E \rightarrow I). The relaxed intensity profile of the amorphous edge shows that the uncompleted crystallization process is observed for the as-grown sample. This is because the uncompleted growth of UC nanoparticles (Figure 5.7e) leads to the lattice disorder, vacancy, or interstitial form the surface defect states. On the other hand, the unrelaxed crystal edges of the (011) planes are well-crystallized with the regular structure. The magnified atomic-scale image (Figure 5.7f) shows no missing or exceeding of Lu ions at the outmost layer of the UC nanoparticles.

Furthermore, the clear atomic image shows the uniform thickness of the UC nanoparticles has ten atomic layers (Figure 5.8). This 2-dimensional sheet structure ensures the crystal growth is constrained in the plane perpendicular to (100) lattice orientation so that any interstitials and stacking faults will only appear near the edge of the UC nanoparticles. The clustering structure can be observed in the (010) projection. The interplanar spacing in HR-TEM is 0.59 nm, which is corresponding to the distance between the two atom layers in the (010) direction. Thus, a UC nanoparticle consists of ten atomic layers.

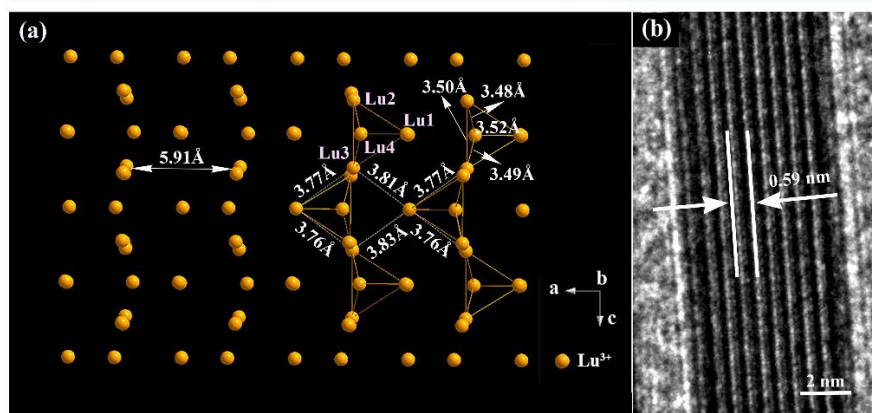


Figure 5.8 (a) Crystal structure mode of KLu_2F_7 in the (010) projection. (b) The HR-TEM image of a KLu_2F_7 :38% Yb^{3+} , 2% Er^{3+} UC nanoparticle after the thermal annealing.

5.4 The enhancement of UC photoluminescence by suppressing the surface defects of the UC nanoparticles

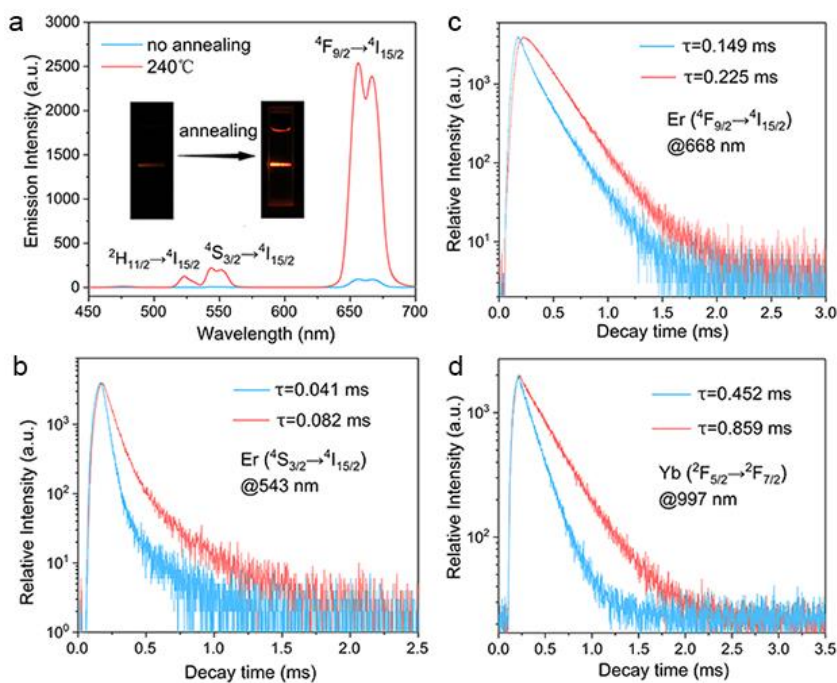


Figure 5.9 (a) photoluminescence spectra of the KLu_2F_7 :38% Yb^{3+} , 2% Er^{3+} UC nanoparticles. Decay curves of (b) $^4\text{S}_{3/2} \rightarrow ^4\text{I}_{15/2}$ transition (@543 nm), (c) $^4\text{F}_{9/2} \rightarrow ^4\text{I}_{15/2}$ transition (@668 nm), and (d) $^2\text{F}_{5/2} \rightarrow ^2\text{F}_{7/2}$ transition (@980 nm) of the UC nanoparticles.

In order to study the photoluminescence properties under the influence of surfaces defects, the UC photoluminescence spectra of $\text{KLu}_2\text{F}_7:38\% \text{Yb}^{3+}, 2\% \text{Er}^{3+}$ UC nanoparticles before and after the annealing process are measured as shown in Figure 5.9a. It is noted that after the thermal annealing at 240 °C, the $\text{KLu}_2\text{F}_7:38\% \text{Yb}^{3+}, 2\% \text{Er}^{3+}$ UC nanoparticles exhibit a simultaneous enhancement of green and red emission intensities by more than 10 times than that of the particles before the thermal annealing. The decay curves of the ${}^4\text{S}_{3/2} \rightarrow {}^4\text{I}_{15/2}$ transition (@543 nm) of the UC nanoparticles before and after the thermal annealing are also shown in Figure 5.9b. It is noted that the decay times have been increased by ~100% after the application of annealing. Increases of ${}^4\text{F}_{9/2} \rightarrow {}^4\text{I}_{15/2}$ (@668 nm) and ${}^4\text{F}_{5/2} \rightarrow {}^4\text{F}_{7/2}$ (@980 nm) decay lifetime by ~50% and ~90% respectively are also observed after the thermal annealing (according to figure 5.9d and 5.9d).

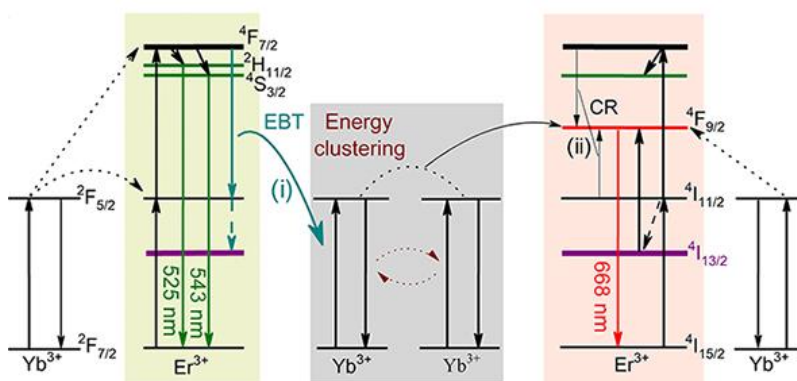


Figure 5.10 Simplified energy transfer diagram of the UC nanoparticles under continuous wave (CW) 980 nm laser excitation.



Figure 5.10 describes the green and red radiative recombination processes of the KLu₂F₇:38%Yb³⁺, 2%Er³⁺ UC nanoparticles. The dominant red emission can be explained by the enhancement of (i) energy back transfer (EBT) process with the influence of high doping concentration of Yb³⁺ and (ii) cross relaxation (CR) process. We measure the photoluminescence spectra of the KLu₂F₇: x%Yb³⁺, 2%Er³⁺ (x=18-98) UC nanoparticles after the thermal annealing (Figure 5.11). All the samples are excited at 980 nm with a 1.3W CW laser diode. The emission spectra are normalized to the emission intensity of Er³⁺ at 543 nm. Under a CW laser diode pumping at 980 nm, the UC emission bands of near-ultraviolet (NUV) (380 nm, ⁴G_{11/2}→⁴I_{15/2}), violet (408 nm, ²H_{9/2}→⁴I_{15/2}), green (525 and 543 nm, ²H_{11/2}, ⁴S_{3/2}→⁴I_{15/2}) and red (668 nm, ⁴F_{9/2}→⁴I_{15/2}) originated from Er³⁺ ions can be observed. UC photoluminescence spectra confirm that the emission intensity of Er³⁺ ions increased with the increase of Yb³⁺ concentration, without exhibiting the concentration quenching phenomenon due to the unique clustering structure of KLu₂F₇. The inset is the enlarged emission spectra in NUV and violet regions (left) and the typical photographs of the UC luminescence (right) of KLu₂F₇: x%Yb³⁺, 2%Er³⁺ (x=18, 48, and 98) UC nanoparticles, respectively. The ratio of the violet-to-green and red-to-green emission intensity increases gradually along with the concentration of Yb³⁺ from 18 to 98 mol%, which derives from the EBT process. Meanwhile, the photographs in the inset display that the UC emission color changes from green-yellow in KLu₂F₇:18%Yb³⁺, 2%Er³⁺ to red in KLu₂F₇: 98%Yb³⁺, 2%Er³⁺. This is because the EBT and CR processes reduce the population at the ⁴F_{7/2} state which supplies carriers to realize radiative recombination between (²H_{11/2}, ⁴S_{3/2}) and ⁴I_{15/2} states (*i.e.* green emission). The realization of high-intensity red emission (*i.e.* enhancement of EBT and CR

processes) and prolonged carrier lifetime indicates that the removal of amorphous surface and the improvement of surface crystallinity by the thermal annealing process.

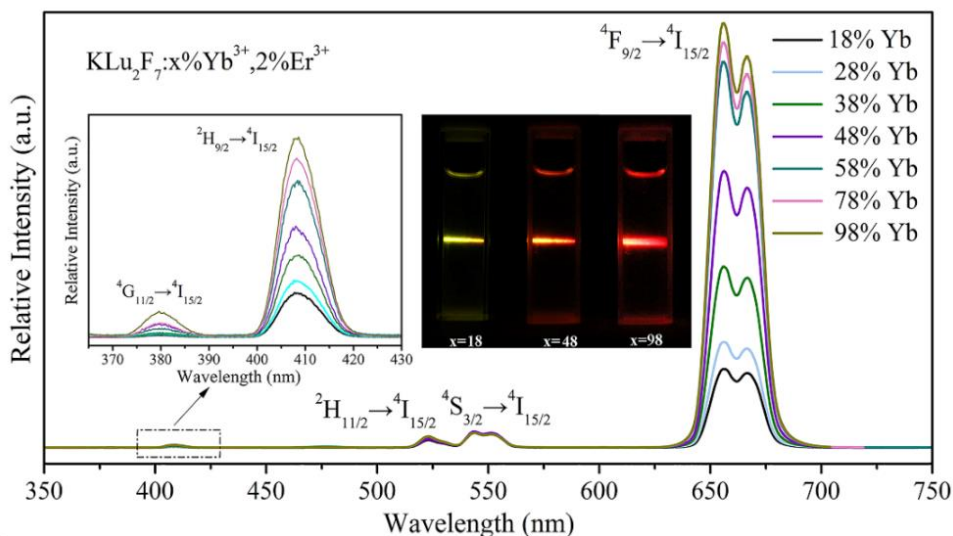


Figure 5.11 Room temperature UC photoluminescence spectra of $\text{KLu}_2\text{F}_7: x\% \text{Yb}^{3+}, 2\% \text{Er}^{3+}$ ($x=18$ -98) UC nanoparticles after the thermal annealing process.

In this experiment, we observe that the decay lifetime of ${}^2\text{H}_{11/2}$ and ${}^4\text{S}_{3/2} \rightarrow {}^4\text{I}_{15/2}$ increases the green emission, but the relative intensity of red emission is reduced. Hence, high crystallinity of the $\text{KLu}_2\text{F}_7: 38\% \text{Yb}^{3+}, 2\% \text{Er}^{3+}$ UC nanoparticles will favor green emission (*i.e.* short decay lifetime) under pulsed laser excitation with pulsewidth close to that of the green decay lifetime. Figures 5.12a and 5.12 b plot the UC emission spectra of $\text{KLu}_2\text{F}_7: 38\% \text{Yb}^{3+}, 2\% \text{Er}^{3+}$ nanoparticles under 980 nm pulsed laser excitation (*i.e.* pulsewidth: CW, 5ms, 0.5ms, 50 μs , and 6ns) before and after the thermal annealing respectively. It is observed that the enhancement of green emission and

suppression of red emission are observed simultaneously under the pulsed laser excitation with pulsewidth of 6 ns. This verifies that the suppression of non-radiative recombination at the short transient time and high-crystallinity of UC nanoparticles should obtain after the thermal annealing.

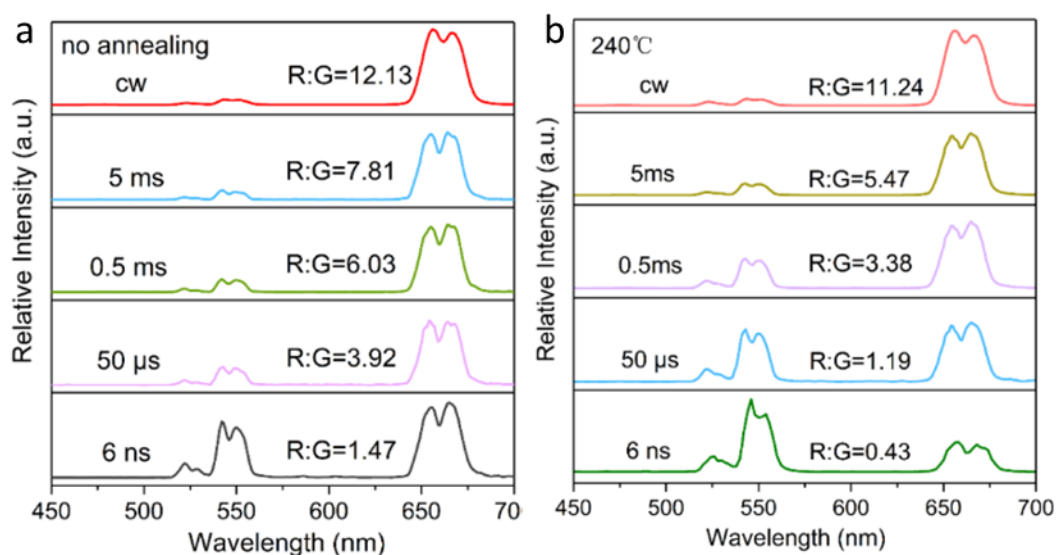


Figure 5.12 (a) Before and (b) after the thermal annealing obtained through the excitation of 980 nm with different laser pulse excitation with pulsewidth from CW to 6 ns.

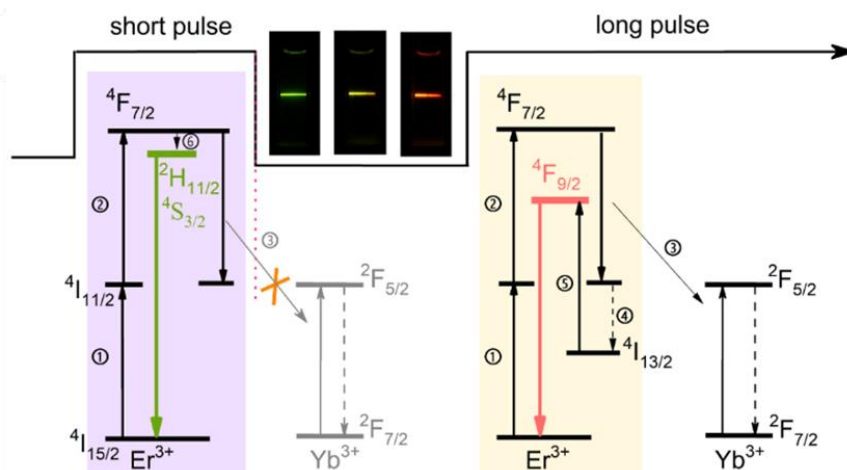




Figure 5.13 Proposed energy transfer process of KLu₂F₇:Yb³⁺, Er³⁺ UC nanoparticles under 980 nm short and long pulsed laser excitation. UC emission spectra of KLu₂F₇:38% Yb³⁺, 2%Er³⁺ UC nanoparticles

Figure 5.13 explains how KLu₂F₇:38% Yb³⁺, 2%Er³⁺ UC nanoparticles response to the influence of pulse laser excitation. The key factors of red emission from KLu₂F₇:Yb³⁺, Er³⁺ UC nanoparticles with a high concentration of Yb³⁺ are the EBT process (step ③) together with the decay of ⁴I_{11/2}→⁴I_{13/2} of Er ions (step ④) as shown under the long pulse operation, see right-hand side of Figure 5.13. On the other hand, the green emission rate from the ²H_{11/2} and ⁴S_{3/2} states are fast due to a direct two-step population procedure and a non-radiative relaxation process with a small energy gap. This can be validated by the time-resolved photoluminescence studies under 980 nm short-pulse excitation, see left-hand side of Figure 5.13. The EBT and the non-relaxation process of step ④ can be suppressed by the short excitation pulses, which contributes to the decrease of the R: G emission intensity ratio. It is noted that EBT (step 3) and non-radiative relaxation (⁴I_{11/2}→⁴I_{13/2}, step 4) processes are suppressed under short-pulse (< 100 ns). This is because ²H_{11/2} and ⁴S_{3/2} are populated (step 6) before the ⁴F_{7/2} → ⁴I_{11/2} transition can take place under short-pulse excitation. The low-temperature UC spectra (Figure 5.14) shows that the non-radiative relaxation process from ⁴I_{11/2} to ⁴I_{13/2} is suppressed at low temperature. This is proved by the decrease of R:G emission intensity ratio at 77 K. Therefore, it is conceivable that the phonon-assisted energy transfer process benefits to the realization of non-radiative relaxation, which could lead to the delay of red emission. Consequently, the non-radiative relaxation process of Er³⁺ from ⁴I_{11/2}→⁴I_{13/2} can be suppressed by short pulse source excitation.

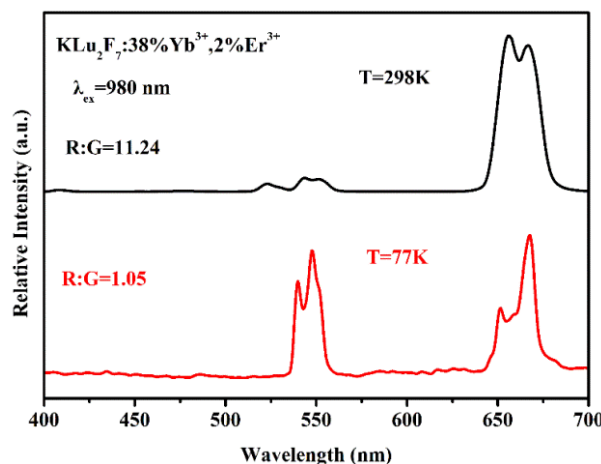


Figure 5.14 UC photoluminescence spectra of the $\text{KLu}_2\text{F}_7:38\% \text{Yb}^{3+}, 2\% \text{Er}^{3+}$ UC nanoparticles under the excitation of 980 nm in 298K (room temperature) and 77K.

In addition, time-dependent Er^{3+} emission profiles of the $\text{KLu}_2\text{F}_7:38\% \text{Yb}^{3+}, 2\% \text{Er}^{3+}$ UC nanoparticles after the thermal annealing at 543 and 668 nm upon a pulsed excitation at 980 nm are measured as shown in Figure 5.15. The non-steady-state UC mechanism proposed for Er^{3+} emission on the pulsed excitation at 980 nm is validated by the time-resolved photoluminescence studies. Under the excitation of a 10-ms-wide laser pulse, the rate of change in the red emission of Er^{3+} ions is appreciably slower than that of the green emission for the extra step of the non-relaxation from $^4\text{I}_{11/2}$ to $^4\text{I}_{13/2}$, which is needed to populate the $^4\text{F}_{9/2}$ state of Er^{3+} . The green and red emission intensities gradually became equal after 3.5 ms, and remain unchanged under further excitation as presented in the figure.

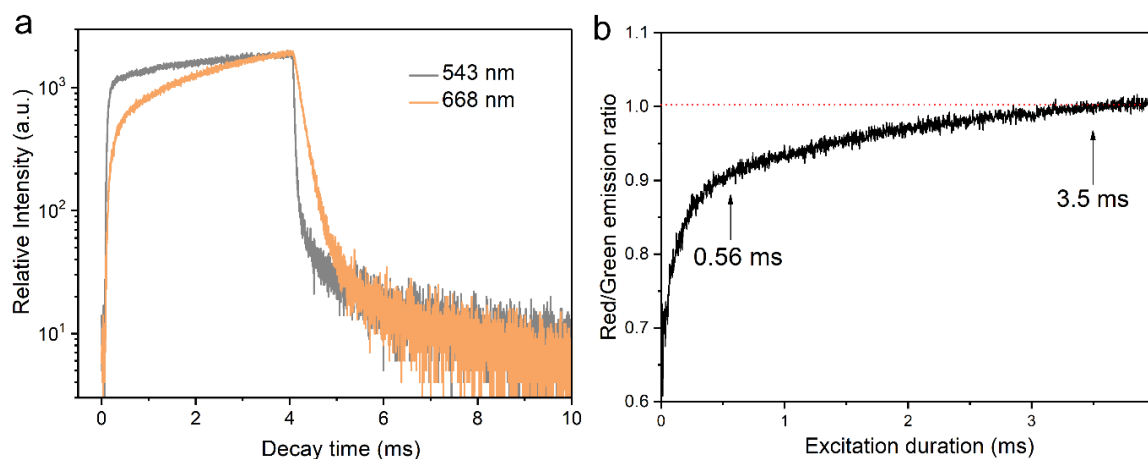


Figure 5.15 (a) Time-dependent Er^{3+} emission profiles of the $\text{KLu}_2\text{F}_7:38\% \text{Yb}^{3+}, 2\% \text{Er}^{3+}$ UC nanoparticles after the thermal annealing at 543 and 668 nm upon a pulsed excitation at 980 nm with a duration of 10 ms. (b) Corresponding R:G emission intensity ratio measured as a function of excitation duration.

As shown in Figure 5.16, the average pump power of CW 980 nm laser decreases along with the decrease of the pulse width. This indicates that the R:G emission intensity ratio depends on the increasing pump power under the excitation of CW 980 nm laser and pulsed (6ns) operation. On the other hand, we find that the R:G emission intensity ratio exhibits no obvious change. This proves that the decreased average pump power has a negligible influence on the R:G ratio, which critically depends on the pulse width of excitation energy.

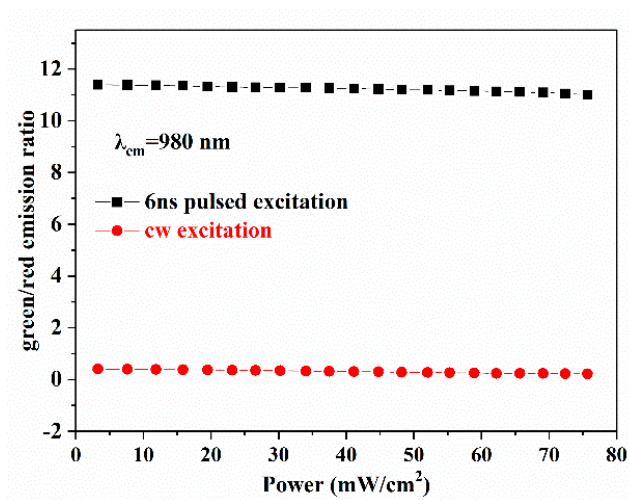


Figure 5.16 Power dependence of the red to green UC emission intensity ratio after the thermal annealing under the excitation of CW 980 nm laser and a pulsed laser (6ns).

5.5 Design and realization of lasing emission from the recovered KLu_2F_7 UC nanoparticles

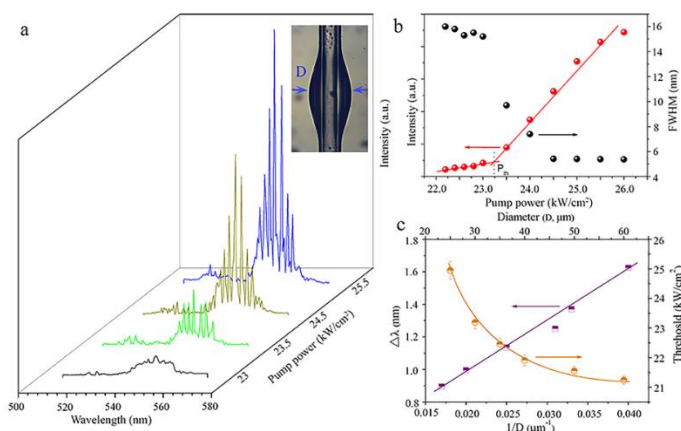




Figure 5.17 (a) Lasing spectra of a microcavity using KLu₂F₇:38% Yb³⁺, 2%Er³⁺ UC nanoparticles as the gain medium under 980 nm pulse laser excitation at room temperature. The inset shows the photo of the laser microcavity. (b) Output power and emission linewidth *versus* excitation power. (c) Measured values of P_{th} and $\Delta\lambda$ *versus* D for the green emission based on the lasing microcavity.

Figure 5.17a plots the emission spectra of a microcavity (with diameter $D = 31 \mu\text{m}$) using KLu₂F₇:38% Yb³⁺, 2%Er³⁺ UC nanoparticles as the gain medium (*i.e.* a mixture of UC nanoparticles and silica resin) under 980 nm pulsed (6 ns) laser excitation at room temperature. A broad emission band with linewidth equal to ~ 16 nm is observed under low excitation power. When the excitation power larger than threshold P_{th} ($=23.25 \text{ kW/cm}^2$), the narrow peaks, which shows a linewidth of less than 0.5 nm, emerge from the emission spectra. In addition, the linewidth of the envelope of the emission spectra reduces from ~ 16 to ~ 5.5 nm with the increase of excitation power and the output intensity of the green lasing emission increases linearly with $P > P_{th}$. The observation of a kink in the UC intensity *vs* pump density curve and the narrow of the envelope of the emission spectra at $P = P_{th}$ (Figure 5.17b) prove that the KLu₂F₇:38% Yb³⁺, 2%Er³⁺ nanoparticles have high optical gain to support green lasing emission. Figure 5.17c shows the measured P_{th} and $\Delta\lambda$ of microcavities with a different value of diameter. It is expected that P_{th} decreases with the increase of D as a long laser cavity allows better amplification of resonant modes. If the side of the microcavity supports resonant optical feedback, mode spacing between the adjacent narrow peaks, $\Delta\lambda$, observed from the spectra can be expressed as:[\[72\]](#)



$$\Delta\lambda = \lambda_0^2 / \pi D n_{eff} \quad (5.1)$$

Where λ_0 (=547 nm) is the center peak wavelength and n_{eff} is the effective refractive index of the microcavity. By using (5.1) to fit the measured data of $\Delta\lambda$ and D , it is deduced that n_{eff} is ~ 1.58 , which is close to the refractive index of the silica resin. Hence, this confirms that the microcavities support whispering gallery modes (WGMs). On the other hand, red emission is suppressed for P larger than P_{th} so that its emission spectra are not shown in the figure. Realization of green lasing emission indicates that high crystallinity UC nanoparticles are formed through surface defects restoration.

5.6 Summary

In this chapter, the mechanism of the surface defects restoration on the photoluminescence properties are studied in detailed and the enhancement of UC intensity can be achieved after the thermal annealing process. The clustering structure of the thin KLu₂F₇:38%Yb³⁺, 2%Er³⁺ UC nanoparticles can be directly observed at the atomic scale by using the HAADF-STEM measurement. Thanks to the proposed thermal annealing method and the arrangement of the lanthanum ions in the particle surface, the activators located at the crystal sites of Lu³⁺ have been recovered without bringing undesired defects. Under CW 980 nm laser excitation, the improvement of UC emission intensity by an order of magnitude is observed. This indicates that the influence of surface quenching appears before the thermal annealing, has been suppressed. On the other hand, under 980 nm pulsed laser (6 ns) excitation, the green lasing emission is dominant from the lasing spectra. The fast-transient response to the ²H_{11/2} and ⁴S_{3/2} states and the suppression



of the EBT process further verify that the high crystallinity of the UC nanoparticles can be restored after the thermal annealing process.



6. Optical properties of Ln^{3+} -doped LuF_3 UC nanoparticles

6.1 Introduction

Lanthanide (Ln^{3+})-doped upconversion (UC) nanoparticles have attracted enormous attention for the application in optical imaging-guided bio-imaging, therapeutics, anti-counterfeiting, and active photonic devices. Even though UC nanoparticles have many desired optical features, one of the major hurdles in the applications is their low efficiency. Therefore, to realize the full potential of these UC nanoparticles, it is important to manipulate the growth processes of the UC nanoparticles so that the corresponding optical performance can be optimized.[\[108\]](#) However, we still have an insufficient understanding on the growth mechanism of the UC nanoparticles in solution. This is because it is a challenge to directly visualize the nanoscale growth processes of nanoparticles in the liquid medium.

Here, we propose to use *in situ* transmission electron microscopy (TEM) technology, which can provide a direct imaging platform to visualize the growth characteristic, [\[109, 110\]](#) to study the optical performance of Er^{3+} , Yb^{3+} co-doped LuF_3 nanoparticles. In the experiment, we observe the appearance of amorphous clusters, which act as the metastable state of the nanoparticles, can be crystallized under electron beam irradiation. We use the thermal annealing method to remove the surface amorphous clusters of the UC nanoparticles during the thermal annealing process. It can be shown that the UC nanoparticles show perfectly crystallized structure even at large surface area with UC emission intensity to be improved by more than 10 times under continuous wave (CW) 980 nm laser pump. We verify that the exhaustion of surface amorphous



cluster, which acts as the impurities and quenching centers, enhances the UC energy transfer process and UC efficiency.

6.2 Fabrication of LuF₃ nanoparticles

6.2.1 Fabrication methods

Synthesis of LuF₃: Yb³⁺, Er³⁺ nanoparticles. The LuF₃: Yb³⁺, Er³⁺ nanoparticles were prepared by the co-precipitation method. The RECl₃ (RE=Lu³⁺, Yb³⁺, and Er³⁺) compounds were prepared by dissolving the corresponding RE₂O₃ compounds in a hot HCl solution. In the typical synthesis, LuCl₃ (1mmol), YbCl₃ (0.18mmol) and ErCl₃ (0.02mmol) was add into the mixture of OA (8 mL) and 1-octadecene (12mL) under vigorous stirring at room temperature. The mixture was heated to 150 °C for 30 min to remove the water and oxygen. After the reaction solution was cooled to room temperature, the NH₄F (4 mmol) dissolved in methanol (25mL) was quickly injected into the solution. The mixture was heated to 50 °C for 30 min and then heated to 80 °C for 1h to remove the methanol. Subsequently, the solution was heated to 290 °C and keep for 90 min under an argon atmosphere. Then the reaction was slowly cooled to room temperature. The nanoparticles were collected after centrifugation, wash several times with ethanol and cyclohexane, and dispersed in cyclohexane. Other samples of LuF₃: Yb³⁺, Er³⁺ nanoparticles were synthesized by a similar procedure except for different keeping time at the last step.



6.2.2 The thermal annealing methods

The thermal annealing of LuF₃: Yb³⁺, Er³⁺ nanoparticles. 8ml OA and 12ml ODE were added into the three-neck round-bottom flask under vigorous stirring at room temperature, and then the mixture solution was heated to 150 °C for 30 min under an argon atmosphere to remove the oxygen. After the reaction solution was cooled to room temperature, the 0.5 mmol as-synthesized core was added into the mixture solution keep at 50 °C for 30 min and then heated to 80 °C for 1h to evaporate cyclohexane. Finally, the mixture solution was heated to 240 °C for 1.5h. After cooling down to the room temperature, the annealed nanoparticles were washed for several with and ethanol and cyclohexane, and re-dispersed in cyclohexane.

6.3 Physical and optical properties of Ln³⁺-doped LuF₃ UC nanoparticles

6.3.1 XRD, TEM, optical characteristics measurement of LuF₃ UC nanoparticles

General measurement: XRD patterns were performed on a D8 Focus diffractometer using Cu-K α radiation ($\lambda=0.15405$ nm) to identify the crystallization phase. The particle size, shape, structure, and composition were studied with TEM images using JEM-2100 at 200 kV. The *in situ* experiment was carried out under electron beam radiation. Aberration-corrected high angle annular dark field (HAADF) scanning transmission electron microscopy (STEM) images were recorded by a JEOL JEM-ARM200F TEM/STEM with a spherical aberration corrector.

Optical measurements: The emission and temperature-dependent photoluminescence spectra of the sample at various temperatures were measured by HITACHI-F7000 spectrometer under CW 980 nm laser excitation. The Raman spectra were measured by HR-800 (HORIBA, Japan) Confocal Raman Microscope. The UC spectra of the single nanoparticles measurement set are shown in Figure 6.1.

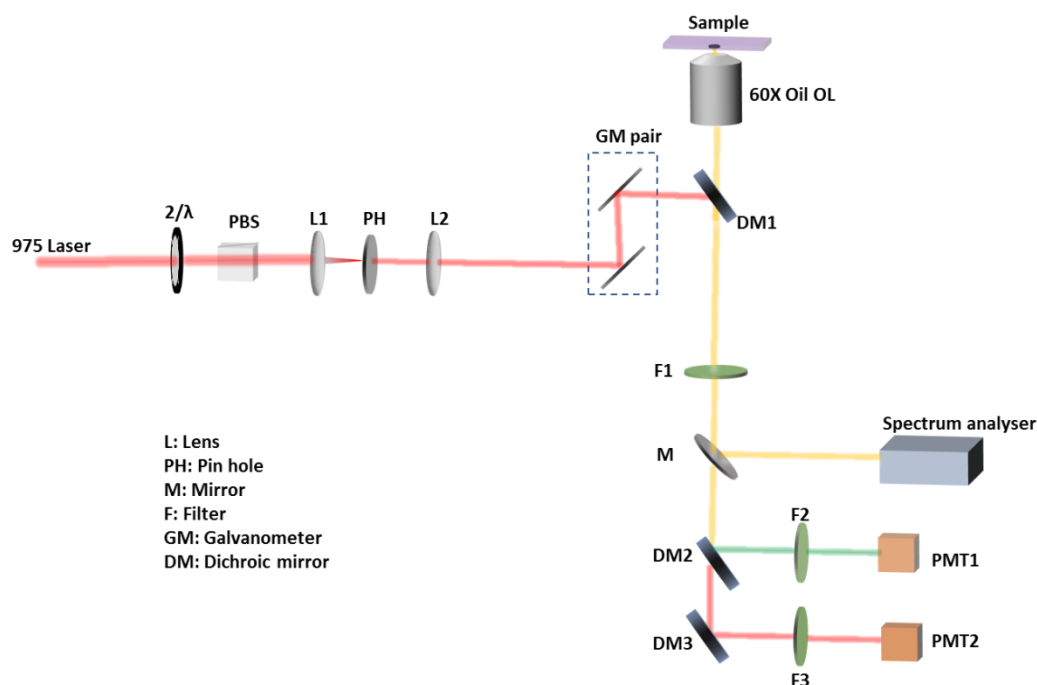


Figure 6.1 Schematic diagram of the single nanoparticle photoluminescence measurement setup. PMT1, PMT2: photomultiplier tubes; M is Ag reflection mirror, L1 and L2 are Lens; F is filter, F1: 975 nm band-pass Filter; F2: 550nm short-pass Filter; F4: 654nm band-pass Filter; GM: Galvanometer scanning mirrors; DM1: 975 nm short-pass dichroic mirror; DM2: 550nm short-pass dichroic mirror; DM3: 654 nm long-pass dichroic mirror.

6.3.2 General properties of LuF₃

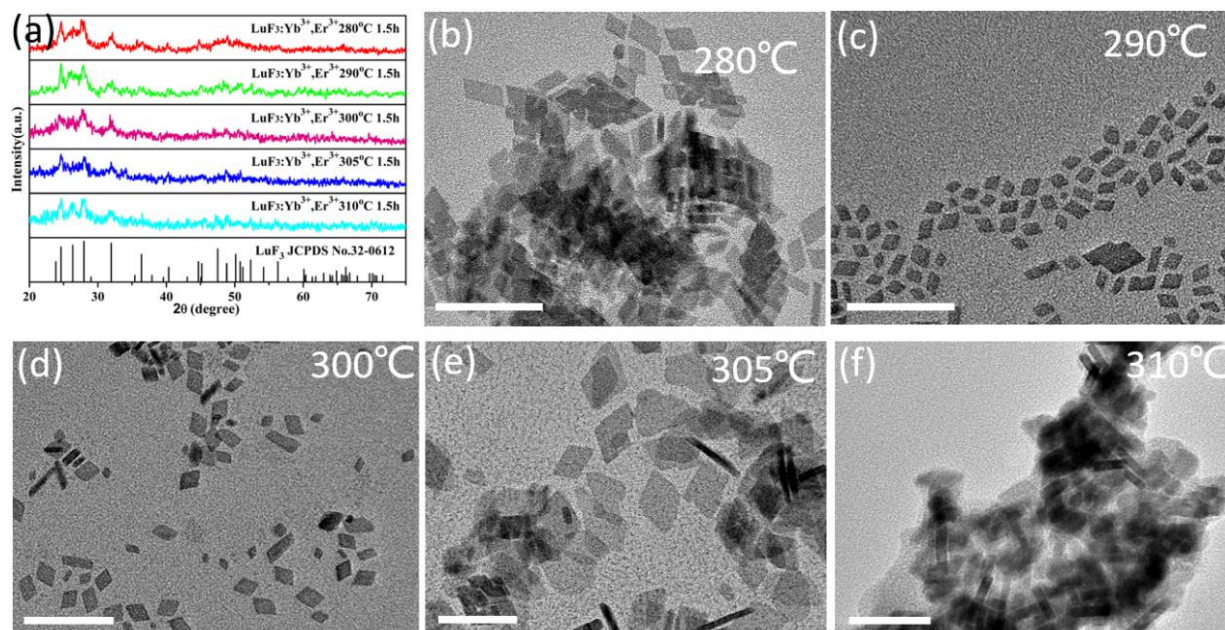


Figure 6.2 (a) XRD patterns of LuF₃: Yb³⁺, Er³⁺ nanoparticles at different synthetic temperature and (JCPDS No.32-0612). TEM images of LuF₃: Yb³⁺, Er³⁺ nanoparticles at different reaction temperature. (b) 280 °C, (c) 290 °C, (d) 300 °C, (e) 305 °C, (f) 310 °C. The scale bars are 50nm.

The LuF₃: Yb³⁺, Er³⁺ nanoparticles are synthesized at different temperature (from 280 to 310°C) via co-precipitation method (Figure 6.2). XRD pattern of LuF₃: Yb³⁺, Er³⁺ nanoparticles at different reaction temperature can be well indexed as the orthorhombic phase of LuF₃ (JCPDS No.32-0612). When the reaction temperature reaches 290 °C, the nanoparticles show monodisperse size distribution and without aggregation.

6.3.3 Photoluminescence properties with the relationship of the morphology of the LuF_3 nanoparticles

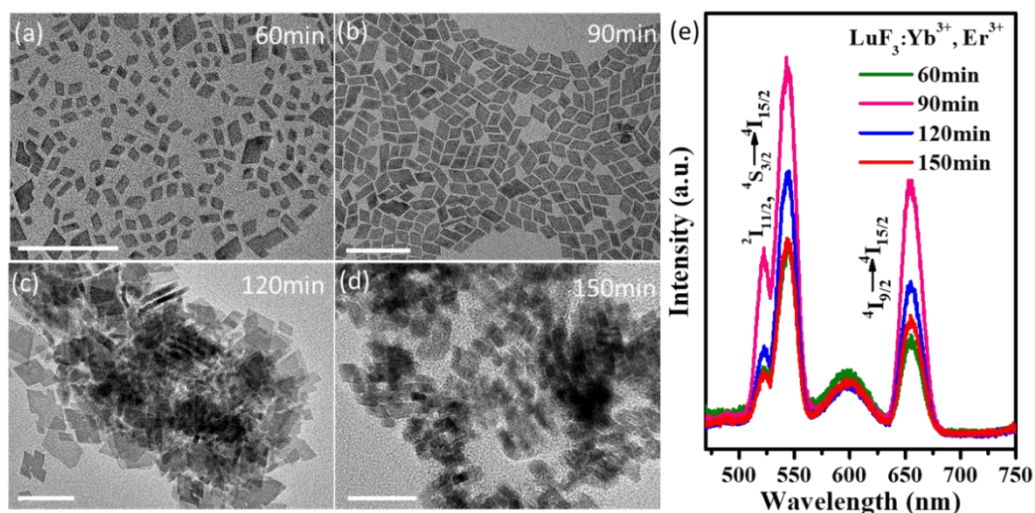


Figure 6.3 TEM images $\text{LuF}_3:\text{Yb}^{3+}, \text{Er}^{3+}$ nanoparticles at 290°C for (a) 60, (b) 90, (c) 120, and (d) 150 mins reaction time. Scale bars, 50nm. (e) Photoluminescence spectra of the LuF_3 nanoparticles under CW 980 nm excitation at room temperature.

It is found that the monodispersed nanoparticles with uniform-morphology are obtained at an optimum reaction temperature of 290°C . Furthermore, we repeat synthesizing the nanoparticles at 290°C for different reaction time and the corresponding TEM images are shown in Figure 6.3. When the reaction time reaches 60 min, non-uniform size of nanoparticles is obtained. For reaction time increases to 90 min, uniform distribution of LuF_3 nanoparticles is achieved. With further increase of reaction time, the growth and agglomerate of the nanoparticles occur simultaneously.



The corresponding photoluminescence spectra are also shown in Figure 6.3e. It is noted that the LuF₃ synthesized at 290 °C for 90 min has the highest emission intensity. Hence, the optimum temperature and time to fabricate LuF₃:Yb³⁺, Er³⁺ nanoparticles with uniform size and high-optical-quality are found to be 290 °C and 90 min respectively.

6.4 Growth mechanism of LuF₃ nanoparticles

6.4.1 Growth and coalescence processes of LuF₃ nanoparticles

Figure 6.4 shows the TEM and selected area electron diffraction (SAED) images of a LuF₃:Yb³⁺, Er³⁺ nanoparticle obtained from the optimized growth conditions (i.e. 290 °C, 90 min). The HR-TEM image clearly shows the lattice fringes at the interior and edges of the nanoparticle. The lattice fringes display the typical d-spacing of ~0.361 and ~0.338 nm which corresponding to the (101) and (020) crystal planes of LuF₃ respectively. The concentric diffraction spots observed from the SAED pattern correspond to the specific (101) and (020) planes of the LuF₃ lattice. In order to further depict the morphology of the as-synthesized LuF₃ nanoparticle, a HAADF-STEM image was measured, as shown in Figure 6.4c. The well-organized atoms crystalize with (101) plane (green arrow) is observed in the interior of the nanoparticles. However, crystallization is partially achieved at the edge of the nanoparticle at the (020) crystal plane (cyan arrow) and the edge of the as-growth UC nanoparticles has an epitaxial amorphous state (magenta arrow) and single atoms (orange circles). The high density of the impurities and imperfect crystal lattices at the surface could result in the low UC energy transfer efficiency. To obtain high UC energy transfer efficiency, it is required to remove surface amorphous clusters. The energy transfer

process is a major process for the UC emission on the Yb^{3+} - Er^{3+} co-doped nanoparticle. Briefly, incident pump light 980 nm near-infrared (NIR) is mainly absorbed by donor Yb^{3+} ion, which then excites a near Er^{3+} ion into $^4\text{I}_{11/2}$ level through the Forster energy transfer process. Other Yb^{3+} can also transfer its energy to Er^{3+} to raising it high energy level from which unconverted luminescence is submitted. When the surface defect shows high density, the nonradioactive transitions (violet line in Figure 6.4f) would show the high frequency and lead to the low energy transfer efficiency. Thus, we conclude that the amorphous clusters at the surface are the main impurities which need to be eliminated. In addition, the amorphous nanoclusters are observed and the metastable state of the LuF_3 nanoparticle, so it may show closely related to the amorphous clusters attached to the edges of the LuF_3 UC nanoparticles.

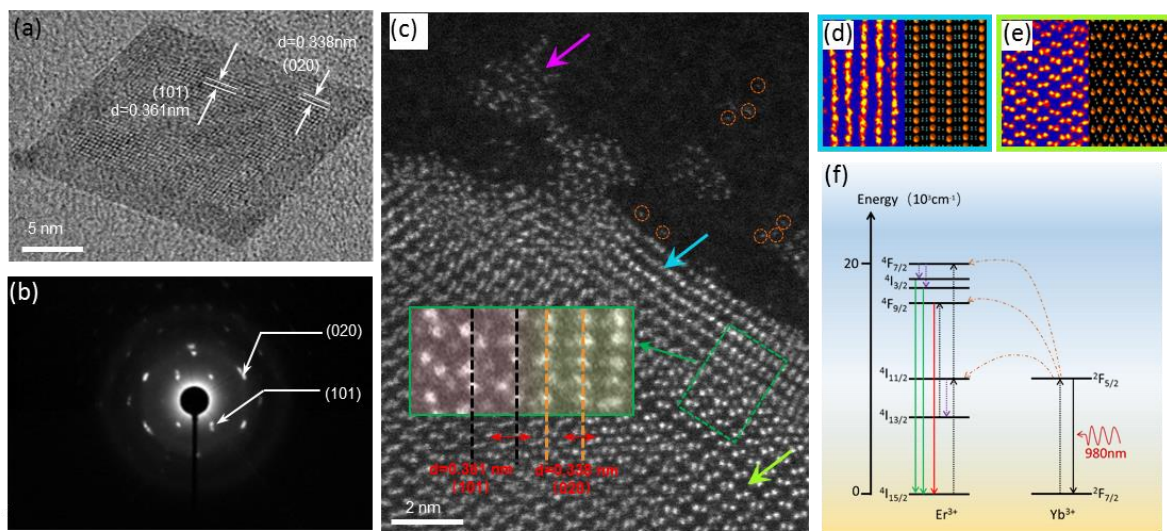
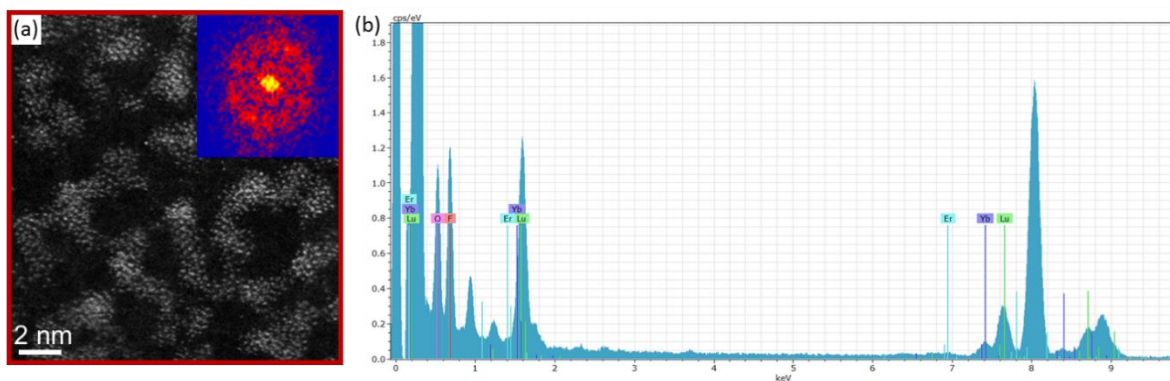


Figure 6.4 (a) HRTEM and (b) SAED images of a LuF_3 : Yb^{3+} , Er^{3+} nanoparticles obtained under the optimized fabrication conditions. (c) Atomic-resolution crystal structure image of the as-synthesized LuF_3 UCNC. The inset is the magnifying diagram of olive rectangular and the orange

circles present the single atoms. The atomic model of (d) and (e) are the corresponding regions as indicated by arrows in (c) respectively. (f) Energy transfer of the UC diagram of the Yb^{3+} - Er^{3+} co-doped UC nanoparticle. UC nanoparticle absorbs NIR light and emits UC green and red emissions. Violet line is the nonradiative transitions.

In order to study the growth process of the LuF_3 nanoparticles, precursor state of LuF_3 (amorphous clusters without crystallizing) are obtained by the co-precipitation method with shorter reaction time (i.e. 30 min). According to the HAADF-STEM and fast Fourier transform (FFT) images given in Figure 6.5a, the amorphous structure of LuF_3 nanoparticles shows no information of crystal-lattice fringes and energy-dispersive X-ray spectroscopy (EDS) spectrum displays mainly Lu, F, Yb, Er elements (Figure 6.5b).



To study the growth process of LuF_3 nanostructure, the precursors are dispersed in absolute ethyl alcohol and dripped onto the copper mesh for TEM observation. Under electron beam radiation, crystallization of LuF_3 nanostructure was realized as shown in Figure 6.6a. It shows the HR-TEM image of a LuF_3 amorphous nanocluster. By prolonging the exposure time, the amorphous nanocluster gradually crystallizes and grows to form a crystal. We observe that the amorphous nanocluster undergoes crystallizing in both horizontally and longitudinally direction under electron beam irradiation. Furthermore, the surrounding amorphous nanoclusters attach to the edges of the crystallized region of the nanoparticles (Figure 6.6b) is recognized. These studies clearly manifest that the growth of LuF_3 nanoparticle is mainly determined by the connection of amorphous nanoclusters.

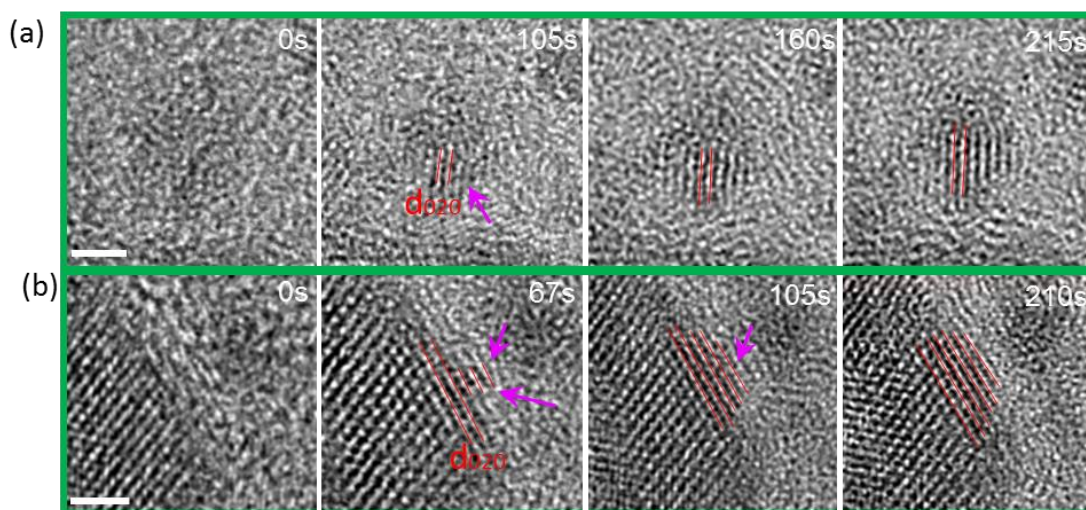


Figure 6.6 (a) Sequential time-resolved *in-situ* TEM images showing the crystallization process of LuF_3 : Yb^{3+} , Er^{3+} single nanoparticle. (b) Sequences of *in situ* TEM images indicate the growth of LuF_3 . The scale bar is 2nm. (Electron beam density, 4.8 A/cm^2).

The dynamic process of amorphous clusters joining two adjacent UC nanoparticles together to promote the growth which can be studied by *in situ* TEM technology as shown in Figure 6.7. At the initial stage, amorphous clusters attach to the edge at the lower-right direction of nanoparticle 3 and then crystallize under the electron beam irradiation. Subsequently, the nanoparticle 3 gradually conjugates with nanoparticle 4 and finally get together to accomplish edge-to-edge attachment process. The insignificant distance change between the UC nanoparticles 4 and 5 suggests these UC nanoparticles are stationary. The decrease in distance between UC nanoparticles 3 and 4 indicates that the amorphous nanocluster acts as a ‘glue’ to fill the gap between two UC nanoparticles together to form a bigger nanoparticle. These results demonstrate that the amorphous clusters which can be regarded as a binder between two UC nanoparticles play a key role in the growth process. This process can be also confirmed in Figure 6.8. These results demonstrate that the amorphous clusters which can be regarded as a binder between two UC nanoparticles play a key role in the growth process.

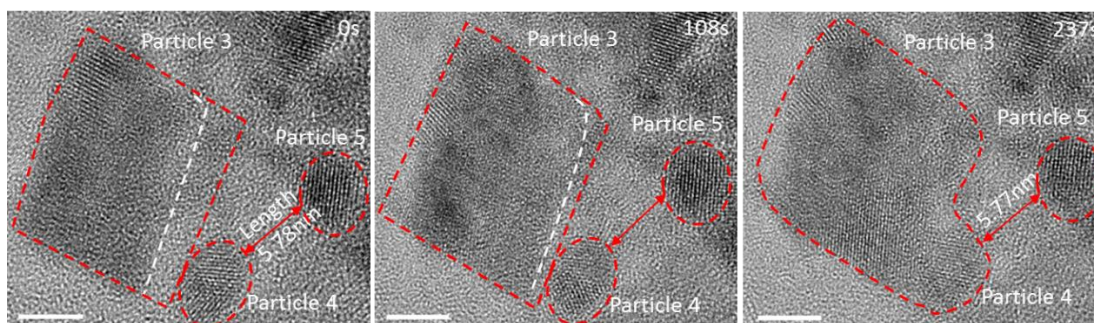


Figure 6.7 Sequential *in situ* HR-TEM images shown the details particle attachment process of the two nanoparticles with the assistance of the amorphous nanoclusters at the edges of the nanoparticles. Scale bar is 5nm.

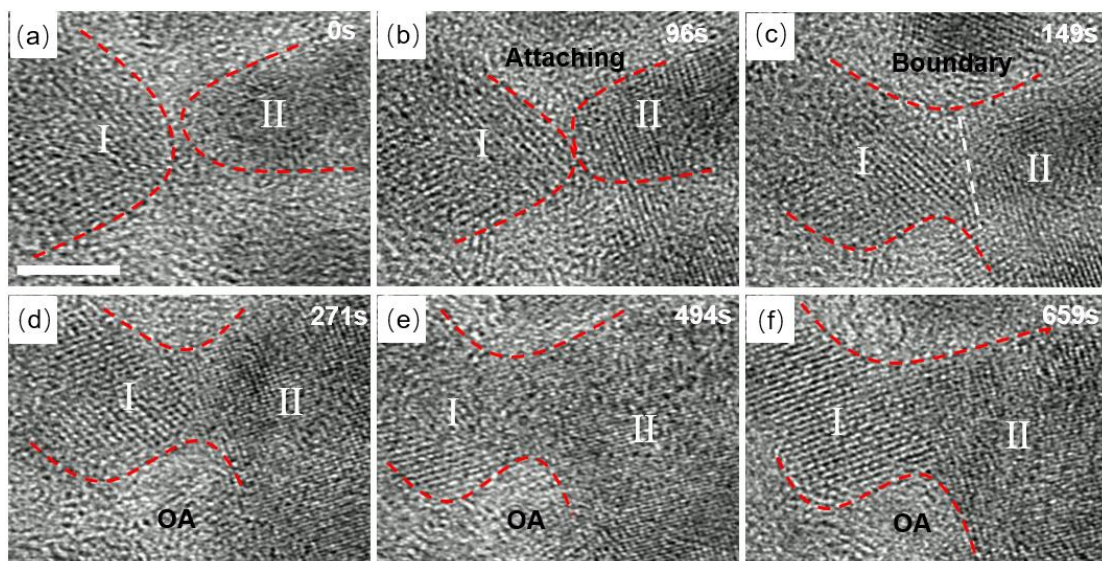


Figure 6.8 Sequential time-resolved *in situ* TEM images showing the process of growth based on amorphous clusters. Scale bar is 5nm.

6.4.2 Tunable morphology and growth mechanisms

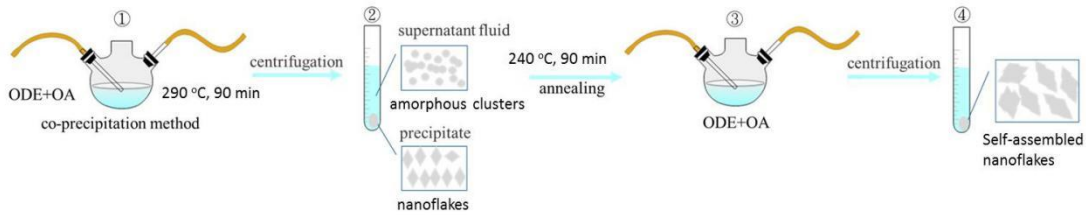


Figure 6.9 Schematic illustration of the co-precipitation and the thermal annealing method for the synthesis of LuF_3 nanoparticles.

Therefore, we propose to use the thermal annealing method to manipulate the morphology of the LuF_3 UC nanoparticles, as shown in Figure 6.9. The required LuF_3 nanoparticles are synthesized by co-precipitation - step ①. It is necessary to avoid random attachment of amorphous nanoclusters in term of the NCs growth process. So the reaction solution was centrifuged and washed for several times to separate supernatant fluid and precipitated nanoparticles - step ②. Subsequently, the LuF_3 nanoparticles were annealed by the thermal annealing method at 240 °C for 90 min - step ③. Finally, the nanoparticles with larger in size are obtained after self-assembly in step ④.

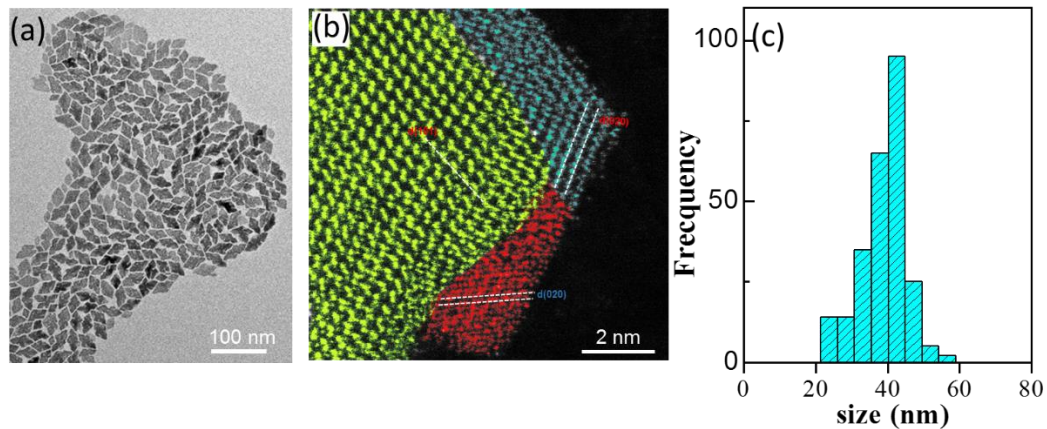


Figure 6.10 (a) Typical TEM, (b) HR-TEM image and (c) the size distribution of $\text{LuF}_3: \text{Yb}^{3+}, \text{Er}^{3+}$ nanoparticles after the thermal annealing process at 240°C for 90 min.

Figure 6.10a shows the TEM image of the LuF_3 nanoparticles after the thermal annealing method with washing process. The TEM image displays that the well mono-dispersed regular flaky LuF_3 possess an average size around 40 nm with perfect crystallization configuration. The crystallinity of the LuF_3 nanoparticles is improved and there is no extra amorphous clusters after the thermal annealing method, especially at the edge of LuF_3 nanoparticles. The HADDF-STEM image of the single LuF_3 (Figure 10b) shows different orientations, ~ 0.361 , ~ 0.338 , ~ 0.361 nm which are corresponding to the orientation of (101), (020) and (410) respectively, may be due to the insufficient energy of the system to drive different lattice planes into perfect matching. On the other hand, the amorphous clusters at edges of nanoparticles have been crystallized, this is because that the amorphous clusters around the nanoparticles are converted from the metastable state (amorphous state) to the stability state (crystal state) during the thermal annealing method.

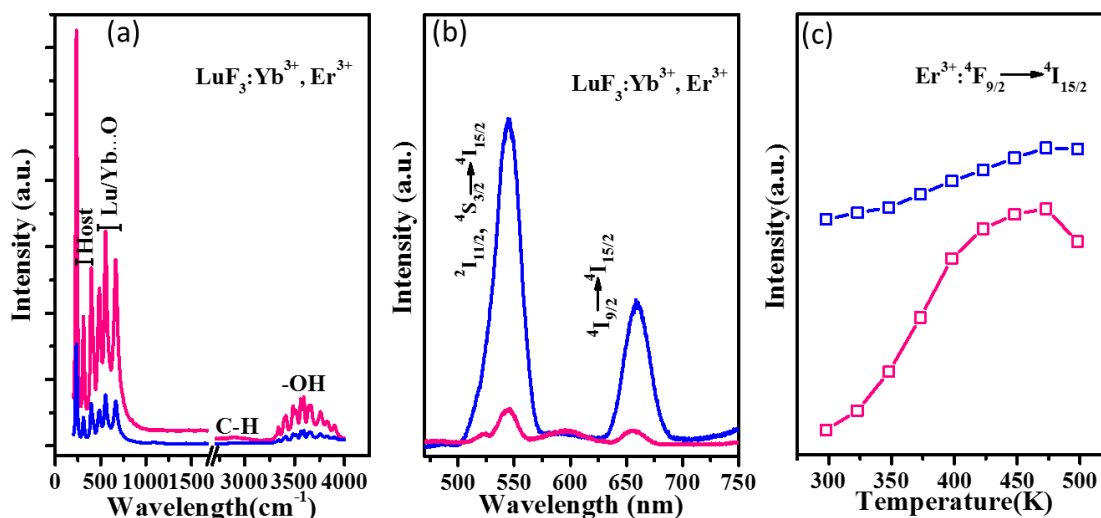


Figure 6.11 (a) Raman spectra; (b) the emission spectra of $\text{LuF}_3:\text{Yb}^{3+}, \text{Er}^{3+}$ nanoparticles, and (c) the emission intensity changes under CW 980 nm excitation at room temperature (The pink and blue lines represent the nanoparticles before and after the thermal annealing process respectively).

Raman spectra of the $\text{LuF}_3:\text{Yb}^{3+}, \text{Er}^{3+}$ nanoparticles shown in Figure 6.11a demonstrates that the total vibration frequencies of oleic acids molecules and ($\text{Yb}\cdots\text{O}$) coordination is greatly reduced due to the complete exhaustion of amorphous nanoclusters after the attachment process. The edge-to-edge attachment process between two adjacent nanoparticles underwent the thermal annealing method is based on the consumption of amorphous nanoclusters. Figure 6.11b and 6.11c plots the emission spectra of $\text{LuF}_3:\text{Yb}^{3+}, \text{Er}^{3+}$ nanoparticles, and the emission intensity changes under CW 980 nm excitation at room temperature. The $\text{LuF}_3:\text{Yb}^{3+}, \text{Er}^{3+}$ nanoparticles exhibit

enhancement more than 10 times of photoluminescence emission intensity after the thermal annealing process. This is due to the removal of the amorphous structures that acts as the quenching center from the edge of nanoparticles and the particle size distribution can show more uniform.

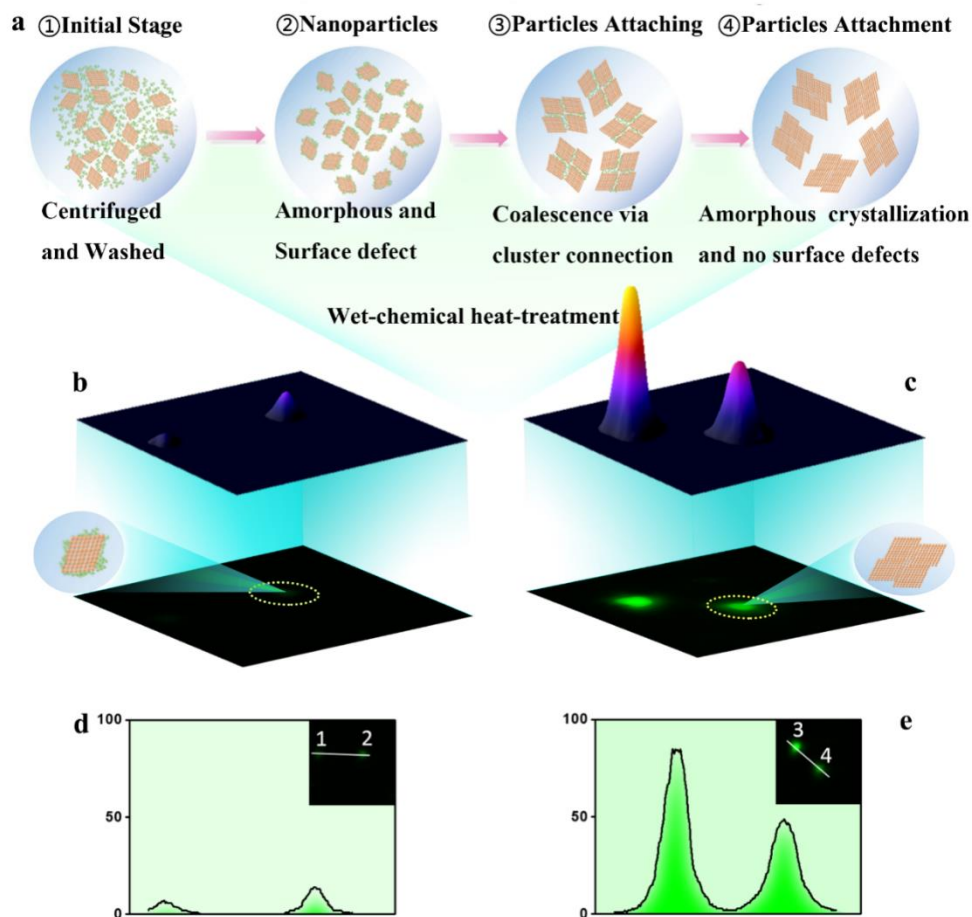


Figure 6.12 The mechanism of the thermal annealing method on the revised surface defect, green and orange spheres are the amorphous cluster and crystallized phase respectively. (b) and (c) show a super-resolution image of Yb^{3+} - Er^{3+} co-doped LuF_3 nanoparticles before and after the thermal annealing method captured by using super-resolution microscopy and the three-



dimensional representation of the wide-field UC emission image under CW 980 nm excitation. (d) And (e) show the intensity recording over the number of scans under CW 980 nm excitation solely for the selected areas.

Based on the above analysis, schematic diagram of the LuF_3 nanoparticles growth process mechanism are given in Figure 6.12 and can be explained as followed: in the initial stage (①), UC nanoparticles without aggregation are obtained, however, amorphous clusters adhered to the edge of UC nanoparticles and randomly dispersed in the as-obtained solution are also observed. After the removal of the dissociative amorphous cluster in the solution, while the amorphous clusters adhered to the nanoparticles are removed (②), particles attachment process lead the particle attachment with the assistance of amorphous clusters (③). Finally, the uniformed flake of the nanoparticle is obtained as expected (④). Therefore, the thermal annealing method is explored to control the LuF_3 nanoparticles growth process. In this process, the amorphous cluster can be transformed from the metastable state to the stability stage, which may contribute to the improvement of the single nanoparticles optical properties. So, the single UC nanoparticle emission spectra were measured under CW 980 nm excitation by using the high-resolution microscopy (Figure 6.1). According to the compared three-dimensional representation of the wide-field UC emission image of the nanoparticle as well as the intensity recording for the selected area before and after the thermal annealing method, the UC emission intensity of the single nanoparticle



can also be increased more than 10 times during the thermal annealing method (Figure 6.12b-6.12e). This is attractive for biological studies and technique commercialization.

6.5 Summary

In summary, we demonstrate the enhancement of UC emission intensity from the Ln^{3+} -doped LuF_3 nanoparticles via the use of the thermal annealing method. The improvement of UC efficiency of the LuF_3 nanoparticles can be explained by the crystallization of the surface amorphous clusters. This is verified by using *in situ* TEM imaging technology to directly observe the growth of UC nanoparticles. The surface amorphous clusters, which act as the quenching centers, crystallize after the thermal annealing method. Besides, by controlling the concentration of amorphous nanoclusters in the precursor solution, we can manipulate the morphology of LuF_3 UC nanoparticles with high-crystal-quality to support effective UC emission. Under CW 980 nm laser excitation, the improvement of UC emission intensity can be increased by an order of magnitude for the Ln^{3+} -doped single LuF_3 UC nanoparticles.



7. Conclusions and outlook

7.1 Conclusions

In this thesis, the lanthanide (Ln^{3+}) -doped upconversion (UC) emission characteristics from the micro- & nano-particles materials are investigated.

The $\beta\text{-NaYF}_4$ hexagonal microrods are chosen to be the laser cavity and gain medium. We demonstrate that the $\beta\text{-NaYF}_4$ hexagonal microrods support whispering gallery modes (WGMs) lasing at 654, 540 and 450 nm simultaneously with linewidths less than 0.4 nm. It is noted that the red lasing emission is easier to be obtained than that of the other two colors. On the other hand, the corresponding lasing threshold can be reduced by increasing the radius of the microrods. The white lasing is obtain from the Yb^{3+} , Er^{3+} , Tm^{3+} doped $\beta\text{-NaYF}_4$ hexagonal microrods with the CIE 1931 color diagram coordinate ($x = 0.3440$, $y = 0.3573$). On the other hand, surface plasmon resonance (SPR) is introduced to enhance the lasing efficiency from single $\text{Yb}^{3+}\text{-Er}^{3+}\text{-Tm}^{3+}$ tri-doped $\beta\text{-NaYF}_4$ hexagonal microrods. This can be achieved by placing the microrods on to the surface of an Ag-coated substrate. For the microrod excited below the lasing threshold, we observe the enhancement of the UC spontaneous emission through the presence of SPR by 10 times. For the microrods under lasing operation, we show that the presence of SPR reduces the lasing threshold by 50%. This is due to the coupling of the WGMs which arose from the coupling between the WGMs of the bare microrod and the SPR modes propagating on the surface of the Ag layer.



Ln^{3+} ions -doped nanoparticles on the stimulated lasing are also investigated. Firstly, the mechanism of the surface defects restoration on the photoluminescence properties of KLu_2F_7 UC nanoparticles are studied in detailed and the enhancement of UC intensity can be achieved by the thermal annealing. The clustering structure of thin $\text{KLu}_2\text{F}_7:38\% \text{Yb}^{3+}, 2\% \text{Er}^{3+}$ UC nanoparticles is directly observed at an atomic scale by using the HAADF-STEM. Under continuous wave (CW) 980 nm laser excitation, the improvement of UC emission intensity by an order of magnitude is observed after restoring the surface defects. This indicates that the influence of surface quenching appears before the thermal annealing, has been suppressed. On the other hand, under 980 nm pulsed laser (6 ns) excitation, the green lasing emission is dominant from the lasing spectra. The fast-transient response to the $^2\text{H}_{11/2}$ and $^4\text{S}_{3/2}$ states and the suppression of the energy back transfer (EBT) process further verify that the high crystallinity of the UC nanoparticles can be restored after the thermal annealing.

Furthermore, we demonstrate the enhancement of UC emission intensity from the Ln^{3+} -doped LuF_3 UC nanoparticles via the use of the thermal annealing by studying the nanoparticle growth process. The improvement of UC efficiency of the LuF_3 UC nanoparticles can be explained by the crystallization of surface amorphous cluster. This is because the surface amorphous clusters, which act as the quenching centers, are crystallized through the thermal annealing process. This is verified by using *in situ* TEM imaging technology to directly observe the growth mechanism of UC nanoparticles. Under CW 980 nm laser excitation, the improvement of UC emission intensity can be increased by an order of magnitude for the Ln^{3+} -doped single LuF_3 UC nanoparticles.



7.2 Outlook

Recently, the use of Ln^{3+} -doped UC materials as the laser gain medium has shown to achieve lasing emission at 310 nm under 980 nm near-infrared (NIR) excitation at room temperature. When compared with the traditional methods (e.g. multiple-photon emission and second harmonic generation) to obtain deep UV emission, the Ln^{3+} -doped UC shows advantages of simple operation procedures and compact in size. However, further improvement of the Ln^{3+} -doped UC efficiency and the lasing cavities design still a challenge especially for the deep UV regime, from 200 to 260 nm. The following paragraphs propose the possible strategies to obtain effective deep UV UC lasers using UC nanoparticles as the gain media.

- 1) Although the standalone $\beta\text{-NaYF}_4$ nanoparticles have shown to have high UC efficiency, it is still not suitable to realize 310 nm lasing under 980 nm excitation especially for high power operation. This is because this type of nanomaterials suffers from its low thermal stability and low optical damage threshold. Hence, we propose to embed Tm^{3+} or Gd^{3+} ions doped $\beta\text{-NaYF}_4$ nanoparticles inside glass-ceramic (i.e. protector of the nanoparticles) as the gain medium to sustain deep UV lasing at high power operation. This is possible as the glass medium can withstand high-power laser pump and show little absorption at deep UV wavelength.
- 2) UC deep UV spontaneous emission at 205 nm has been reported by using Gd^{3+} , Yb^{3+} , and Ho^{3+} doped $\beta\text{-NaLuF}_4$ micro-particles under 980 nm excitation at room temperature. [\[111\]](#) This is possible because the hexagonal $\beta\text{-NaLuF}_4$ host, which has a similar structure compared with the hexagonal $\beta\text{-NaYF}_4$, shows high UC efficiency at deep UV region.



Therefore, we propose to use β -NaLuF₄ micro-or nano-particle as the gain medium to realize deep UV lasing emission at room temperature under 980 nm excitation.

- 3) In chapter 3, we observed lasing emission from 450 to 654 nm based on the hexagonal Er³⁺, Yb³⁺, Tm³⁺ doped β -NaYF₄ microcavities. We have developed a measurement setup by using an optical microscope for the excitation and collection of light from the samples. For measuring emission in deep UV regime, it is necessary to modify the optical microscope so that the corresponding mirrors and lens/objective lens to have low absorption at deep UV wavelength. Hence, this is a necessary modification procedure to effectively detect signal from deep UV lasers.



References

- [1] F. Auzel, Upconversion and anti-stokes processes with f and d ions in solids, *Chemical Reviews* 104(1) (2004) 139-174.
- [2] N. Bloembergen, Solid state infrared quantum counters, *Physical Review Letters* 2(3) (1959) 84.
- [3] M.J. Dejneka, A. Streltsov, S. Pal, A.G. Frutos, C.L. Powell, K. Yost, P.K. Yuen, U. Müller, J. Lahiri, Rare earth-doped glass microbarcodes, *Proceedings of the National Academy of Sciences* 100(2) (2003) 389-393.
- [4] H. Dong, L. D. Sun, C.H. Yan, Basic understanding of the lanthanide related upconversion emissions, *Nanoscale* 5(13) (2013) 5703-5714.
- [5] L.M. Jin, X. Chen, C.K. Siu, F. Wang, S.F. Yu, Enhancing multiphoton upconversion from NaYF₄: Yb/Tm@ NaYF₄ core-shell nanoparticles via the use of laser cavity, *ACS Nano* 11(1) (2017) 843-849.
- [6] L. Johnson, H. J. Guggenheim, Infrared-pumped visible laser, *Applied Physics Letters* 19(2) (1971) 44-47.
- [7] F. Wang, D. Banerjee, Y. Liu, X. Chen, X. G. Liu, Upconversion nanoparticles in biological labeling, imaging, and therapy, *Analyst* 135(8) (2010) 1839-1854.
- [8] M.K. Mahata, H.C. Hofsäss, U. Vetter, Photon-upconverting materials: advances and prospects for various emerging applications, luminescence-an outlook on the phenomena and their applications, *IntechOpen* 2016.



- [9] J.M. Hales, M. Cozzuol, T.E.O. Screen, H.L. Anderson, J.W. Perry, Metalloporphyrin polymer with temporally agile, broadband nonlinear absorption for optical limiting in the near infrared, *Optics Express* 17(21) (2009) 18478-18488.
- [10] M. Michon, 9C3-The influence of Nd^{3+} ion properties in a glass matrix on the dynamics of a Q-spoiled laser, *IEEE Journal of Quantum Electronics* 2(9) (1966) 612-616.
- [11] M. Inokuti, F. Hirayama, Influence of energy transfer by the exchange mechanism on donor luminescence, *The Journal of Chemical Physics* 43(6) (1965) 1978-1989.
- [12] J.S. Chivian, W. E. Case, D. D. Eden, The photon avalanche: a new phenomenon in Pr^{3+} -based infrared quantum counters, *Applied Physics Letters* 35(2) (1979) 124-125.
- [13] F. Lahoz, I.R. Martin, J.M. Calvilla-Quintero, Ultraviolet and white photon avalanche upconversion in Ho^{3+} -doped nanophase glass ceramics, *Applied Physics Letters* 86(5) (2005) 051106.
- [14] Z.L. Yuan, B.E. Kardynal, A.W. Sharpe, A. Shields, High speed single photon detection in the near infrared, *Applied Physics Letters* 91(4) (2007) 041114.
- [15] I.R. Martin, V.D. Rodriguez, Y. Guyot, S. Guy, G. Boulon, M. Joubert, Room temperature photon avalanche upconversion in Tm^{3+} -doped fluoroindate glasses, *Journal of Physics: Condensed Matter* 12(7) (2000) 1507.
- [16] F. Wang, X.G. Liu, Recent advances in the chemistry of lanthanide-doped upconversion nanocrystals, *Chemical Society Reviews* 38(4) (2009) 976-989.
- [17] W. Lenth, R.M. Macfarlane, Upconversion lasers, *Optics and Photonics News* 3(3) (1992) 8-15.



- [18] F. Wang, R.R. Deng, J. Wang, Q.X. Wang, Y. Han, H.M. Zhu, X.Y. Chen, X.G. Liu, Tuning upconversion through energy migration in core-shell nanoparticles, *Nature Materials* 10(12) (2011) 968.
- [19] F. Wang, Y. Han, C.S. Lim, Y. Lu, J. Wang, J. Xu, H. Chen, C. Zhang, M. Hong, X.G. Liu, Simultaneous phase and size control of upconversion nanocrystals through lanthanide doping, *Nature Materials* 463(7284) (2010) 1061.
- [20] A.J. Silversmith, W. Lenth, R.M. Macfarlane, Green infrared - pumped erbium upconversion laser, *Applied Physics Letters* 51(24) (1987) 1977-1979.
- [21] W. Lenth, A.J. Silversmith, R.M. Macfarlane, Green infrared - pumped erbium upconversion lasers, *AIP Conference Proceedings*, AIP, 1988, pp. 8-12.
- [22] R.M. Macfarlane, F. Tong, A.J. Silversmith, W. Lenth, Violet cw neodymium upconversion laser, *Applied Physics Letters* 52(16) (1988) 1300-1302.
- [23] R.A. McFarlane, Dual wavelength visible upconversion laser, *Applied Physics Letters* 54(23) (1989) 2301-2302.
- [24] D.C. Nguyen, G.E. Faulkner, M. Dulick, Blue-green (450-nm) upconversion Tm^{3+} : YLF laser, *Applied Optics* 28(17) (1989) 3553-3555.
- [25] T. Hebert, R. Wannemacher, W. Lenth, R. Macfarlane, Blue and green cw upconversion lasing in Er: YLiF₄, *Applied Physics Letters* 57(17) (1990) 1727-1729.
- [26] T. Herbert, W.R. Risk, R.M. Macfarlane, W. Lenth, Diode-laser-pumped 551-nm upconversion laser in YLiF₄: Er³⁺, *Advanced Solid State Lasers*, Optical Society of America, 1990, p. TNL5.



- [27] D.C. Nguyen, G.E. Faulkner, M.E. Weber, M. Dulick, Blue upconversion thulium laser, *Solid State Lasers*, International Society for Optics and Photonics, 1990, pp. 54-64.
- [28] R.M. Macfarlane, E.A. Whittaker, W. Lenth, Blue, green and yellow upconversion lasing in Er: YLiF₄ using 1.5 μm pumping, *Electronics Letters* 28(23) (1992) 2136-2138.
- [29] T. Hebert, R. Wannemacher, R.M. Macfarlane, W. Lenth, Blue continuously pumped upconversion lasing in Tm: YLiF₄, *Applied Physics Letters* 60(21) (1992) 2592-2594.
- [30] R.J. Thrash, L.F. Johnson, Upconversion laser emission from Yb³⁺-sensitized Tm³⁺ in BaY₂F₈, *JOSA* 11(5) (1994) 881-885.
- [31] R. Brede, E. Heumann, J. Koetke, T. Danger, G. Huber, B. Chai, Green up-conversion laser emission in Er-doped crystals at room temperature, *Applied Physics Letters* 63(15) (1993) 2030-2031.
- [32] R.J. Thrash, L.F. Johnson, Ultraviolet upconversion laser emission from Yb³⁺ sensitized Tm³⁺ in BaY₂F₈, *Advanced Solid State Lasers*, Optical Society of America, 1994, p. US7.
- [33] R. Scheps, Photon avalanche upconversion in Er³⁺: YAlO₃, *IEEE Journal of Quantum Electronics* 31(2) (1995) 309-316.
- [34] J.Y. Allain, M. Monerie, H. Poignant, Blue upconversion fluorozirconate fibre laser, *Electronics Letters* 26(3) (1990) 166-168.
- [35] J.Y. Allain, M. Monerie, H. Poignant, Room temperature CW tunable green upconversion holmium fibre laser, *Electronics Letters* 26(4) (1990) 261-263.
- [36] T.J. Whitley, C.A. Millar, R. Wyatt, M.C. Brierley, D. Szebesta, Upconversion pumped green lasing in erbium doped fluorozirconate fibre, *Electronics Letters* 27(20) (1991) 1785-1786.



- [37] R.G. Smart, D.C. Hanna, A.C. Tropper, S.T. Davey, S.F. Carter, D. Szebesta, CW room temperature upconversion lasing at blue, green and red wavelengths in infrared-pumped Pr³⁺-doped fluoride fibre, *Electronics Letters*, 27(14) (1991) 1307-1309.
- [38] S.G. Grubb, K.W. Bennett, R.S. Cannon, W.F. Humer, CW room-temperature blue upconversion fibre laser, *Electronics Letters* 28(13) (1992) 1243-1244.
- [39] D.S. Funk, S.B. Stevens, J.G. Eden, Excitation spectra of the green Ho: fluorozirconate glass fiber laser, *IEEE Photonics Technology Letters* 5(2) (1993) 154-157.
- [40] J.Y. Allain, M. Monerie, H. Poignant, Red upconversion Yb-sensitised Pr fluoride fibre laser pumped in 0.8 μm region, *Electronics Letters* 27(13) (1991) 1156-1157.
- [41] I.J. Booth, C.J. Mackechnie, B.F. Ventrudo, Operation of diode laser pumped Tm³⁺: ZBLAN upconversion fiber laser at 482 nm, *IEEE Journal of Quantum Electronics* 32(1) (1996) 118-123.
- [42] D.S. Funk, S.B. Stevens, J.G. Eden, Excitation spectra of the green Ho: fluorozirconate glass fiber laser, *IEEE Photonics Technology Letters*, 5(2) 5(2) (1993) 154-157.
- [43] D. Piehler, D. Craven, 11.7 mW green InGaAs-laser-pumped erbium fibre laser, *Electronics Letters* 30(21) (1994) 1759-1761.
- [44] M.L. Dennis, J.W. Dixon, I. Aggarwal, High power upconversion lasing at 810 nm, in Tm: ZBLAN fibre, *Electronics Letters* 30(2) (1994) 136-137.
- [45] D.S. Funk, J.W. Carlson, J.G. Eden, Ultraviolet (381 nm), room temperature laser in neodymium-doped fluorozirconate fibre, *Electronics Letters* 30(22) (1994) 1859-1860.



- [46] D.M. Baney, G. Rankin, K.W. Chang, Simultaneous blue and green upconversion lasing in a laser-diode-pumped $\text{Pr}^{3+}/\text{Yb}^{3+}$ doped fluoride fiber laser, *Applied Physics Letters* 69(12) (1996) 1662-1664.
- [47] D.S. Funk, J.W. Carlson, J.G. Eden, Room-temperature fluorozirconate glass fiber laser in the violet (412 nm), *Optics Letters* 20(13) (1995) 1474-1476.
- [48] P. Xie, T.R. Gosnell, Room-temperature upconversion fiber laser tunable in the red, orange, green, and blue spectral regions, *Optics Letters* 20(9) (1995) 1014-1016.
- [49] A. Saïssy, B. Dussardier, G. Maze, G. Monnom, S.J. Wade, Blue upconversion emission in Er^{3+} -doped fluoride fiber, *Optical Fiber Technology* 2(3) (1996) 249-252.
- [50] R. Paschotta, N. Moore, W.A. Clarkson, A.C. Tropper, D.C. Hanna, G. Mazé, 230 mW of blue light from a thulium-doped upconversion fiber laser, *IEEE Journal of Selected Topics in Quantum Electronics* 3(4) (1997) 1100-1102.
- [51] G. Tohmon, H. Sato, J. Ohya, T. Uno, Thulium: ZBLAN blue fiber laser pumped by two wavelengths, *Applied Optics* 36(15) (1997) 3381-3386.
- [52] T.P. Baraniecki, R. Caspary, W. Kowalsky, Blue, green, red fiber lasers based on Pr/Yb fluoride fibers, *Proceedings of 2004 6th International Conference on Transparent Optical Networks (IEEE Cat. No. 04EX804)*, IEEE, 2004, pp. 206-209.
- [53] Z. Luo, Q. Ruan, M. Zhong, Y. Cheng, R. Yang, B. Xu, H. Xu, Z. Cai, Compact self-Q-switched green upconversion Er: ZBLAN all-fiber laser operating at 543.4 nm, *Optics Letters* 41(10) (2016) 2258-2261.



- [54] O. Hellmig, S. Salewski, A. Stark, J. Schwenke, P.E. Toschek, K. Sengstock, V.M. Baev, Multicolor diode-pumped upconversion fiber laser, *Optical Letter* 35(13) (2010) 2263-2265.
- [55] J. Ward, O. Benson, P. Reviews, WGM microresonators: sensing, lasing and fundamental optics with microspheres, *Laser & Photonics Reviews* 5(4) (2011) 553-570.
- [56] J. Wang, T. Zhan, G. Huang, P.K. Chu, Y.F. Mei, Optical microcavities with tubular geometry: properties and applications, *Laser & Photonics Reviews* 8(4) (2014) 521-547.
- [57] C. Zhang, C.L. Zou, Y. Yan, C. Wei, J.M. Cui, F.W. Sun, J. Yao, Y.S. Zhao, Self-assembled organic crystalline microrings as active whispering-gallery-mode optical resonators, *Advanced Optical Materials* 1(5) (2013) 357-361.
- [58] I.S. Grudinin, A.B. Matsko, A.A. Savchenkov, D. Strekalov, V.S. Ilchenko, L. Maleki, Ultra high Q crystalline microcavities, *Optics Communications* 265(1) (2006) 33-38.
- [59] C.H. Dong, L. He, Y.F. Xiao, V. Gaddam, S. Ozdemir, Z.F. Han, G.C. Guo, L.J. Yang, Fabrication of high-Q polydimethylsiloxane optical microspheres for thermal sensing, *Applied Physics Letters* 94(23) (2009) 231119.
- [60] D.W. Vernooy, V.S. Ilchenko, H. Mabuchi, E.W. Streed, H.J. Kimble, High-Q measurements of fused-silica microspheres in the near infrared, *Optics Letters* 23(4) (1998) 247-249.
- [61] V. Sandoghdar, F. Treussart, J. Hare, V.L. Seguin, J.M. Raimond, S. Haroche, Very low threshold whispering-gallery-mode microsphere laser, *Physical Review Letters* 54(3) (1996) R1777.



- [62] W.V. Klitzing, E. Jahier, R. Long, F. Lissillour, V.L. Seguin, J. Hare, J. Raimond, S. Haroche, Very low threshold lasing in Er^{3+} doped ZBLAN microsphere, *Electronics Letters* 35(20) (1999) 1745-1746.
- [63] H. Fujiwara, K. Sasaki, Upconversion lasing of a thulium-ion-doped fluorozirconate glass microsphere, *Journal of Applied Physics* 86(5) (1999) 2385-2388.
- [64] H. Fujiwara, K. Sasaki, Microspherical lasing of an erbium-ion-doped glass particle, *Japanese Journal of Applied Physics* 41(1) (2002) L46-L48.
- [65] Y. Wu, J.M. Ward, S. Nic Chormaic, Ultralow threshold green lasing and optical bistability in ZBNA ($\text{ZrF}_4\text{-BaF}_2\text{-NaF-AlF}_3$) microspheres, *Journal of Applied Physics* 107(3) (2010) 033103.
- [66] X. Wang, Y. Yu, S. Wang, J.M. Ward, S.N. Chormaic, P. Wang, Single mode green lasing and multicolor luminescent emission from an $\text{Er}^{3+}\text{-Yb}^{3+}$ co-doped compound fluorosilicate glass microsphere resonator, *OSA Continuum* 1(1) (2018) 261-273.
- [67] X. Li, D. Shen, J. Yang, C. Yao, R. Che, F. Zhang, D. Zhao, Successive layer-by-layer strategy for multi-shell epitaxial growth: shell thickness and doping position dependence in upconverting optical properties, *Chemistry of Materials* 25(1) (2013) 106-112.
- [68] M. Ding, D. Chen, D. Ma, J. Dai, Y. Li, Z. Ji, Highly enhanced upconversion luminescence in lanthanide-doped active-core/luminescent-shell/active-shell nanoarchitectures, *Journal of Materials Chemistry C* 4(13) (2016) 2432-2437.
- [69] F. Qian, S. Gradečak, Y. Li, C.-Y. Wen, C.M. Lieber, Core/Multishell nanowire heterostructures as multicolor, high-efficiency light-emitting diodes, *Nano Letters* 5(11) (2005) 2287-2291.



- [70] D. Chen, L. Liu, P. Huang, M. Ding, J. Zhong, Z. Ji, Nd³⁺-sensitized Ho³⁺ single-band red upconversion luminescence in core-shell nanoarchitecture, *The Journal of Physical Chemistry Letters* 6(14) (2015) 2833-2840.
- [71] A.F. Khan, R. Yadav, P.K. Mukhopadhyaya, S. Singh, C. Dwivedi, V. Dutta, S. Chawla, Core-shell nanophosphor with enhanced NIR-visible upconversion as spectrum modifier for enhancement of solar cell efficiency, *Journal of Nanoparticle Research* 13(12) (2011) 6837-6846.
- [72] H. Zhu, X. Chen, L.M. Jin, Q.J. Wang, F. Wang, S.F. Yu, Amplified spontaneous emission and lasing from lanthanide-doped up-conversion nanocrystals, *ACS Nano* 7(12) (2013) 11420-11426.
- [73] X. Chen, L. Jin, W. Kong, T. Sun, W. Zhang, X. Liu, J. Fan, S.F. Yu, F. Wang, Confining energy migration in upconversion nanoparticles towards deep ultraviolet lasing, *Nature Communications* 7 (2016) 10304.
- [74] A. Fernandez-Bravo, K. Yao, E.S. Barnard, N.J. Borys, E.S. Levy, B. Tian, C.A. Tajon, L. Moretti, M.V. Altoe, S. Aloni, K. Beketayev, F. Scotognella, B.E. Cohen, E.M. Chan, P.J. Schuck, Continuous-wave upconverting nanoparticle microlasers, *Nature Nanotechnology* 13(7) (2018) 572-577.
- [75] S. Heer, K. Kömpe, H.U. Güdel, M. Haase, Highly efficient multicolour upconversion emission in transparent colloids of lanthanide-doped NaYF₄ nanocrystals, *Advanced Materials* 16(23-24) (2004) 2102-2105.



- [76] F. Wang, X.G. Liu, Upconversion multicolor fine-tuning: visible to near-infrared emission from lanthanide-doped NaYF₄ nanoparticles, *Journal of the American Chemical Society* 130(17) (2008) 5642-5643.
- [77] G.S. Yi, G.M. Chow, Synthesis of hexagonal-phase NaYF₄:Yb, Er and NaYF₄:Yb, Tm nanocrystals with efficient up-conversion fluorescence, *Advanced Functional Materials* 16(18) (2006) 2324-2329.
- [78] R. Abdul Jalil, Y. Zhang, Biocompatibility of silica coated NaYF₄ upconversion fluorescent nanocrystals, *Biomaterials* 29(30) (2008) 4122-4128.
- [79] C. Zhang, L. Yang, J. Zhao, B. Liu, M.Y. Han, Z. Zhang, White-light emission from an integrated upconversion nanostructure: toward multicolor displays modulated by laser power, *Angewandte Chemie International Edition* 54(39) (2015) 11531-11535.
- [80] E. Jang, S. Jun, H. Jang, J. Lim, B. Kim, Y. Kim, White-light-emitting diodes with quantum dot color converters for display backlights, *Advanced Materials* 22(28) (2010) 3076-3080.
- [81] F. Fan, S. Turkdogan, Z. Liu, D. Shelhammer, C.Z. Ning, A monolithic white laser, *Nature Nanotechnology* 10 (2015) 796.
- [82] J.C. Huang, Y.C. Hsiao, Y.T. Lin, C.R. Lee, W. Lee, Electrically switchable organo-inorganic hybrid for a white-light laser source, *Scientific Reports* 6 (2016) 28363.
- [83] L. Ulrich, Whiter brights with lasers, *IEEE Spectrum* 50(11) (2013) 36-56.
- [84] M. Werkstetter, S. Weber, F. Hirth, C. Amann, Laser light in the BMW i8 controlling and E/E integration, *Technology Light Systems* 9(4) (2014) 14-19.
- [85] C. Basu, M. Meinhardt-Wollweber, B. Roth, Lighting with laser diodes, *Advanced Optical Technologies*, 2013, p. 313.



- [86] A.K. Dharmadhikari, F.A. Rajgara, D. Mathur, Systematic study of highly efficient white light generation in transparent materials using intense femtosecond laser pulses, *Applied Physics B* 80(1) (2005) 61-66.
- [87] D. Chen, Y. Wang, K. Zheng, T. Guo, Y. Yu, P. Huang, Bright upconversion white light emission in transparent glass ceramic embedding $\text{Tm}^{3+}/\text{Er}^{3+}/\text{Yb}^{3+}:\beta\text{-YF}_3$ nanocrystals, *Applied Physics Letters* 91(25) (2007) 251903.
- [88] H. Qin, D. Wu, J. Sathian, X. Xie, M. Ryan, F. Xie, Tuning the upconversion photoluminescence lifetimes of $\text{NaYF}_4:\text{Yb}^{3+}, \text{Er}^{3+}$ through lanthanide Gd^{3+} doping, *Scientific Reports* 8(1) (2018) 12683.
- [89] C. Duan, L. Liang, L. Li, R. Zhang, Z. Ping Xu, Recent Progresses of upconversion luminescence nanomaterials for biomedical applications, *Journal of Materials Chemistry B* 6(2) (2018): 192-209.
- [90] J. Żmojda, D. Dorosz, M. Kochanowicz, D. Jan, Active glasses as the luminescent sources of radiation for sensor applications, *Bulletin of the Polish Academy of Sciences Technical Sciences* 62(2) (2014): 393-397.
- [91] C. Mi, J. Wu, Y. Yang, B. Han, J. Wei, Efficient upconversion luminescence from $\text{Ba}_5\text{Gd}_8\text{Zn}_4\text{O}_{21}:\text{Yb}^{3+}, \text{Er}^{3+}$ based on a demonstrated cross-relaxation process, *Scientific Reports* 6 (2016) 22545.
- [92] S. Schietinger, T. Aichele, H.Q. Wang, T. Nann, O. Benson, Plasmon-enhanced upconversion in single $\text{NaYF}_4:\text{Yb}^{3+}/\text{Er}^{3+}$ codoped nanocrystals, *Nano Letters* 10(1) (2010) 134-138.



- [93] D.M. Wu, A. García-Etxarri, A. Salteo, J.A. Dionne, Plasmon-enhanced upconversion, *The Journal of Physical Chemistry Letters* 5(22) (2014) 4020-4031.
- [94] W. Park, D. Lu, S. Ahn, Plasmon enhancement of luminescence upconversion, *Chemical Society Reviews* 44(10) (2015) 2940-2962.
- [95] Z. Xu, M. Quintanilla, F. Vetrone, A.O. Govorov, M. Chaker, D. Ma, Harvesting lost photons: plasmon and upconversion enhanced broadband photocatalytic activity in core@shell microspheres based on lanthanide-doped NaYF₄, TiO₂, and Au, *Advanced Functional Materials* 25(20) (2015) 2950-2960.
- [96] M.R. Dousti, R.J. Amjad, Z.A.S. Mahraz, Enhanced green and red upconversion emissions in Er³⁺-doped boro-tellurite glass containing gold nanoparticles, *Journal of Molecular Structure* 1079 (2015) 347-352.
- [97] Y. Wang, Z. Yang, Y. Ma, Z. Chai, J. Qiu, Z. Song, Upconversion emission enhancement mechanisms of Nd³⁺-sensitized NaYF₄:Yb³⁺,Er³⁺ nanoparticles using tunable plasmonic Au films: plasmonic-induced excitation, radiative decay rate and energy-transfer enhancement, *Journal of Materials Chemistry C* 5(33) (2017) 8535-8544.
- [98] Y. Xue, C. Ding, Y. Rong, Q. Ma, C. Pan, E. Wu, B. Wu, H. Zeng, Tuning plasmonic enhancement of single nanocrystal upconversion luminescence by varying Gold nanorod diameter, *Small* 13(36) (2017) 1701155.
- [99] M. Ambati, S.H. Nam, E. Ulin-Avila, D.A. Genov, G. Bartal, X. Zhang, Observation of stimulated emission of surface plasmon polaritons, *Nano Letters* 8(11) (2008) 3998-4001.
- [100] C. Shi, S. Soltani, A.M. Armani, Gold nanorod plasmonic upconversion microlaser, *Nano Letters* 13(12) (2013) 5827-5831.



- [101] H. Dong, L.D. Sun, W. Feng, Y. Gu, F. Li, C.H. Yan, Versatile spectral and lifetime multiplexing nanoplatfom with excitation orthogonalized upconversion luminescence, *ACS Nano* 11(3) (2017) 3289-3297.
- [102] T. Rinkel, A.N. Raj, S. Dühnen, M. Haase, Synthesis of 10 nm β -NaYF₄:Yb,Er/NaYF₄ core/shell upconversion nanocrystals with 5 nm particle cores, *Angewandte Chemie International Edition* 55(3) (2016) 1164-1167.
- [103] S. Han, X. Qin, Z. An, Y. Zhu, L. Liang, Y. Han, W. Huang, X.G. Liu, Multicolour synthesis in lanthanide-doped nanocrystals through cation exchange in water, *Nature Communications* 7 (2016) 13059.
- [104] F. Lu, L. Yang, Y. Ding, J.J. Zhu, Highly emissive Nd³⁺-sensitized multilayered upconversion nanoparticles for efficient 795 nm operated photodynamic therapy, *Advanced Functional Materials* 26(26) (2016) 4778-4785.
- [105] M.K. Gnanasammandhan, N.M. Idris, A. Bansal, K. Huang, Y. Zhang, Near-IR photoactivation using mesoporous silica-coated NaYF₄:Yb,Er/Tm upconversion nanoparticles, *Nature Protocols* 11 (2016) 688.
- [106] X. Lin, X. Chen, W. Zhang, T. Sun, P. Fang, Q. Liao, X. Chen, J. He, M. Liu, F. Wang, P. Shi, Core-shell-shell upconversion nanoparticles with enhanced emission for wireless optogenetic inhibition, *Nano Letters* 18(2) (2018) 948-956.
- [107] F. Wang, J. Wang, X. Liu, Direct evidence of a surface quenching effect on size-dependent luminescence of upconversion nanoparticles, *Angewandte Chemie International Edition* 49(41) (2010) 7456-7460.



- [108] F. Wang, Y. Han, C.S. Lim, Y. Lu, J. Wang, J. Xu, H. Chen, C. Zhang, M. Hong, X. Liu, Simultaneous phase and size control of upconversion nanocrystals through lanthanide doping, *Nature* 463 (2010) 1061.
- [109] T.J. Woehl, J.E. Evans, I. Arslan, W.D. Ristenpart, N.D. Browning, Direct in situ determination of the mechanisms controlling nanoparticle nucleation and growth, *ACS Nano* 6(10) (2012) 8599-8610.
- [110] J.E. Evans, K.L. Jungjohann, N.D. Browning, I. Arslan, Controlled growth of nanoparticles from solution with in situ liquid transmission electron microscopy, *Nano Letters* 11(7) (2011) 2809-2813.
- [111] L. Wang, M. Lan, Z. Liu, G. Qin, C. Wu, X. Wang, W. Qin, W. Huang, L. Huang, Enhanced deep-ultraviolet upconversion emission of Gd^{3+} sensitized by Yb^{3+} and Ho^{3+} in β - $NaLuF_4$ microcrystals under 980 nm excitation, *Journal of Materials Chemistry C* 1(13) (2013) 2485-2490.